UC Davis

UC Davis Electronic Theses and Dissertations

Title

Ion Channel Clusters in Arterial Smooth Muscle: Investigating the Mechanisms of KV2.1 and CaV1.2 Formation in Murine Mesenteric Cells and Their Implications for Smooth Muscle Physiology and Sex Differences

Permalink

https://escholarship.org/uc/item/5c55k79w

Author

Matsumoto, Collin Scott Tadashi

Publication Date

2023

Peer reviewed|Thesis/dissertation

eScholarship.org Powered by the California Digital Library
University of California

Ion Channel Clusters in Arterial Smooth Muscle: Investigating the Mechanisms of $K_V2.1$ and $Ca_V1.2$ Formation in Murine Mesenteric Cells and Their Implications for Smooth Muscle Physiology and Sex Differences

By

COLLIN SCOTT TADASHI MATSUMOTO
DISSERTATION

Submitted in partial satisfaction of the requirements for the degree of

DOCTOR OF PHILOSOPHY

in

Molecular, Cellular and Integrative Physiology

in the

OFFICE OF GRADUATE STUDIES

of the

DAVIS

Approved:

Luis Fernando Santana, Chair

Eamonn Dickson

Crystal Ripplinger

Committee in Charge

2023

Copyright by Collin Scott Tadashi Matsumoto 2023

Abstract:

The work contained within this dissertation aims to investigate the role and mechanisms of $Ca_V1.2$ and $K_V2.1$ ion channel cluster formation in the membrane of arterial smooth muscle cells. Clustering of ion channels selective for these ions have long been a commonly observed phenotype, yet the mechanisms of cluster formation are still unknown. Overall, this dissertation provides a model by which ion channel clusters form stochastically via a self-assembly process in the membrane based on three mechanistic probabilities: nucleation, growth, and removal. Additionally, we focused on clustering and interactions of two key ion channels, $K_V2.1$ and $Ca_V1.2$, in smooth muscle physiology selective for potassium (K^+) and calcium (Ca^{2+}) respectively. The opening of these channels play key roles in arterial physiology, counterbalancing each other to affect arterial diameter. The key findings from this work help to elucidate the mechanisms involved in the trafficking of ion channels, maintenance of clusters in the plasma membrane and provide potential reasoning for sex-based differences in smooth muscle physiology. Using a multiscale experimental and computational approach, we describe a key interaction between $Ca_V1.2$ and $K_V2.1$ in arterial smooth muscle. This model proposes that $K_V2.1$ clustering state is not a determinate of channel conduction in mesenteric smooth muscle. Additionally, $K_V2.1$ macro-clusters serve as a sex-specific site for increased $Ca_V1.2$ clustering and decreasing $K_V2.1$ macro-clustering decreases $Ca_V1.2$ channel clustering. This sex-based interaction ultimately plays a key role in Ca^{2+} dynamics and smooth muscle physiology.

Acknowledgements:

To all my mentors, colleagues, family and friends – thank you. This journey was not possible without the love and support of my network. I cannot express how deeply thankful and honored I am to have met and worked with Dr. Fernando Santana. To say that I am a mentee of such an accomplished professional would be an understatement. Dr. Santana has taught me to be a better scientist and an even better person. He has allowed me to explore the depths of my research, challenged me to think critically and offered hours upon hours of support both in a scientific setting and in support of my personal growth. I will always admire Fernando's advice to think critically, to always ask questions and chase what I am passionate of. Thank you, Fernando, for the invaluable advice and support. A special thanks go to my committee members Drs. Eamonn Dickson and Crystal Ripplinger. Both have provided incredible support and feedback over the years. I am also thankful to have served with both professors on many student/faculty committees who's focus on mentorship has always made me comfortable to ask for help. I know that our graduate program, fellow graduate students and their lab members will always be in great hands and that they will usher in and develop so many great scientists. I am also incredibly grateful to the colleagues I have had the privilege to work with. Our lab has always had such great chemistry and collaborative spirit that has only helped to create lifelong friendships no matter the distance. I will forever be grateful for the diversity that surrounded me and the opportunity to learn about other cultures and backgrounds. I have learned so many lessons from all these great people that I can take with me wherever I go.

To my friends and family. We did it. It was not always easy, but it was your advice and encouragement that was crucial to my success. Mom, Dad, and Heather, thank you for the support and guidance throughout this whole process. You have always encouraged me to explore my interests and set wonderful examples of what dedication, perseverance and a good work ethic can get you in life. To Janice, thank you for all the love and support (both personally and financially). We have already accomplished so much in life, and this was a major step that would not have been possible without you. From the long nights, early mornings, and hours of complaining – you have always supported me. Even though I have literally put you to sleep with talk about my work you have consistently pushed me to continue and get the most out of every situation. I am incredibly lucky to have you in my life and cannot tell you how important it was and how lucky I am to come home to you.

Table of Contents

List of Figures and Tables

List of Abbreviations

Symbol	Abbreviation
Å	Angstrom
κ	Coupling coefficient
µL	Microliter
µm	Micron
µM	Micromolar
$[Ca^{2+}]_i$	Intracellular calcium concentration
a.a.	Amino acid
AKAP	A-kinase anchoring protein
ANOVA	One-way analysis of variance
BK_{Ca}	Large conductance calcium activated potassium channel
Ca^{2+}	Calcium
$CaCl_2$	Calcium chloride
CaM	Calmodulin
Ca_V	Voltage-gated calcium channel
CDI	Calcium dependent inactivation
cGMP	Cyclic guanosine monophosphate
CICR	Calcium-induced calcium release
Cs	Cesium
CsCl	Cesium chloride
CsOH	Cesium hydroxide
CVD	Cardiovascular disease

DAG	Diacylglycerol
DMEM	Dulbecco's Modified Eagle Medium
EC	Excitation-contraction
EGTA	Ethyleneglycol- *bis*(β-aminoethyl)-N,N,N',N'-tetraacetic Acid
EMCCD	Electron-multiplying charge-coupled devidce
ER	Endoplasmic reticulum
ER-PM	Endoplasmic reticulum plasma membrane junctions
ET-1	Endothelin-1
FV3000	Olympus Fluoview 3000
GA	Glutaraldehyde
GLOX	Glucose oxidase
GPCR	G-protein coupled receptor
GSD	Ground state depletion
HCl	Hydrochloride acid
Hz	Hertz
I	Current
IBC	IP_3 binding core
IK_{Ca}	Intermediate conductance Ca^{2+} activated K^+ channel
IP_3	Inositol 1,4,5 triphosphate
IP_3R	Inositol 1,4,5 triphosphate receptor
K^+	Potassium
KCl	Potassium chloride
kg	Kilogram

kHz	Kilohertz
KOH	Potassium hydroxide
K_V	Voltage-gated potassium channel
$K_V2.1^{-/-}$	$K_V2.1$ null
L	Liter
LTCC	L-type calcium channel
MΩ	Megaohm
mAB	Monoclonal antibody
MEA	Cysteamine hydrochloride
MEPS	Myoendothelial projections
Mg^{2+}	Magnesium
MgATP	Magnesium adenosine triphosphate
$MgCl_2$	Magnesium chloride
MLCK	Myosin light chain kinase
mg	Milligram
mM	Millimolar
ms	Millisecond
mV	Millivolt
n	Number of quantal levels reached by the sparklet site
ng	Nanogram
NA	Numerical aperture
Na^+	Sodium
NaCl	Sodium chloride

NaOH	Sodium hydroxide
NCX	Na^{+}/Ca^{2+} exchanger
Ni^{2+}	Nickel
NO	Nitric oxide
NOS	Nitric oxide synthase
nm	Nanometer
nM	Nanomolar
NMDG	N-methyl-D-glucamine
NVC	Neurovascular coupling
PA	Photoactivatable
PBS	Phosphate-buffered saline
PCR	Polymerase chain reaction
P_g	Probability of growth
PIP2	Phosphatidylinositol 4,5-bisphosphate
PKA	Protein kinase A
PKC	Protein kinase C
PKG	Protein kinase G
PLA	Proximity ligation assay
PLC	Phospholipase C
PLB	Phospholamban
PMCA	Plasma membrane Ca^{2+} ATPase
P_n	Probability of nucleation
P_O	Open probability

P_R	Probability of removal
PRC	Proximal restriction and clustering
P_s	Probability of sparklet occurrence
PSS	Physiological saline solution
qPCR	Quantitative polymerase chain reaction
RLC	Regulatory light chain
ROI	Region of interest
RyR	Ryanodine receptor
SEM	Standard error of the mean
SERCA	Sarco/endoplasmic reticulum calcium ATPase
SK_{Ca}	Small conductance Ca^{2+} activated K^+ channels
SR	Sarcoplasmic reticulum
STOC	Spontaneous transient outward currents=
TEA-Cl	Tetraethylammonium chloride
$T_{1/2}$	Half amplitude
TIRF	Total internal reflection fluorescence
TGCC	T-type calcium channel
VDI	Voltage dependent inactivation
VGCC	Voltage-gated calcium channels
VSM	Vascular smooth muscle
WGA	Wheat germ agglutinin
WT	Wild-type

Chapter 1: Introduction

1.1 Cardiovascular system overview

The cardiovascular system is composed of the heart, vasculature, and blood with primary functions to transport oxygen, nutrients, and metabolic wastes, regulate water, pH and temperature and protect from foreign invaders and pathogens. This is accomplished by the coordination of three major components. The heart which primarily serves as a pump creates a pressure gradient that propels blood through the vasculature. The vasculature which consists of the arterial, venule and capillary system, serves as a conduit for blood in order to delivery nutrients and remove wastes from tissues. The blood is the media for transport throughout the system. Closely related, although not part of the cardiovascular system is the lymphatic system. It is a system of vessels and organs that closely interacts with the vasculature primarily functioning to collect and transport lymph, a clear liquid that carries immune cells and waste products from the body's tissues back into the bloodstream. In addition to its role in fluid balance, the lymphatic system also plays a critical role in immune function.

1.2 The heart

The heart is a closed four-chambered system which pumps blood through the two major vasculature circuits - the pulmonary and systemic circulations. The heart’s primary function is to beat at regular intervals, creating a pressure gradient that propels blood throughout the vascular network. The beating of the heart is incredibly precise and regular but can be modulated to increase or decrease in frequency and strength. In a

healthy individual, action potentials originate in the pacemaking cells of the sinoatrial node located within the right atria.

From the sinoatrial node, electrical signals propagate cell to cell via gap junction throughout the left and right atria. The action potentials then propagate to the atrioventricular node throughout the left and right sides of the heart via the bundle of His and Purkinje fibers leading to contraction of the ventricles and pumping of blood into the systemic circulation.

Extensive research has been dedicated to understanding the role of pacemaking cells in cardiovascular physiology. The initiation of the heartbeat is commonly believed to occur via an entrainment mechanism, whereby a small group of pacemaker cells within the sinoatrial node have a higher firing rate than other cells in the cardiac conduction system. These pacemaker cells synchronize with each other through electrical signals transmitted via interactions between gap junctions, providing a commonly accepted model for heartbeat initiation. It is noteworthy that the leading pacemaking location is not fixed(*1*-*3*) and can change in reaction to physiological stimuli(*4*).

A recent study from our lab examined how the organization of the microvasculature in the sinoatrial node relates to the electrical activity of nearby myocytes(*5*). We propose that microvascular densities differ regionally within the sinoatrial node to match the electrical and Ca^{2+} dynamics of nearby myocytes, ultimately dictating the site of dominant pacemaking within the node. Specifically, the superior sinoatrial node has a

higher vascular density, positioning myocytes with metabolically demanding, high-frequency action potentials in closer proximity to vessels. On the other hand, lower vascularization and electrical activity in the inferior sinoatrial node may restrict these cells to support sinoatrial node periodicity with sporadic voltage fluctuations via a stochastic resonance mechanism.

This model is based on a phenomenon called stochastic resonance where a weak signal can be amplified by the assistance of noise. Such stochastic resonance events have been implicated in the activation of APs in neurons(*6, 7*). In this scenario, the SAN cells exhibit stochastic local Ca^{2+} signals, generating low-amplitude electrical signals that, individually, may not trigger cell firing since they fall below the threshold. However, when these chance occurrences coincide with an electrical signal from a periodic oscillator, subthreshold signal events (referred to as resonance) have the potential to integrate and, at their peaks, enhance the likelihood of surpassing the threshold for cell firing(*8*). In this formulation, the presence of noisy SAN cells with stochastic local Ca^{2+} transients plays a role in enhancing both the intensity and regularity of SAN activation. Despite the limited understanding of the impact of stochastic resonance on pace-making activity and cardiac contractility, a recent study proposed that it enhances the synchronization capacity within the coupling of electrical stimulation and contractile response(*9*). In the stochastic resonance model, all SAN cells are important in driving the system. In this model both the noisy cells and the periodic oscillators play important roles. The noisy cells create local Ca^{2+} release events increasing the reliability of the system to entrainment and adaptation, whereas the recurring electrical signaling

emanating from the inherently oscillating cells are critical for SAN activity altogether. This mechanism does not involve entrainment by an external stimulus, but rather, it suggests that the regional variation in the microvascular densities can shape the intrinsic pacemaking properties of the sinoatrial node myocytes, allowing for efficient and effective coordination of cardiac function. Our data provides a significant new insight that the ability of certain areas of the node to function as periodic oscillators or stochastic signal generators may be largely influenced by the density of vessels and consequently, blood flow.

1.2.1 The cardiac cycle

The cardiac cycle is a series of events that occur during one heartbeat, which includes the contraction and relaxation of the heart muscle cells, ultimately resulting in the pumping of blood throughout the body. The cardiac cycle begins with the contraction of the atria, which pushes blood into the ventricles through the open atrioventricular valves (tricuspid for the right side and mitral/bicuspid for the left). As the atria relax, the ventricles begin to contract, increasing the pressure within the ventricles and causing the atrioventricular valves to close. During this step, isovolumetric contraction occurs as the valves leading into and out of the ventricles are closed, and the volume of blood in the ventricles remains. Once the pressure within the ventricles exceeds that of the aorta and pulmonary arteries, the semilunar valves (pulmonary and aortic) open, allowing blood to be ejected from the ventricles into the aorta and pulmonary artery. The volume of blood ejected during ventricular ejection is known as the stroke volume. Once the ventricles have ejected their blood and begin to relax, the pressure within the ventricles

decrease leading to the closure of the semilunar valves. At this point, the ventricles are again closed off, and the volume of blood in the ventricles remains constant until the pressure within the atria exceeds that of the ventricles, causing the atrioventricular valves to open and allowing blood to flow from the atria into the ventricles. As the atria contract, they push blood into the ventricles through the open atrioventricular valves, filling the ventricles with blood in preparation for the next cardiac cycle. The duration of the cardiac cycle and the timing of each of these events can be influenced by a variety of factors, including the autonomic nervous system, hormones, and other physiological processes. The ability of the heart to adapt and respond to changing conditions is essential for maintaining proper cardiovascular function and overall health.

1.2.2 Excitation-contraction coupling in the heart

At a cellular level, the mechanical pumping relies on a process termed excitation-contraction (EC) coupling (**Figure 1.1**). As an action potential propagates along the membrane of the cardiomyocyte, the electrical signal activates voltage-gated, L-type calcium channel $Ca_V1.2$ leading to a localized Ca^{2+} influx. Clusters of $Ca_V1.2$, form functional units with nearby ryanodine receptors called “couplons”(*10, 11*) expressed in the closely juxtaposed sarcoplasmic reticulum (SR). This close interaction results in a process termed calcium induced calcium release (CICR) where the activation of a cluster of $Ca_V1.2$ channel creates a localized Ca^{2+} signal within this intracellular compartment between sarcolemma and sarcoplasmic reticulum. This Ca^{2+} signal activates nearby ryanodine receptors creating a larger calcium event called a “spark”(*12*) further increasing intracellular Ca^{2+} concentrations. Synchronous $Ca_V1.2$-

activated spark activity summate to create a global Ca^{2+} transient, initiating contraction. The generation of a global Ca^{2+} signal following a series of local RyRs openings, initiated by $Ca_V1.2$, constitutes the fundamental principle of a local control theory for EC coupling.

For the heart to relax, intracellular calcium must be brought down to resting levels via several different mechanisms. The low intracellular Ca^{2+} concentrations are maintained primarily through the Na^+/Ca^{2+} exchanger (NCX)(*13*) and the sarco/endoplasmic reticulum calcium ATPase (SERCA) protein found in the sarcoplasmic reticulum which fills the SR Ca^{2+} store(*14*). There is also evidence that the plasma membrane Ca^{2+} ATPase (PMCA), and mitochondrial Ca^{2+} uniporter (MCU) play a smaller but significant role in Ca^{2+} homeostasis. NCX is an electrogenic protein that facilitates the exchange of sodium (Na^+) and Ca^{2+} across the plasma membrane in either the Ca^{2+}-efflux or Ca^{2+}-influx mode, depending on the electrochemical gradients of the substrate ions. The primary function on a beat-to-beat basis is to extrude Ca^{2+} from myocytes during relaxation and diastole, which maintains Ca^{2+} balance by counteracting the Ca^{2+} entry through L-type Ca^{2+} channels during cardiac excitation. SERCA plays a critical role in cardiac muscle function by pumping Ca^{2+} from the cytosol back into the SR during relaxation phase of the cardiac cycle. The activity is larger dependent on Ca^{2+} and by regulation by phospholamban(*15*) (PLB). When unphosphorylated, PLB can act as an inhibitor of SERCA. However, when phosphorylation of PLB occurs (such as during β-adrenergic stimulation(*16*)) inhibition is relieved. The PMCA is a transporter that pumps Ca^{2+} ions out of the cell using ATP hydrolysis. This mechanism is slower than NCX, but

it can operate against a large electrochemical gradient(*17*). The MCU located on the inner mitochondrial membrane allows Ca^{2+} ions to enter the mitochondria. Once inside, the Ca^{2+} can stimulate oxidative phosphorylation and ATP synthesis.

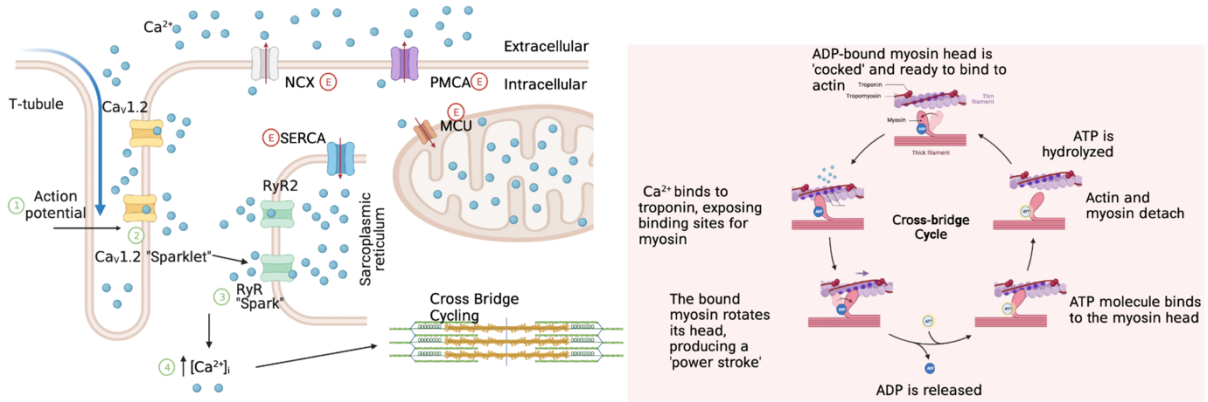

Figure 1.1 Classical view of electromechanical coupling in cardiac myocytes. Mechanisms by which the cardiac action potential initiates a contraction (1 - 4, green). Red "E" denotes Ca^{2+} extrusion mechanisms that are active during the relaxation of the heart. Events of cross bridge cycling are shown with pink background. Image created on Biorender and adapted from template by Alyson Smith.

In cardiac muscle, the sarcomere is the basic unit of contraction, composed of thin and thick filaments that interweave between α-actinin containing Z-discs. The sliding filament theory describes how the myosin and actin filaments are positioned and how this produces muscle contraction. Early studies using high resolution electron micrographs showed that during a contraction the "A" band consisting of the myosin filaments remained relatively constant in length and the "I" band, consisting of the actin filaments, would change in length(*18, 19*). The actin filaments in complex with various

proteins such as tropomyosin and troponin are anchored to the Z-discs. This alignment of actin filaments guarantees that the myosin will pull towards the center of the sarcomere and causing the distance between the Z-discs to shorten. The force generated is proportional to the number of actin-myosin interactions, “cross-bridges”. Furthermore, tension can differ depending on the filament overlap and can be visualized with tension-length curves. There is an optimum sarcomere length at which the actin-myosin filaments are sufficiently overlapped and can produce the maximum amount of tension. However, shortening or elongating the sarcomere length can decrease the tensile force as the overlap is either too close and cannot come closer or too far away to overlap(*20*).

Cross-bridge cycling is the process by which the myosin heads of thick filaments interact with the actin filaments to generate force and cause contraction of cardiac myocytes. The cardiac action potential triggers the influx of Ca^{2+} into the cytoplasm of the cardiac myocyte, which binds to the troponin complex on the actin filaments, causing a conformational change that exposes the myosin-binding sites on the actin filaments. The myosin head acts as an ATPase, hydrolyzing ATP into ADP and phosphate. In this state, the myosin head is primed to generate force in a pre-power stroke conformation. The primed myosin heads of the thick filaments bind to the exposed myosin-binding sites on the actin filaments, forming cross-bridges.
The myosin heads undergo a conformational change, releasing ADP and phosphate and generating force that pulls the actin filaments towards the center of the sarcomere, shortening the sarcomere and causing contraction of the myocyte. ATP binds to the

myosin head, causing it to detach from the actin filament. The hydrolysis of ATP into ADP and phosphate provides the energy for the myosin head to reset to its original conformational state, allowing it to form a new cross-bridge with the actin filament and repeat the cycle.

1.3 The vasculature

Blood vessels serve as conduits for blood, oxygen, nutrients, and waste delivery to and from the body's tissues. This system, and its regulatory components, are responsible for changing blood distribution as necessitated by the metabolic needs of various tissues in response to physiological and pathological conditions. The vasculature can be divided into three major groups – arterial vessels which carry blood away from the heart, venous vessels which return blood to the heart and capillaries which are the sites for exchange of oxygen, nutrients and waste(*21*). When blood is pumped out of the heart to the systemic circulation, it first travels from the aorta, a large conducting arterial outlet of the heart, to the conduit arterial branches followed by resistance arteries and arterioles. At this point, blood enters the microcirculation flowing from arterioles into the capillaries at each target tissue. The capillaries consist of a single layer of endothelial cells which permit the rapid exchange of oxygen, nutrients, and waste. Blood then begins the return trip to the heart, first through microcirculatory venules which merge into the larger veins, finally entering the right side of the heart through the vena cava. Blood is then pumped into the pulmonary arterial circulation which transports the deoxygenated blood to the lungs. Gas exchange occurs at the capillary/alveoli interface of the lung reoxygenating the blood and removes carbon dioxide. The blood is first returned to the left atrium via

the pulmonary veins, then into the left ventricle for transport back out into the systemic circulation via the systemic arterial network.

1.3.1 Blood flow through the vasculature

Contraction of the heart first propels blood into larger arteries leading to their distension. The aorta and large conducting or conduit arteries are more elastic in nature(*21*). The elastic recoil of the walls during ventricular relaxation continues the propulsion of blood forward so that blood flow in continuous. As the artery network branches into the resistance artery and arteriole levels, the vessels narrow and the composition of the walls decrease in elasticity and become more muscular (*22*). Branching of the arteries in the systemic circulation allows blood to be pumped through parallel arrangements of vessels. This ensures that all organs receive blood of the same composition from the source, such that no one organ receives blood that has passed through another organ. In addition, an increase in branching concomitant with decrease in vessel diameter, results in a large surface area of perfusion, an ability to independently regulate blood perfusion to each organ and tight control of systemic blood pressure. This final point is largely relevant in resistance arteries and arterioles, highlighted below.

The main function of the capillaries is to facilitate the movement of gases, nutrients, and wastes. They are ideally suited for exchange of materials via diffusion for numerous reasons. First, the walls of capillaries are made of a single layer of endothelial cells providing a short route for diffusion. Second, capillaries are narrow, often only wide enough for a single blood cell to flow through, so blood content is in close contact to the

wall. Third, every cell is extremely close to a capillary so distance from blood to target cell is short. Fourth, capillaries are vastly branched with a large total surface area for exchange. Finally, blood flows very slowly in the capillary network which allows for a greater amount of time for exchange. Blood then flows out of the capillaries into the venules.

The venous system receives blood from the capillary beds and returns it back to the heart. Capillaries first drain into venules, which lead into small veins exiting the organ and increasingly converge into larger veins as it gets closer to the heart. The vessels of the venous system are often termed capacitance vessels or as a blood reservoir because of their storage capacity and high distensibility. They typically are larger radii, low-resistance passageways as compared to arteries. A key physical characteristic for many of these vessels is the presence of one-way valves which prevent blood from flowing back toward the tissue. Although they can also be modulated via systemic controls the remainder of the dissertation will not be focused on these vessels.

Blood flow through the vasculature is largely dependent on the pressure gradient and the vascular resistance. Flow, or volume per unit time, is directly proportional to the pressure gradient and inversely proportional to the vascular resistance ($F=\Delta P/R$), where F = flow, ΔP = pressure gradient and R = vascular resistance. Contraction of the heart imparts pressure to the heart and is the main driving force through the vessel. As blood travels through the system, flow begins to decrease due to frictional losses and pressure drops throughout the vessels length. Resistance is the measure of the

hindrance or opposition to the blood moving through the vessel and relies on three factors: viscosity of blood, vessel length and vessel radius. Blood viscosity is generally relatively constant but can change depending on blood composition. Vessel length (i.e., total surface area of the vasculature) does not considerably change beat to beat so it has little overall effect on the resistance in an idealized system. Therefore, the largest determinant of resistance to flow is the vessel's radius. Blood can more easily move through a vessel with a larger radius since the surface area at which the blood is contact with the vessel (a frictional resistance) is much lower than in smaller vessels. All these factors can be integrated into Poiseuille's law: Flow rate = $\pi*\Delta P*r^4/8n\imath$. Critically, resistance is inversely proportional to the radius to the fourth power. Therefore, tight diameter control particularly at the resistance arteries can have profound effects on total peripheral resistance and redistribution of blood to tissues where needed.

1.3.2 Vasculature Anatomy

All blood vessels share a common layered structure. The tunica intima is a single layer of endothelial cells that form an inner tube of the vessel and that has important regulatory roles of vascular diameter. The second layer, termed the tunica media, is formed by the smooth muscle and smooth-muscle related cells which are the contractile elements that set the diameter of the vessel. The smooth muscle-endothelial cell interaction is critical to vessel function, repair, and remodeling. The final layer, tunica adventitia, is formed by the extracellular matrix, fibroblasts, and nerve cells which add another source of regulation and control. The composition and structure of each layer differs depending on vascular region.

1.3.3 The endothelium

The endothelium is a single layer of cells that line the entire vascular system(*23, 24*). In addition to providing a barrier between blood and vessel, the endothelium serves a myriad of roles including the regulation of vessel diameter, vascular growth, proliferation of smooth muscle, and the blood clotting process(*23*).

A primary function of endothelial cells is its role in permeability. The endothelium is semipermeable and allows for passive transport of solutes or mediated transport of larger substances. The physical structure between endothelial cells can vary creating a variety of conditions for the passage of compounds from vasculature to tissue(*25*). Tight junctions between endothelial cells, as seen in arteries or at the blood brain barrier, allow for precise control of passage of compounds(*26, 27*). In these cases, smaller substances such as ions, glucose or amino acids can readily pass whereas larger substances such as proteins cannot. In contrast, in many capillary beds, pores or fenestrations exist between endothelial cells which provides less resistance to movement of water-soluble substances or larger molecules.

Endothelial cells are a dynamic cell type that respond to various hormones, neurotransmitters, and vasoactive factors communicating between themselves but also conveying these responses to the overlaying smooth muscle cells. The overall endothelium function and communication with smooth muscle can vary in function and structure depending on vascular bed(*28*). Gap junctions between endothelial cells

enable the electrical coupling between adjacent cells, allowing ion channel-mediated alterations in membrane potential to propagate over long distances along the endothelial tube that lines arterioles and that comprises capillaries(*29-31*). Furthermore, hetero-cellular gap junctions allow endothelial cells to be electrically coupled to smooth muscle cells in arterioles and pericytes in capillaries, enabling electrical signals generated by endothelial cell ion channels to propagate to overlying mural cells, thereby modulating smooth muscle or pericyte contractile activity. In arteries and arterioles, these junctions are termed myoendothelial projections (MEPS)(*32-34*).

The protrusions of MEPS, mostly of the endothelium cell(*35*), are structurally similar to a nervous system synapse and are observed mainly in smaller arteries and arterioles, although they have been noted in veins(*36*). The expression of gap junctions suggests that passageway for chemical and electrical signals that are key for fine-tuned control of vasomotor function(*37*). Additionally, these connections occur at invaginations of the smooth muscle membrane called caveolae creating signaling hubs that bring together key scaffold and ion channel proteins such as AKAP150 and TRPV4(*38*). These MEPs are widely considered as a signaling microdomain that is critical of the localization and concentrating of cell-signaling partners.

The endothelium also has an important role in vessel diameter regulation by synthesizing and releasing various vasoactive factors such as nitric oxide or endothelin 1 that effect the overlying smooth muscle. Nitric oxide (NO) is a potent vasodilatory activator that is a result of the conversion of L-arginine by nitric oxide synthase (NOS).

NO production can be stimulated by changes in blood flow or chemical signals. NO can freely diffuse from the endothelial cell to the smooth muscle cells activating guanylate cyclase, increasing the production of cyclic guanosine monophosphate (cGMP) which can activate downstream protein kinases(*39*). Downstream NO related pathway targets that induce artery dilation include protein kinase G (PKG) inhibition of calcium channels(*40*) or modulation of K^+ channels(*41*) which oppose constriction of the muscle(*42*). Endothelin-1 (ET-1) is a potent vasoconstrictor produced by the endothelial cells in response to inflammation or low oxygen levels. ET-1 activation stimulates the influx of Ca^{2+} and contraction of the muscle via a phospholipase C – IP_3 receptor mediated event(*43*).

Immense work has uncovered a key vasodilatory signaling pathway in endothelial cells via activation of intermediate (IK_{Ca}) or small (SK_{Ca}) conductance Ca^{2+} activated K^+ channels(*44, 45*) by TRPV4, TRPA1 and IP_3R Ca^{2+} signaling(*46-49*). Binding of vasodilator agonists to Gαq-coupled receptors initiates endothelium-dependent, agonist-induced vasodilation. The activation of these receptors triggers phospholipase C β (PLCβ), which leads to the breakdown of membrane phosphatidylinositol 4,5-bisphosphate (PIP_2) into inositol 1,4,5 trisphosphate (IP_3) and diacylglycerol (DAG)(*50*). IP_3 produced during this process binds to IP_3 receptors (IP_3R) located in the endoplasmic reticulum membrane, increasing their sensitivity to activation by cytosolic Ca^{2+} and leading to Ca^{2+}-induced Ca^{2+}-release(*51, 52*). These local subplasmalemmal increases in Ca^{2+}, DAG-activated protein kinase C(*49*), and reduced membrane PIP_2 levels(*53*) activate clusters of TRPV4 channels located in MEPs(*49, 54, 55*). In cerebral

arterioles, TRPA1 channels also shown to be expressed in this microdomain(*56-58*). The activation of TRPV4 (or TRPA1) channels, IP_3Rs, and other ion channels by vasodilator agonists causes increases in intracellular Ca^{2+} concentration, which in turn activate IK_{Ca} and SK_{Ca} channels. The activation of these channels leads to K^+ efflux from the cells and membrane hyperpolarization, ultimately resulting in endothelium-dependent vasodilation(*49, 59*).

Emerging evidence suggests that capillaries, themselves consisting of a single layer of endothelium, act as a sensory network regulating blood flow to meet the metabolic demands of the tissue. These studies have primarily focused on the role of the capillary in the context of neurovascular coupling (NVC). NVC is the process by which neuronal activity in the brain is matched with local changes in cerebral blood flow and is a critical process that ensures the adequate delivery of oxygen and nutrients to active brain regions. These studies showed that capillary endothelial cells exposed to elevated extracellular K^+, as what would be experienced during enhanced neuronal activity, initiates a retrograde, propagating, hyperpolarizing signal that travels endothelial to endothelial cell, dilating upstream arterioles to increase local blood flow to the capillary bed(*60*). This signaling is mediated by inward-rectifier K^+ channel ($K_{IR}2.1$)(*60*), and regulated by $K_{ATP(61)}$, PIP_2 and GPCR modulation(*53*). For many years, it was believed that the increase in blood flow triggered by neuronal activity was primarily caused by the relaxation of smooth muscle cells around arterioles, directing oxygen and glucose supply to active neurons(*62-67*). However, recent findings indicate that the dilation of

capillaries, rather than arterioles, is responsible for much of the flow increase(*68*). As such work soon focused on the role of pericytes.

Pericytes, which project around capillaries within a transitional region after arterioles, differentially constrict to determine the morphology of capillary junctions and regulate branch-specific blood flow(*69*). Pericytes first described by Rouget(*70*) in 1873 as "rouge cells," and were later renamed pericytes by Zimmermann(*71*) in 1923, are specialized cells that are situated periodically along the walls of capillaries covering 30-90% of the microvessel wall(*72, 73*). Studies within the central nervous system show they play vital roles in a range of physiological processes, including blood vessel formation, maintenance of the blood-brain barrier, regulation of immune cell entry into the central nervous system, and the control of cerebral blood flow(*74*). In response to increased neuronal activity, capillaries under the presence of pericytes dilated before that of the arteriole(*75*) implying the capillary dilation was a result of pericyte relaxation. It is proposed that this dilation is regulated through the relaxation of contractile pericytes(*75-79*).

Although the majority of the work has focused on this signaling unit in the brain or retina, there is evidence that for similar mechanism through the systemic vasculature. Zhao et al.(*80*) observed that K_{ATP} channels are highly expressed in cardiac ventricular myocytes and play a crucial role in sensing the metabolic state of myocytes and transmitting a negative feedback signal electrically to upstream elements. This electro-metabolic voltage signal is immediately communicated through gap junctions to

neighboring cellular components in the microvascular network, where it regulates contractile pericytes and smooth muscle cells to modulate blood flow. Together, these studies highlight the importance of functional hyperemia, coupling tissue activity to vessel function.

1.4 Smooth Muscle Cells

There are two classes of smooth muscle: multi-unit and unitary. Multi-unit smooth muscle functions similarly to skeletal muscle in that the muscle tension is graded by variation in the number of active units. This type of muscle is highly innervated and typically in areas that require fine control such as in the eye. Unitary smooth muscle contains cells that tightly couple so that electrical signals can propagate cell to cell which allows for a synchronized response. Unitary muscle can have phasic behavior, with slow rhythmic contractions, or act tonically which produces a continuous contraction. The electrical signals can also vary in smooth muscle. For instance, in certain venule beds, action potential firing leads to a phasic contractile response(*81, 82*). However, in tonic unitary smooth muscle, such as in resistance arteries, action potentials are not the driving electrical signal. Instead, changes in intravascular pressure led to graded changes in membrane potentials(*83, 84*). Smooth muscle cells in the vasculature wrap around the endothelial layer in a helical arrangement and can be anywhere from a single layer in arterioles up to 20 layers in conduit arteries(*24*).

1.4.1 Mechanisms of arterial smooth muscle contraction and relaxation

For this dissertation, we will be focusing on small resistance arteries located in the murine mesentery. The mesentery is a recently classified organ(*85, 86*) involved in the storage of fat and which arteries of this organ supply blood to both small and large intestine. Approximately 25% of the body's cardiac output is delivered via arteries of the mesenteric, making them a major contributor to and a great model for total peripheral resistance and blood pressure regulation(*87*). Upon dissection of this arterial bed, a clear branching pattern becomes visible. The main artery is termed the first order branch, increasing in classification number at each bifurcation point. The small resistance arteries that we study are of the third or fourth order which are made up of up to six layers of smooth muscle cells and internal layer of endothelial cells. The contractile state of smooth muscle cells determines the diameter of the vessels, contracting to narrow arteries and dilate to expand. Critical to arterial function is the ability to shunt and reappropriate blood to areas of need. Physiologically, this process is exemplified through functional hyperemia, where blood flow is increased to tissues that exhibit an increased metabolic rate or in reactive hyperemia where an ischemic event results in an increase in blood flow to an area that receives an inadequate amount of blood perfusion.

Resistance arteries have a unique intrinsic autoregulatory ability to respond to changes in intravascular pressure. In the absence of neural or hormonal influences, arteries can constrict or dilate to maintain an adequate blood flow despite changes in perfusion pressure. The process termed myogenic tone, was initially described by William Bayless in 1902(*88*). Increases in intravascular pressure will induce an increase in vessel

diameter. With sustained pressure, the vessel will respond by contracting to return the vessel to the original or smaller diameter. This response is crucial for maintenance of a relatively constant blood flow to organs despite changes of intravascular pressure and can be fine-tuned depending on a tissue's metabolic needs (**Figure 1.2**).

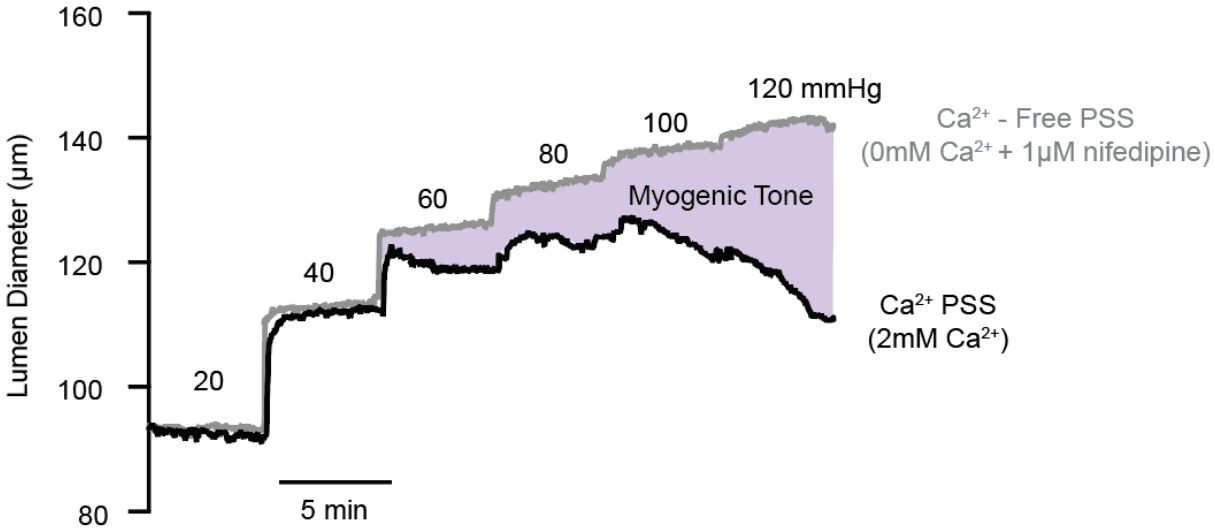

Figure 1.2 Myogenic response of a small resistance artery. Representative diameter recording of a vessel in 2 mM Ca^{2+} physiological saline solution (PSS, black trace) and the same vessel upon incubation in Ca^{2+}-free PSS with 1μM nifedipine (gray trace). Intravascular pressure steps are denoted above the traces. Shaded purple region denotes active myogenic constriction. Figure adapted from unpublished data collected by Matsumoto, C.

Electro-mechanical coupling is a process that is critical for the myogenic response and maintenance of myogenic tone (**Figure 1.3**). Although this process does rely on changes in membrane potential, arterial smooth muscle does not require an action

potential like skeletal or cardiac muscle to elicit a response. Instead, increases in intravascular pressure stretch the plasma membrane which activates Na^+ channel TRPC6, melastatin-type TRPM4 and TRPP1 (PKD2) channels resulting in the depolarization of the plasma membrane(*89-91*). This depolarization activates voltage gated, dihydropyridine sensitive, L-type $Ca_V1.2$ calcium channels. $Ca_V1.2$ channel activation results in a small, localized calcium event termed a “sparklet” (*92-94*). Summation of nearby sparklets leads to a global increase in intracellular calcium which is available for the contractile process.

Individual smooth muscle cells are long, spindle-like and do not have striations, therefore contractile elements are organized differently than those of cardiac muscle. In smooth muscle, the contractile proteins actin and myosin are not arranged into well-defined sarcomeres like they are in cardiac muscle. Instead, they are scattered throughout the cytoplasm of the smooth muscle cell in a more disorganized pattern. The thin filaments of smooth muscle are composed of actin and regulatory proteins such as caldesmon and calponin, and thick filaments composed of myosin. The actin filaments are attached to dense bodies, which are like the Z-discs in skeletal muscle but are dispersed throughout the cytoplasm. The myosin filaments are interspersed among the actin filaments and are attached to the dense bodies by intermediate filaments. The dense bodies and intermediate filaments provide structural support and help to anchor the contractile proteins in place. Contraction of smooth muscle pulls these dense bodies together shortening the cell. Despite irregular patterning compared to striated muscle, the tension-length relationship is smooth muscle is consistent with that of straited

muscle suggesting that the sliding filament theory is still upheld (*95*). The lack of a well-defined sarcomere structure in smooth muscle allows for more flexibility in the degree and pattern of contraction and allows for smooth muscle cells to contract over a wide range of lengths and shapes.

EC-coupling in smooth muscle myocytes shares many commonalities as well as differences with EC coupling in ventricular myocytes. Instead of binding troponin C, free intracellular Ca^{2+} ions bind to calmodulin (CaM), activates myosin light chain kinase (MLCK) which phosphorylates the regulatory light chain (RLC) site on the myosin head, hydrolyzes ATP into ADP and a phosphate, activating the filament for binding to actin and cross-bridge formation(*96*). Like in cardiomyocytes, the dissociation of the phosphate group results in a conformational change in the myosin head creating the power stroke. When a new ATP molecule binds the myosin head, the myosin-actin complex detaches. Hydrolysis of the ATP into ADP and phosphate primes the myosin head for the next cycle. The process repeats itself until the intracellular Ca^{2+} concentration falls and the RLC is dephosphorylated.

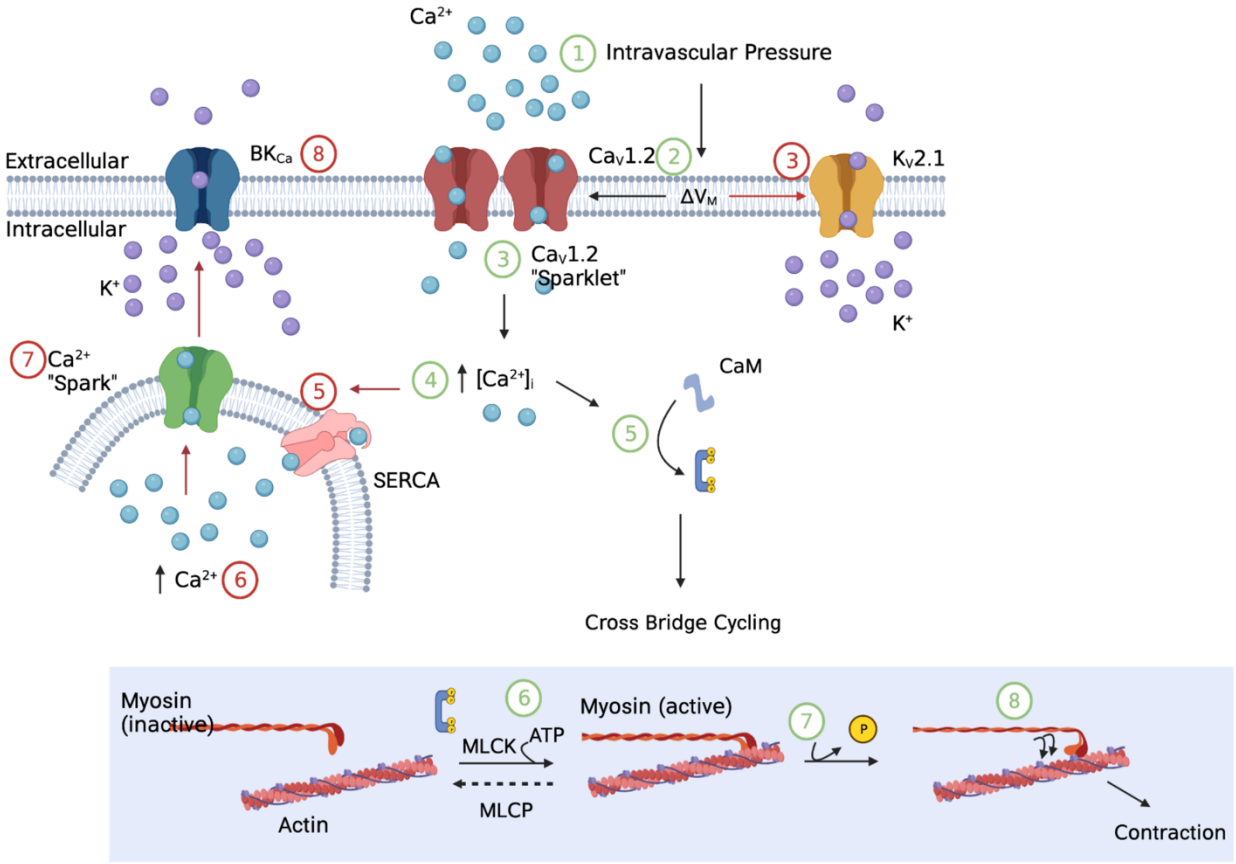

Figure 1.3 Classical view of electromechanical coupling in vascular smooth muscle. The myogenic tone pathway (1 - 8, green) as initiated by an increase in intravascular pressure. Negative feedback regulation via voltage-gated ion channels, which respond directly to changes in membrane potential (3, red), or by calcium-activated BK_{Ca} channel activity resulting from an increase in SR Ca^{2+} load (5 - 8, denoted in red), are represented by red numbers. Image created using Biorender.

Myogenic tone serves as a starting point for vessel diameter but can be regulated via endothelial-cell signaling, circulating metabolites, neurotransmitters or hormones(*97*). Resistance artery smooth muscle contraction can also occur via a pharmaco-mechanical coupling process. The pharmaco-mechanical coupling process primarily

occurs via G-protein coupled receptor (GPCR) signaling pathways that can result in either dilation or contraction without much effect on the membrane potential (*98, 99*). Various ligands can initiate the signaling pathway which include but are not limited to hormones, circulating peptides, neurotransmitters, and enzymes. GPCR activation leads to increased cytosolic Ca^{2+} concentrations or changes in phosphorylation states for the contractile machinery, without directly affecting the membrane potential or voltage-activated channels. For example, angiotensin II, a circulating metabolite, is a potent vasoconstrictor and has implicated in several disease states such as hypertension(*100, 101*). Furthermore, the angiotensin II receptor has proposed to be involved in the myogenic process with a noncanonical role as a mechanosensitive receptor(*102, 103*). Likewise, the sympathetic nervous system can influence myogenic tone by releasing norepinephrine which binds alpha-adrenergic receptors.

The two major negative feedback regulation mechanisms to regulate vascular tone in mesenteric arteries are the activation of voltage gated (K_V) potassium channels $K_V2.1$ and $K_V1.5$ and the large-conductance, calcium activated potassium channels (BK_{Ca}).(*104-106*) These channels play a role in hyperpolarizing the membrane which decreases $Ca_V1.2$ channel activity and intracellular Ca^{2+} concentrations leading to vasodilation. K_V channels are activated with membrane depolarization, inducing an efflux of potassium from inside the cell and ultimately hyperpolarization of the membrane. BK_{Ca} channels can be modulated by voltage and Ca^{2+} with each stimuli capable of sensitizing K^+ efflux. For the Ca^{2+} sensitive activation, BK_{Ca} channel activity is dependent on ryanodine receptors in the membrane of sarcoplasmic reticulum.

Deeper discussion on the biophysics and physiological role of these channels follows below.

Finally, myogenic tone is not consistent among all vessels. Studies suggest that within the arterial network, the myogenic response increases as vessel diameter decreases(*107*). Furthermore, studies have shown that veins and venules are capable of a myogenic response(*108*), however, the arteries and arterioles are the primary level where this regulation occurs and the site where the greatest resistance is generated.

1.5 Ion channels in the membrane of arterial smooth muscle

Numerous ion channels underlie the intrinsic electrical properties of excitable cells. Each channel has a highly selective pore which allows passage of specific ion across the membrane. These pores can move from an open or closed state, transitioning between the two is referred to channel gating, and are based on the conformational changes of the channel in response to changes in membrane potential. Upon opening, the select ions move down their electrochemical gradients. The major players consist of channels selective for Ca^{2+}, Na^{+} or K^{+} but others ion-selective channels exist.

1.5.1 Voltage-gated calcium channels

Calcium is a critical and highly regulated second messenger and the movement of this ion plays diverse roles from setting membrane potential to signal transduction in all cell types. One key family of ion channels for calcium movement into and out of the cell are voltage-gated calcium channels (VGCC). These channels have been shown to be

involved in muscle contraction, secretion, gene expression, synaptic transmission, and action potential firing(*109-111*). VGCCs encompass a large family of channels encoded by 10 genes split into three families: Ca_V1 (L-type), Ca_V2 (P/Q, N, R Type) and Ca_V3 (T type)(*112*). Each family of VGCC has distinct pharmacological profiles, however, to separate the members within each family is difficult via experimentation. Therefore, classification of individual VGCCs tend to focus on the genetic identification and where the channels are expressed. VGCCs share a common structure of an α1, α2δ and β subunit with a γ subunit in some cases(*112*).

A specific VGCC, $Ca_V1.2$, is critical to arterial smooth muscle function(*84, 113, 114*). The channel is referred to as L-type, dihydropyridine sensitive and voltage-gated $Ca_V1.2$ channel because it requires a higher depolarization, exhibits long-lasting activity (L-type) and is pharmacologically blocked by organic antagonists that include dihydropyridines, phenylalkylamines and benzothiazepines. Recent cryo-electron microscopy has revealed a structural model of family member $Ca_V1.1$ (*115, 116*) that aid in the understanding on excitation-contraction coupling and channel function. Although this specific channel is responsible for excitation-contraction coupling in skeletal muscle, the structural arrangement is believed to be conserved throughout eukaryotic Ca_V and Na_V channel families(*117*). Cryo-EM structures of the channel, determined at 3.6 and 4.2Å resolution(*115, 116*), found the pore-forming alpha unit in complex with a transmembrane γ-, cytosolic β- and extracellular $\alpha_2\delta$-subunits sitting at 170Å height and 100Å at its widest point. The α1 subunit is the pore-forming subunit composed of four homologous domains (I-IV) each containing six transmembrane

domains (S1-S6), an NH2-, and a COOH-terminus(*109*). The voltage sensor is formed by S1-S4 while S5-S6 is the pore forming region(*118*). The N- and C- termini contain important regulatory binding sites that include phosphorylation sites, calmodulin binding sites and IQ domains. Each auxiliary subunit plays important roles in ion conduction, membrane expression and channel function. The β subunit is important for channel activity and for targeting of the channel to the plasma membrane(*119*). The $\alpha_2\delta$ subunit comprises an extracellular α_2 and membrane spanning δ subunit connected by a disulfide bond and has an important role in channel activity(*120*) as supported by cryo-EM structures showing α2-α1 subunit interaction at the voltage sensing domain I(*115*). Furthermore, the γ subunit is the subject of increased study and has varying reported functions(*121, 122*) yet has been proposed to alter channel conductance(*115*) (**Figure 1.4**).

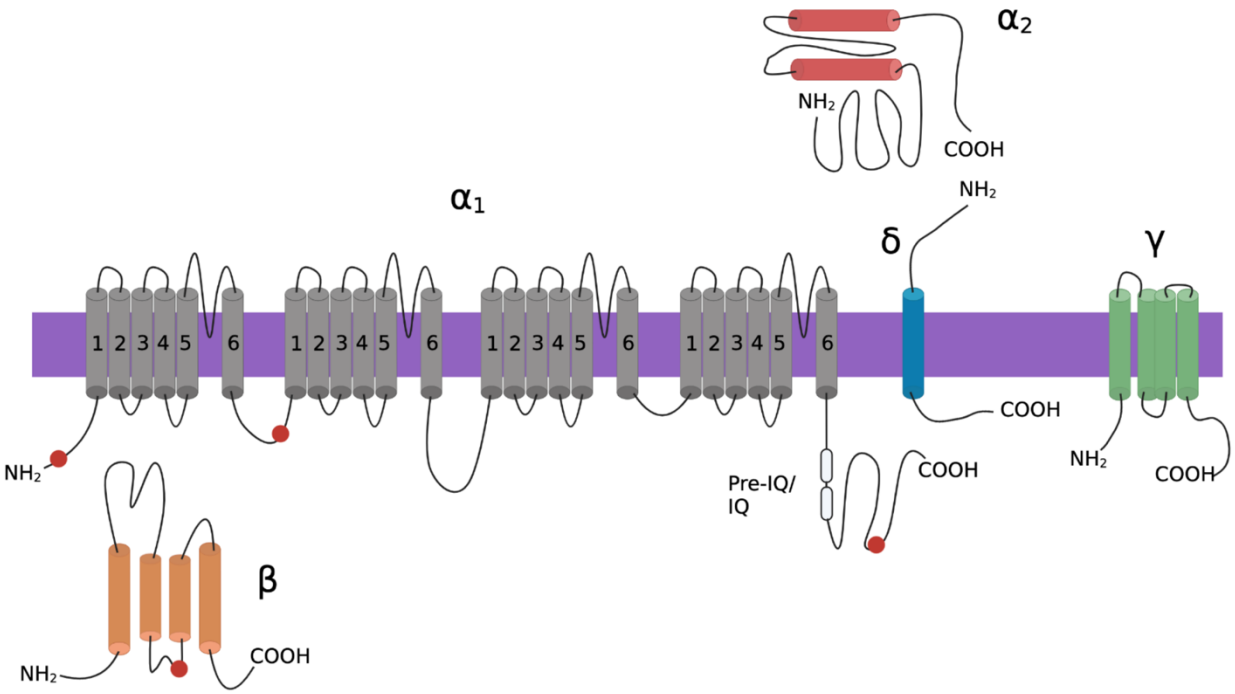

Figure 1.4 Structure and subunit composition of voltage-gated Ca^{2+} channels. The α1 subunit (gray), β subunit (orange), $\alpha_2\delta$ subunit (red and blue), and γ subunit (green) are depicted in this model of voltage-gated Ca^{2+} channel structure and subunit composition. Key phosphorylation sites of protein kinases throughout the α1 and β subunits are denoted by red dots. Pre-IQ and IQ domains are represented by ovals. This image has been adapted and modified from Keef, Hume, and Zhong.

There is emerging data that suggest T-type calcium channels (TTCC) participate in arterial tone regulation(*123-127*). TTCC alpha subunits $Ca_V3.1$, $Ca_V3.2$, and $Ca_V3.3$ that have been identified in vascular smooth muscle across different vascular beds(*123, 127*). The structure of the TTCC α1 subunit is like other VGCCs, but so far, no auxiliary subunits have been identified in association with TTCC. However, studies suggest that TTCC activity can be influenced by other proteins, including LTCC auxiliary subunits(*128, 129*). TTCCs are activated by low voltages, have fast-activating and fast-inactivating currents, have relatively small unitary conductance, and are relatively insensitive to agents that block L-type other high voltage activated Ca^{2+} channels(*127*). Of note, the inhibition of TTCCs had a weaker effect on myogenic tone compared to LTCC blockade, but it was most significant at lower pressures when the vessels were hyperpolarized(*123*) suggesting TTCCs may have a larger role at these lower pressures.

Research on rat mesenteric small arteries and arterioles investigated the function of TTCCs in regulating vascular smooth muscle reactivity. Although larger vessels

expressed both $Ca_V1.2$ and Ca_V3s, it was found that TTCCs in arterioles (vessels smaller than 40 μM), were primarily involved in vasoconstrictor responses since they lacked expression of $Ca_V1.2$. Thus, TTCCs appear to play a significant role in arterial constriction in these vessels(*130*). Studies have demonstrated that the activity of $Ca_V3.1$ and $Ca_V3.3$ channels is implicated in pressure-induced constriction in the cerebral vasculature(*124-126*). Intriguingly, when wild-type rat cerebral arteries were selectively inhibited with micromolar Ni^{2+} concentration, it led to depolarization and constriction, suggesting the involvement of $Ca_V3.2$ channels(*124*). Immunogold labeling in electron tomography of rat cerebral vascular smooth muscle (VSM) showed the presence of microdomains containing caveolae and sarcoplasmic reticulum (SR), with localization of $Ca_V3.2$ and RyR to these microdomains(*124*). Studies have suggested that a Ca^{2+} signaling network is established by caveolae, which enables $Ca_V3.2$-mediated Ca^{2+} influx to activate RyR receptors. This activation leads to the opening of Ca^{2+}-activated potassium channels, which results in membrane potential hyperpolarization(*124-126*). As a result, the separation of microdomains allows for the regulation of arterial tone by $Ca_V3.2$, which modulates the RyR-BK_{Ca} channel axis. Although important to consider the role of TTCCs, the remaining of the dissertation will focus on $Ca_V1.2$ channels.

1.5.2 Biophysical properties of $Ca_V1.2$

$Ca_V1.2$ activation requires a strong depolarization to open resulting in an inward current of extracellular Ca^{2+}. Membrane depolarization shifts the voltage sensor of the α1 subunit opening the channel pore. $Ca_V1.2$ is quickly activated and long lasting where a relatively slow voltage dependent inactivation (VDI) occurs(*131*) in addition to Ca^{2+}

dependent inactivation (CDI)(*132, 133*). CDI serves as a protective mechanism by which Ca^{2+} entry can be terminated preventing Ca^{2+} overload and related toxicity. This protective mechanism occurs when calmodulin, a Ca^{2+} binding regulatory protein, binds both the pre-IQ and IQ domains within the C-terminus of the channel, resulting in inactivation of the channel(*131*). This calcium regulatory process seems to occur at a local level rather than via a global Ca^{2+} signal, as this CDI can be seen at the single channel level(*134*).

$Ca_V1.2$ is also the target of various regulatory mechanisms which include protein kinase C (PKC) and protein kinase A (PKA) both of which reversibly phosphorylate serine and threonine residues along the various subunits of the channel(*135, 136*). PKC phosphorylation via Gq-protein coupled receptor signaling enhances $Ca_V1.2$ activity and results in the constriction of arterial smooth muscle(*135, 136*). This regulation is required for basal and persistent sparklet activity, as inhibition of PKC reduces $Ca_V1.2$ activity and $[Ca^{2+}]_i$. The effect of cAMP-PKA signaling cascade in arterial smooth muscle is much more complex as studies have proposed both a stimulatory and inhibitory effect(*136*).

1.5.3 $Ca_V1.2$ in arterial smooth muscle

Significant work has shown the important role $Ca_V1.2$ plays in regulated calcium influx and is critical to the myogenic response in VSMCs(*84, 137, 138*). Incubation of arteries in $Ca_V1.2$ antagonist nifedipine has no effect on membrane depolarization yet prevents pressure-induced arterial constriction, instead resulting in dilation of the vessel(*83, 84*).

Knock out of $Ca_V1.2$ is embryonic lethal(*139*), however, studies of smooth muscle-specific knockout of $Ca_V1.2$ in mice showed a decrease in mean arterial pressure and the inability/severely hampered ability to develop myogenic tone(*140*).

Research of $Ca_V1.2$ channel biophysics have elucidated key aspects of Ca^{2+} dynamics in these cells (**Figure 1.5**). Critically important in mesenteric smooth muscle is the relationship between voltage-dependent calcium channels and a sustained cytosolic calcium level. Early work proposed a "window current", at which sustained depolarizations within a set range of voltages can elicit steady-state Ca^{2+} levels(*138, 141*). The activation curve of $Ca_V1.2$ represents the probability that the channel will be in its open state at a given membrane potential. This curve has a sigmoidal shape, meaning that the probability of the channel being open increases rapidly as the membrane potential becomes more positive, reaches a maximum value, and then plateaus as the membrane potential becomes even more positive. The inactivation curve represents the probability that the channel will be in its closed, inactivated state at a given membrane potential. Also sigmoidal in shape, probability of inactivation decreases rapidly as the membrane potential becomes more positive, reaches a maximum value, and then levels off as the membrane potential becomes even more positive. The overlap of these two curves denotes a range of potentials at which steady state current inactivation is incomplete therefore steady-state calcium flux can occur.

To illustrate this phenomenon, Fleischman and colleagues(*138*) showed that short depolarizations (250 ms) of fura2-AM loaded cells to voltages within this window current

range, produced inward Ca^{2+} currents that were small or nonexistent and no appreciable change in intracellular Ca^{2+} concentration. However, sustained depolarizations of 60 seconds to these voltages did elicit a gradual increase in intracellular Ca^{2+} concentrations to a steady state that was sustained for the duration of the depolarization. At more positive steps where the channel can be maximally activated, a short depolarization elicited a large current concomitant with a rise in intracellular Ca^{2+}(*138*). A sustained depolarization to these more positive membrane potentials led to a transient inward current and transient increase in intracellular Ca^{2+} concentrations which could not be sustained for the duration of the depolarization. Therefore, the range of the window current suggests membrane potentials at which the channel can be constitutively active.

Quantitative measurements of these channels, by combination of both single channel and whole cell Ca^{2+} currents, further dissected the role of $Ca_V1.2$ activity in the development and maintenance of myogenic tone(*141*). Experimental measures of the factors in the equation $I = iNP_O$ has been used to $Ca_V1.2$ channels characteristics in arterial smooth muscle cells. This study determined the open probability (P_O) of $Ca_V1.2$ channels at physiological membrane potentials ranged from 3.4×10^{-4} to 2×10^{-3} at -40 mV and -20 mV, respectively. Additionally, using peak whole cell current, recorded unitary current i, and P_O, the approximate number of $Ca_V1.2$ channels could be calculated. Interestingly, this calculation determined that only 1-10 channels are open at the physiological potentials(*141*). Taken together, evidence supports the notion that at the physiological membrane potentials in smooth muscle cells (-55 mV to -35 mV)

populations of that a relatively low number of $Ca_V1.2$ channels can be constitutively active and have profound effects on calcium dynamics.

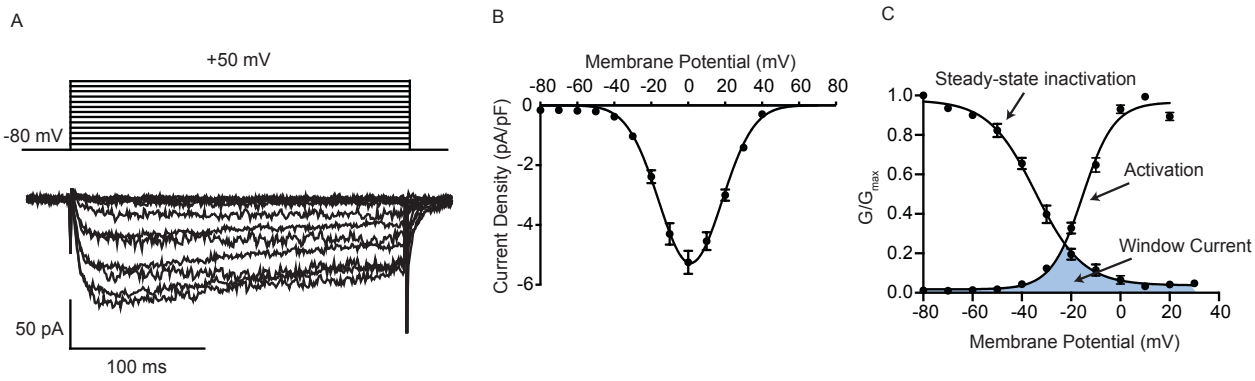

Figure 1.5 Biophysical properties of $Ca_V1.2$ channels in arterial smooth muscle. Representative $Ca_V1.2$ currents in mesenteric arterial smooth muscle measured over a range of voltages (-80 mV to +50 mV). Voltage dependence of $I_{CaV1.2}$ at membrane potentials ranging from -80 to +50 mV. Plots of $Ca_V1.2$ activation and steady-state inactivation. The area under the curves shaded in blue represent the window current. Figure adapted from unpublished data acquired by Matsumoto, C and O'Dwyer, S.

1.5.4 Functional coupling of $Ca_V1.2$

$Ca_V1.2$ channels stochastically form clusters in the membrane of excitable cells which is important in the channel's ability to functionally couple(*142*). In these clusters of typically 2-5 channels, the C-termini of adjacent channels physically interact(*143*). This positive cooperativity results in the coordinated opening of multiple, tethered channels, amplifying Ca^{2+} entry compared to that of random opening of independently gated channels(*143*). This is physiologically relevant since functional coupling can be tuned by local changes in intracellular calcium and can be dysregulated under pathological

conditions(*144, 145*). Functional coupling, also termed coupled gating, is dynamic as $Ca_V1.2$ interactions can be regulated by a local or global Ca^{2+} signal (**Figure 1.6**). At rest, when the membrane is at negative membrane potentials and low intracellular Ca^{2+} concentrations, the open probability of $Ca_V1.2$ is low therefore there is little interaction between adjacent channels. Upon membrane depolarization, $Ca_V1.2$ channels open elevating intracellular Ca^{2+} concentrations which bind calmodulin in the cytosol. The Ca^{2+}-calmodulin complex can bind to the pre-IQ domain of the C-terminal of $Ca_V1.2$ channels which promotes a physical interaction between adjacent channels enabling the functional coupling process. This functional coupling increases the activity of the adjoined channel, amplifying Ca^{2+} influx. As intracellular Ca^{2+} concentrations begin to fall, the channels can remain in a primed state. If the membrane is depolarized while in this primed state, the amplification of Ca^{2+} would be immediate. However, if the Ca^{2+} levels remain at resting levels beyond the lifetime of the primed state, the coupling dissolves and the cycle begins again(*146*).

In arterial smooth muscle, $Ca_V1.2$ channels produce persistent sparklets over a range of physiological membrane potentials. This persistent phenomenon of high channel activity has been linked to the coupled gating and could account for as much as 50% of the Ca^{2+} influx in pressurized arteries (*92-94, 113, 147, 148*). Furthermore, $Ca_V1.2$ channel gating is potentiated in hypertensive states resulting in increased myogenic tone and blood pressure(*144*). Although coupled gating plays a critical role in smooth muscle activity, little is known on how $Ca_V1.2$ clusters are formed and maintained. It does appear that clustering of $Ca_V1.2$ channels themselves are not affected by cooperative

gating. For example, removal of the C-termini of the channel results in similar cluster sizes to WT(*146*). Further research is needed to understand the mechanism behind this phenomenon and its role in arterial smooth muscle physiology.

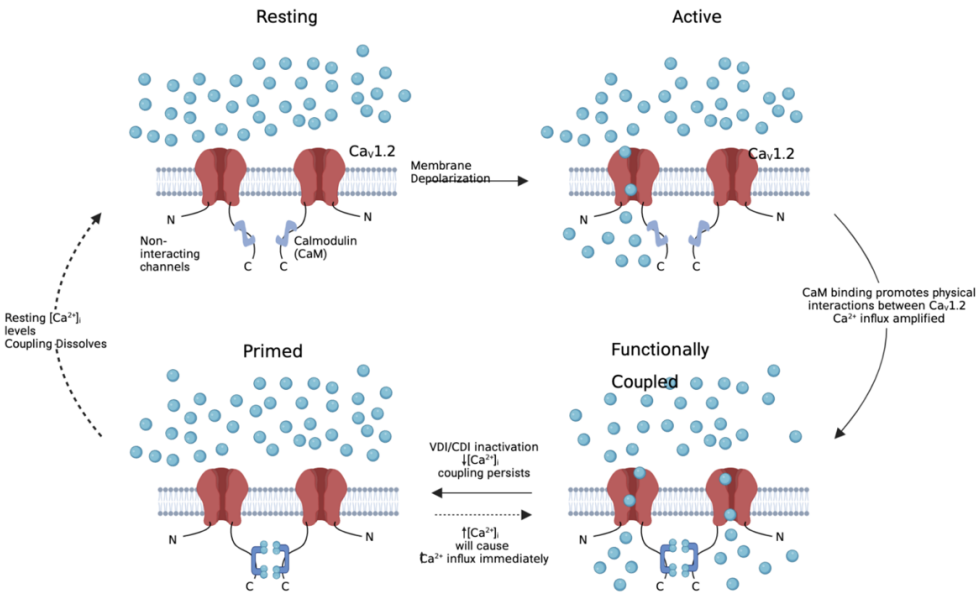

Figure 1.6 Model of functional coupling in $Ca_V1.2$ channels. $Ca_V1.2$ channels in a cluster at resting membrane potentials (top left). During depolarization, open probability of $Ca_V1.2$ increases allowing external Ca^{2+} to flow through the channels into the cell. Ca^{2+} binding to calmodulin is increased (top right). Calmodulin binding facilitates physical interaction between $Ca_V1.2$ channels. Functional coupling increases activity of connected channels and Ca^{2+} influx into cell (bottom right). Voltage- and calcium-dependent inactivation decrease $[Ca^{2+}]_i$ yet $Ca_V1.2$ stay coupled for a period of time (bottom left). If membrane depolarization occurs within that time-frame Ca^{2+} amplification will occur immediately. Otherwise, coupled channels will disband and the cycle will restart. Adapted from Dixon et al.(*146*).

1.5.5 Voltage-gated potassium channels

Potassium ion concentrations are key to cell homeostasis and play critical roles in several biological processes. Potassium is the major cation inside the cell whose movement is associated with setting of resting membrane potentials or as a key regulator of action potentials. One key family of potassium channels are the voltage-gated potassium (K_V) channels. They have been divided into twelve large subfamilies (K_V1-12)(*149*) encoding dozens of distinct α subunits that contain the pore-forming and voltage sensing transmembrane domains which assemble as homo- or hetero-tetramers(*150*). Channel activity and functional characteristics are formed by a wide variety of combinations of subunits that allow for distinct properties. Nomenclature has varied over time, however now follows KCN* nomenclature as assigned by the UCL/HGNC/HUGO Human Gene Nomenclature(*151*). Each α unit has 6 transmembrane segments (S1-S6) with S4 serving as a voltage-sensing domain, the P-loop between S5-S6 as the pore-forming domain and a myriad of N- and C- terminal cytoplasmic domains as revealed in the crystal structure of K_V1 (Shaker) channel at a resolution of 2.9Å(*152*). In vascular smooth muscle, the expression profile of members from K_V channel family depends on the tissue type and vascular bed. In mesenteric arteries specifically expresses a variety of family members including BK_{Ca}, K_V1.2, K_V1.5, K_V2 and K_V9.3(*105, 153-156*) suggesting that this family of channels is critical in hyperpolarization of the membrane and serving as a key regulator in arterial smooth muscle(*157*).

1.5.6 K_V2.1 in arterial smooth muscle

Although murine mesenteric smooth muscle expresses several K_V family members, the focus of this dissertation is on K_V2.1(*158*). K_V2.1 channels specifically have been shown in arterial smooth muscle to comprise ~50% of K_V current and blockade of the channel induces enhanced myogenic constriction in pressurized arteries(*105, 153, 157*). Pharmacological inhibition of K_V2.1 with stromatoxin in intact arterioles induced a robust constriction suggesting K_V2.1 plays a critical role in maintenance of myogenic tone(*105, 157*) (**Figure 1.7**). The functional K_V channel is formed by a tetramer of α subunits or in complex with an electrically silent K_V9 subunits. K_V9's are an electrically silent channel subunit that do not form homo-tetramers at the membrane but instead form complexes with K_V2.1 to modulate activity and function(*159*). When found in complex, the voltage activation of K_V2.1/K_V9.3 channels exhibited shifts to more hyperpolarized potentials compared to homo-tetramers of K_V1 or K_V2.1 channels(*157*). Together this suggests that these K_V2.1/K_V9.3 complexes could play a role in regulation of myogenic tone over lower and wider range of membrane potentials and pressures and would argue for the importance of the study of K_V2.1 channels in the vasculature.

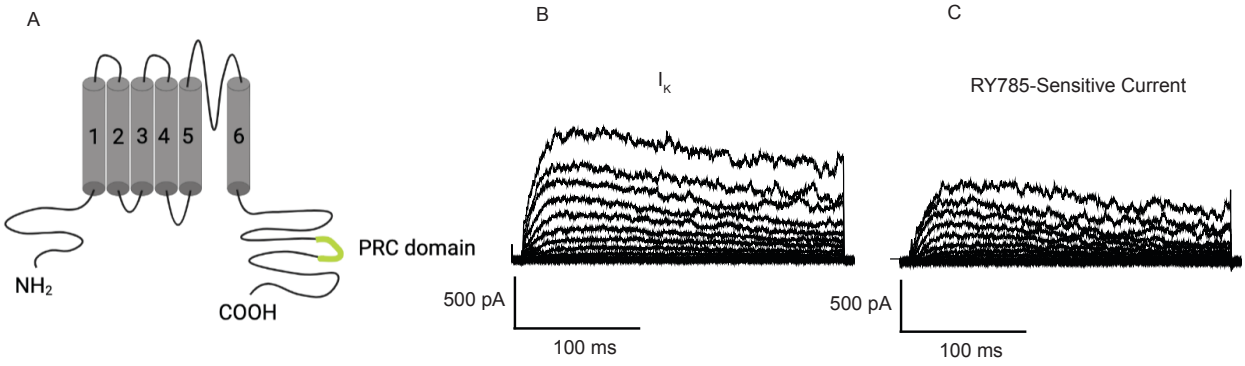

Figure 1.7 Structure of K_V2.1 and representative traces. (A) The α1 subunit (gray) of K_V2.1. The proximal restriction and clustering signal domain is denoted in green. (B)

Representative total K^+ (I_K) and RY785 sensitive ($K_V2.1$ currents) in mesenteric arterial smooth muscle measured over a range of voltages (-80mV to +50 mV). (C) Voltage dependence of I_K and $K_V2.1$ at membrane potentials ranging from -80 to +50 mV. Figure adapted from unpublished data acquired by Matsumoto, C.

$K_V2.1$ is unique in that it forms large, high-density clusters at the surface of the plasma membrane observed in many cell types and tissues (i.e. neurons(*160, 161*), transfected COS1 (*162, 163*), HEK293 cells, pancreatic β cells). The proximal restriction and clustering (PRC) domain, a 26 amino acid targeting domain that includes 4 critical amino acids(*164*) located within the C-terminus of $K_V2.1$ channels, is critical for localization and clustering of the channel(*151*). This state of clustering is dynamic, forming or dissolving depending on different states of the cell. The phosphorylation state of the channel is critical to this clustering phenotype. For instance, in response to ischemia or elevated intracellular Ca^{2+} concentrations, $K_V2.1$ channels within the plasma membrane are dephosphorylated, reducing the clustering and appearing more uniform in distribution within the membrane(*165, 166*). Additionally, this dissolution of $K_V2.1$ macro-clusters has functional consequences for the channel. De-phosphorylated and therefore de-clustered $K_V2.1$ channels exhibit a hyperpolarized shift in voltage dependence(*165, 167*) suggesting a potential mechanism for effects on clustered state of the channel and function.

Studies have also proposed that the majority of $K_V2.1$ channels in the membrane are non-conducting and instead have non-canonical functions(*168-170*). For instance, $K_V2.1$

serves to help anchor the plasma membrane to the endoplasmic reticulum forming junctions (ER-PM junctions) with the plasma membrane that are independent of potassium conductance. $K_V2.1$ expression in the PM can affect the ER-PM junctional sites via phosphorylation states of interacting proteins VAPA and VAPB(*171*). It has also been shown to be involved in a signaling microdomain with $Ca_V1.2$ and ryanodine receptors. The ability to remodel of the ER-PM junctions by $K_V2.1$ is unaffected by the conduction potential of the channel, instead important for clustering and contact sites is the PRC domain(*172*).

1.6 Other important ion channels in smooth muscle physiology

Although the focus on the dissertation will be on $Ca_V1.2$ and $K_V2.1$, it is also recognized that there are several other ion channels that are key to regulation of smooth muscle physiology.

1.6.1 Ryanodine receptors

Ryanodine receptors (RyR) are large homo-tetramers located in the membrane of the endoplasmic reticulum, a specialized membrane system that stores and releases Ca^{2+}, that are ryanodine-sensitive and Ca^{2+} selective(*155*). There are three isoforms of RyR (RyR1, RyR2 and RyR3) that share high sequence homology(*173*) but expression changes regionally and depending on vascular bed(*174*). Cryo-EM studies show a mushroom shaped structure with a large (~80% of entire mass) cytosolic cap and a transmembrane stalk(*175*). Each RyR subunit contains six transmembrane domains (S1-S6), a calcium selective pore formed by S6, a large N-terminal tail and a smaller C-

tail, together forming the Ca^{2+} sensor, binding sites of interacting partners and numerous sites for channel regulation(*176*). RyR are Ca^{2+} sensitive and can be activated at low Ca^{2+} concentrations(*177*), inhibited at higher Ca^{2+}concentrations(*177*), or effected by SR Ca^{2+} load(*178*). These receptors are also regulated via phosphorylation(*176*) or by interacting partners such as calmodulin.

In both skeletal and cardiac myocytes, RyR are critical for increase cytosolic Ca^{2+} concentrations for muscle contraction as explained in the CICR process. Although CICR has been shown to occur in particular smooth muscle of various tissues(*179, 180*), the focus of this section will be on the negative feedback role of RyR that has been shown to occur in arterial smooth muscle cells and the myogenic tone process(*104*). Ca^{2+} influx through a clusters of ryanodine receptor was first “sparks” by Heping Cheng and colleagues in 1993(*12*). Since then, immense work has been undertaken to understand the role of spark activity in arterial smooth muscle. Alone, these localized increase in Ca^{2+} do not significantly raise the global Ca^{2+} levels(*181*). Spark activity instead has been linked to BK_{Ca} channel activity, such that each spark has an associated a spontaneous transient outward currents (STOCs)(*104*). These STOCs can be visualized as outward transients which hyperpolarize the membrane, deactivating $Ca_V1.2$ channels, reducing myogenic tone and causing dilation of the artery. Pharmacological blockade of RyR results in silencing of STOCs and BK_{Ca} inhibition therefore establishing this interaction(*12, 104, 182*).

1.6.2 BK_{Ca} channels

Another ion channel critical for homeostatic feedback of vascular smooth muscle is the BK_{Ca} channel. This channel encoded by the KCNMA1 gene is also referred to as Maxi-K, calcium sensitive BK, Slo1 or $K_{Ca}1.1$. As some of these names imply, the channel is voltage and Ca^{2+} sensitive, outwardly rectifying K^+ current with a large unitary conductance. Studies suggest that smooth muscle BK_{Ca} channels are also mechanosensitive(*183*).

BK_{Ca} channels are formed by a tetramer of alpha subunits(*184*) that have six transmembrane domains (S1-S6) that is highly conserved with K_V channels(*185*). However, these channels also have a distinct S0 region which makes the N-terminal extracellular (*185*) and a long cytosolic C-tail which includes several regulatory sites. Importantly, the long C-tail contains two regions called the regulator of conductance for K+ (RCK1 and RCK2) which are high affinity Ca^{2+} binding sites as well as a low affinity Mg^{2+} binding site, all key to the calcium sensitivity of the channel(*186*). Additionally, BK_{Ca} channels are often associated with two transmembrane BK_{Ca} beta subunits. Although four types of β subunits have been identified, β1 appears to be the most highly expressed in resistance arteries(*187*). BK_{Ca} channel association with this subunit has profound effects, altering gating kinetics and increasing the calcium sensitivity(*188, 189*).

Cryo-EM structural studies of the BK_{Ca} channel have revealed several unique functions for the channel in addition to confirming the structure above. For instance, the high K^+ conductance may be attributed to the large funnel like opening below the selectivity

pore with additional lateral openings that shorten the path and reduce the resistance for K^+ ion movement(*190*). Structures within the funnel opening also has a number of electronegative residues which attract the K^+ ions(*190*). The structure also confirms the existence of three ion-binding sites as predicted in other electrophysiological studies(*190*). Furthermore, additional structural studies propose that the gating ring and voltage censors are directly linked, which may allow for the coupling of membrane voltage and Ca^{2+} sensors(*191*).

Physiologically, BK_{Ca} channel activation is an important feedback mechanism for vascular contraction. Membrane depolarization in addition to increases in intracellular Ca^{2+} activate BK_{Ca} channels which are critical for maintaining resting membrane potential(*192*). Pharmacological blockade of BK_{Ca} channels enhanced myogenic tone in mesenteric smooth muscle(*193, 194*). The BK_{Ca} channel's sensitivity and regulation by Ca^{2+} is key to channel function. Global intracellular Ca^{2+} concentrations in smooth muscle range from ~100 to 300 nM which is below the threshold required to significantly increase the open probability of the channel(*182, 195*). However, local intracellular Ca^{2+} signals from the ryanodine receptors (sparks, as mentioned in above section) can raise Ca^{2+} concentrations enough to elicit a BK_{Ca} response(*104*). Key to this model is the close juxtaposition of approximately 20 nm, of RyR within the SR to BK_{Ca} channels in the membrane. The opening of a single RYR or cluster of RYRs can lead to a localized increase in Ca^{2+} that can reach between 4-30 μM which activate BK_{Ca} channels creating a large macroscopic K^+ current(*195*). This K^+ efflux from the cell is one regulatory feedback mechanism employed by the cell and have been identified as spontaneous

transient outward currents (STOCs)(*196*). Pharmacological dissection of the coupling of these two channels imply that BK_{Ca} channel activity is controlled by the spark activity of RyRs(*104*). In this study, blockage of BK_{Ca} with TEA or iberiotoxin or inhibition of RyR with ryanodine led to similar levels of constriction(*104*).

BK_{Ca} channel activators are effective vasodilators and ablation of the beta subunit enhances myogenic tone. This channel and its subtype is a target of many pharmacological studies that have vast number of naturally occurring regulators. Pharmacological block of BK_{Ca} channels in arterial smooth muscle by iberiotoxin results in membrane depolarization and constriction of the artery. Inhibiting sparks, or efflux of Ca^{2+} from the SR via RyR, also results in membrane depolarization and vascular constriction, further illustrating the relationship of BK_{Ca}, RyR and VSMCs.

The α-subunit of BK_{Ca} channels is frequently associated with modulatory β subunits, which modify channel gating kinetics and increase the Ca^{2+} sensitivity of the α-subunit(*197-199*). Variations in the coupling of α and β subunits of BK_{Ca} channels may contribute to the observed heterogeneity of Ca^{2+} sensitivity of these channels in vascular SMCs from different vascular beds(*200*). Research in artery smooth muscle cells has revealed that the majority of α subunits of BK_{Ca} channels are located in the plasma membrane, while β1 subunits are situated in Rab11A positive recycling endosomes. The β1 subunits can rapidly transport to the plasma membrane and associate with α subunits, providing a dynamic mechanism for modulating the activity of BK_{Ca} channels(*201*). Under pathological conditions, the β1 subunit of BK_{Ca} channels

plays a role in regulating excitability and contractility. In various models of hypertension, the expression of this subunit is reduced, leading to impaired BK_{Ca} channel function and in coupling of BK_{Ca} and RyR spark signaling(*202, 203*). The calcineurin/NFATc3 signaling pathway has been identified as a mechanism for decreasing β1 expression during angiotensin II-induced hypertension. Ca^{2+} influx through L-type Ca^{2+} channels are required for down-regulation of the beta1 subunit of the BK channel, which contributes to arterial dysfunction and the development of hypertension. Remarkably, $NFATc3^{-/-}$ mice have lower systemic blood pressure, suggesting that this transcription factor plays a crucial role in the development of severe hypertension induced by chronic angiotensin II signaling activation(*203*).

1.6.3 Inositol-1,4,5-triphosphate receptor

The inositol-1,4,5-triphosphate receptor (IP_3R) is located within the membrane of the endoplasmic reticulum. It is encoded by three separate genes(*204*) and can form both homo- and heterotetrametric proteins which give rise to various functional properties(*205*). Similar to RyR, IP_3R subunits also consists of 6 transmembrane domains (S1-S6), an S5 and S6 domain that forms the ion pore, a long cytoplasmic N-terminus and a shorter cytoplasmic C-terminal tail(*206*). Like RyR, the IP_3R crystal structure revealed a large mushroom shaped protein although relatively smaller(*207*). In mammals, there are three isoforms of IP_3Rs (IP_3R1-IP_3R3)(*51*) that share approximately 60-80% homology, with highly conserved pope and ligand-binding regions(*52*). As the name suggests, IP_3Rs are activated by inositol 1,4,5 triphosphate (IP_3). IP_3 is generated from the hydrolysis of membrane phosphatidylinositol 1,4 bisphosphate (PIP_2) by

membrane associated phospholipases under the control of Gaq/11 mediated GPCR signaling. The IP_3 binding site is located on the N-terminus of each monomer at a region called the IP_3 binding core (IBC). Importantly, both IP_3 and cytosolic Ca^{2+} are required for activation of the receptor(*51*). In the absence of IP_3, Ca^{2+} is not capable of opening the channel. IP_3 binds to the IBC, modulating channel gating in a Ca^{2+} dependent manner, such that in low concentrations of IP_3, IP_3R are more sensitive to inhibition by Ca^{2+} and higher IP_3 concentrations decrease the Ca^{2+} sensitivity of inhibition.

IP_3R are important regulators of calcium signaling and smooth muscle contraction in the arterial vasculature. In SMCs, there are regional and vascular bed differences of IP_3R expression(*208*) but typically IP_3R1 appears to be the predominant isoform(*208*) in smooth muscle. In some vascular beds, IP_3 is proposed to have a central role in the generation and maintenance of myogenic tone. The current model suggests IP_3R Ca^{2+} release activates TRPM4 channels which contribute to the pressure-induced depolarization of SMCs, activation of VGCCs and ultimately contraction of the muscle. Interestingly, studies in mesenteric smooth muscle argue that IP_3 and IP_3R do not have as large of a role in the development of myogenic tone, instead suggesting that DAG produced by PLC hydrolysis of phosphatidylcholine is the key regulator(*209*). However, mesenteric arteries from hypertensive mice exhibited enhanced IP_3R expression and IP_3R-depedent Ca^{2+} release compared to normotensive mice possibly via upregulation of the channel via the calcineurin-NFAT axis(*210*). Despite this difference in the players in development of myogenic tone, we cannot completely rule out the role of IP_3R in our

cells. Under normal conditions, IP_3R could have a negligible role in myogenic tone and activity is enhanced in pathophysiological states.

1.7 Sex-differences in vasculature in health and disease

Cardiovascular disease (CVD) is a leading cause of morbidity and mortality worldwide, and there is increasing recognition that there are important sex differences in the epidemiology, pathophysiology, and clinical presentation of CVD(*211*). Hypertension is one of the leading risk factors for CVD and plays a large role in deaths caused by heart disease, stroke and renal disease supporting the importance of sex-based research of smooth muscle physiology. Women have historically been underrepresented in cardiovascular clinical trials, and as a result, most of the evidence on CVD prevention and treatment is based on studies conducted in men. However, recent studies have shown that there are important sex differences in the epidemiology of CVD. For example, women have a lower overall incidence of CVD than men, but this difference disappears after menopause(*212*). Women also have different risk factor profiles for CVD, with a greater prevalence of hypertension and diabetes, but a lower prevalence of smoking and dyslipidemia compared to men(*212, 213*). Women with CVD tend to present with different symptoms than men. For example, women are more likely to experience atypical symptoms such as fatigue, shortness of breath, nausea, and back pain rather than the classic symptoms of chest pain and arm pain that are more common in men(*214, 215*). This can lead to underdiagnosis and undertreatment of CVD in women(*215*). Clinically, cardiovascular diseases are treated differently in men and women. Women are often prescribed diuretics and beta-blockers, while men more often

receive ACE inhibitors and calcium channel blockers(*216-218*). Furthermore, multiple studies have reported that ACE inhibitors are more effective in men than women(*217-219*). These sex differences may have important implications for the development of sex-specific guidelines for CVD prevention and treatment and have important implications for the development of sex-specific diagnostic algorithms and education for healthcare providers.

There are several indications at the arterial level that ion channel activity and myogenic tone differ between males and females. Various lines of evidence propose circulating sex hormones such as estrogen as a possible explanation for these sex differences. For instance, estrogen, specifically 17βEstradiol, has been suggested to mediate vasorelaxation(*39, 220, 221*), increase BK_{Ca} channel function(*222*), and decrease $[Ca^{2+}]_i$(*223*). In intact coronary arteries, males generally exhibit enhanced myogenic tone in intact coronary arteries compared to females(*224*), however, when estrogen is present, arterial tone is significantly reduced. Considering the evident health disparities between pre- and post-menopausal women, it is crucial to conduct research on the fundamental physiological variances between male and female arterial smooth muscle under normal conditions, devoid of hormonal influence. Specific areas to be studied include whether ion channels function at different rates in one sex versus the other and whether the response of arterial smooth muscle to neurotransmitters and vasoconstrictors differs between sexes.

1.8 Goals and Hypotheses

Given the review above, the overall scope of this dissertation is to elucidate the mechanisms governing the formation of $K_V2.1$ and $Ca_V1.2$ clusters and the role of these channels in arterial myocyte physiology. Two major narratives are presented.

Aim 1*:* Assess how ion channel clusters are formed in the membrane of excitable cells.

Hypothesis: Ion channel clustering is a default mechanism of channel organization and are formed via a stochastic self-assembly mechanism

Aim 2*:* Assess the role of $K_V2.1$ macro-clusters on sex-specific differences in $Ca_V1.2$ clustering and function in arterial myocytes

Hypothesis: $K_V2.1$ forms large macro-clusters upon phosphorylation at a specific at specific site S590A, and disrupting the clustering site eliminates sex-specific differences in $Ca_V1.2$ clustering and function in arterial myocytes.

Chapter 2: Ion channels stochastically organize in the membrane of excitable cells

Note: This chapter is composed of the following published paper: Sato D et al. A stochastic model of ion channel cluster formation in the plasma membrane. Published in Journal of General Physiology. 2019 Sep 2; 151(9):1116-1134. doi: 10.1085/jgp.201912327

2.1 Abstract

Ion channels are often found arranged into dense clusters in the plasma membranes of excitable cells, but the mechanisms underlying the formation and maintenance of these functional aggregates are unknown. Here, we tested the hypothesis that channel clustering is the consequence of a stochastic self-assembly process and propose a model by which channel clusters are formed and regulated in size. Our hypothesis is based on statistical analyses of the size distributions of the channel clusters we measured in neurons, ventricular myocytes, arterial smooth muscle as well as heterologous cells, which in all cases were described by exponential functions, indicative of a Poisson process, i.e., clusters form in a continuous, independent and memory-less fashion. We were able to reproduce the observed cluster distributions of five different types of channels in the membrane of excitable and tsA-201 cells in simulations using a computer model in which channels are 'delivered' to the membrane at randomly assigned locations. The model's three parameters represent channel cluster nucleation, growth, and removal probabilities, the values of which were estimated based on our experimental measurements. We also determined the time

course of cluster formation and membrane dwell time for $Ca_V1.2$ and TRPV4 channels expressed in tsA-201 cells to constrain our model. In addition, we elaborated a more complex version of our model that incorporated a self-regulating, feedback mechanism to shape channel cluster formation. The strong inference we make from our results is that $Ca_V1.2$, $Ca_V1.3$, BK, and TRPV4 proteins are all randomly inserted in the plasma membranes of excitable cells and that they form homogeneous clusters that increase in size until they reach a steady-state. Further, it appears likely that the regulation of cluster size for both a diverse set of membrane-bound proteins and a wide range of cell types is regulated by a common feedback mechanism.

Introduction

Cell biologists have been studying the mechanisms of ion channel expression and delivery to the membrane for decades. This work has revealed key roles for the cytoskeleton, channel subunits, scaffolding proteins, and/or lipid microdomains (e.g., caveolae) in the organization of ion channels in the plasma membrane (*221, 225-229*). The process starts when messenger RNA encoding the transmembrane ion channel subunits is translated on endoplasmic reticulum (ER)-bound ribosomes from which the nascent polypeptides are translocated into the membrane. Fully assembled channel proteins leave the ER in vesicles that fuse with the *trans* Golgi, where they undergo post-translation processing, including, for many ion channel subunits, modification of N-linked glycosylation. These vesicles are transported as cargo by molecular motors traveling along microtubules that run from the *cis* side of the Golgi apparatus to the cytoplasmic surface (*229, 230*). Ion channels appear on the cell surface upon fusion of

these vesicles with the plasma membrane, which, depending on the ion channel and cell type, can occur at proximal sites or, in some cases, quite distant from where the vesicles emerged from the Golgi apparatus. Plasma membrane ion channels are eventually removed and either recycled or degraded via endocytic pathways.

The organization of ion channels has long been recognized to vary along a cell's membranous surface (*231-234*). Descriptions of the distributions of ion channels in the plasma membrane have been based on the analysis of electron micrographs (*233-237*), confocal images of cells exposed to protein-specific antibodies attached to fluorescent moieties (*238*), and, more recently, super resolution imaging (*239-244*). In most instances, it has been shown that many ion channels aggregate into dense clusters. For example, in neurons, ligand-gated ion channel proteins involved in synaptic transmission are concentrated on the dendritic and somatic membranes (*245*), whereas the voltage-gated ion channels required for the release of neurotransmitter are restricted to the axon terminals (*231, 232, 235, 246*). In striated muscle, dihydropyridine-sensitive voltage-gated Ca^{2+} channels form clusters along the sarcolemma and transverse tubules of the cells (*234, 236*). Such exquisite spatial arrangements of ion channels are critical for efficient biological functions in both neurons and muscle. Indeed, clustering of voltage-gated Ca^{2+} channels is critical for the amplification of Ca^{2+} influx that is necessary to initiate neurotransmitter release in neuronal terminals and to sustain excitation-contraction coupling in muscle. Furthermore, it has recently been demonstrated that proteins engaged in cooperative signaling cascades display co-clustering, e.g., clusters of large conductance Ca^{2+}-

activated K^+ (BK) channels are surrounded by clusters of $Ca_V1.3$ channels that generate the requisite local Ca^{2+} influx (*239, 247*). Yet, despite these advances, a broadly applicable quantitative model that amalgamates key concepts of ion channel insertion and organization in mammalian cells is lacking.

We gain some insight on the mechanisms underlying channel cluster formation from studies performed in bacteria, where time-lapse fluorescence images suggest that chemoreceptor proteins are inserted randomly into the membrane via the general protein translocation machinery of the cells and then diffuse to existing clusters (*248*). The distance between clusters, however, varied widely within cells, prompting Thiem, Kentner and Sourjik (*249*) to propose that protein cluster formation and growth is a stochastic self-assembly process in which newly synthesized proteins diffuse in the membrane and then join existing clusters or create new clusters. In their model, clusters can originate anywhere in the membrane and later become attached to scaffolding or anchoring sites. Shortly thereafter, it was reported that anchoring sites may not be required for the formation of new clusters and their simulations suggested that the periodic positioning of new clusters can emerge spontaneously in growing cells (*250*). At present, however, it is unclear whether the distribution of ion channels in the surface membrane of mammalian cells could be the result of a similar stochastic self-assembly process of protein organization.

In the work described here, we used super-resolution fluorescent microscopy to determine the sizes and densities of clusters of five different ion channel proteins

expressed in the surface membranes of ventricular myocytes ($Ca_V1.2$), smooth muscle cells ($Ca_V1.2$, TRPV4, and BK channels), neurons ($Ca_V1.3$), and tsA-201 cells ($Ca_V1.2$, $Ca_V1.3_S$, $Ca_V1.3_L$, and TRPV4 channels). We found that the probability density functions of the cluster sizes of all of these ion channels could be fit with an exponential function, a hallmark of a Poisson process. Thus, we generated a mathematical model in which vesicles containing ion channel proteins are inserted into the membrane at random locations. The model reproduced the observed steady-state clustering of $Ca_V1.2$, $Ca_V1.3$, TRPV4, and BK channels in the membranes of neurons, cardiomyocytes, smooth muscle, and tsA-201 cells. To further elaborate and constrain our model, we studied the formation and growth of clusters of $Ca_V1.2$ and TRPV4 channels expressed in tsA-201 cells, as well as the turnover rate of these channels in the membrane. We found that adding a regulatory feedback mechanism scaled to channel number enhanced its capacity of the model to reproduce our experimental observations. On the basis of our experimental and modeling results, we propose that the regulation of cluster size for both a diverse set of membrane-bound proteins and a wide range of cell types is regulated by a common feedback mechanism. Our model constitutes a novel tool for identifying potential mechanisms by which specific proteins and signaling pathways could dynamically shape membrane channel cluster formation.

2.3 Material and Methods

2.3.1 Immunofluorescence and super-resolution microscopy

We performed immunofluorescence and super resolution imaging experiments using methods similar to those described elsewhere (*239-243*). Briefly, cells were fixed at the

specified times after transfection by incubating in phosphate-buffered saline (PBS) containing 3% paraformaldehyde and 0.1% glutaraldehyde (GA) for 10 minutes at room temperature. After washing with PBS, cells were incubated with sodium borohydride (1 mg/ml) for 10 minutes at room temperature, washed again with PBS, and blocked by incubating in 3% bovine serum albumin and 0.25% v/v Triton X-100 in PBS for 1 hour at room temperature (≈20 ºC). The cells were incubated either overnight at 4˚C or for 1 hour at room temperature with anti-GFP antibody conjugated to Alexa Fluor 647 (Thermo Fisher, #A-31852) diluted in blocking buffer to a concentration of 10 µg/ml. After washing with PBS, samples were post-fixed with 0.25% GA in PBS for 10 minutes at room temperature, washed with PBS and prepared for imaging.

Coverslips were mounted on microscope slides with a round bottom cavity (NeoLab Migge Laborbedarf-Vertriebs GmbH, Germany), using fresh MEA-GLOX imaging buffer. The day of the experiment a stock of 5 ml of 100 mM MEA (cysteamine hydrochloride, Sigma-Aldrich #M6500) in PBS was prepared and pH was adjusted to 8.2 with KOH, 10M. A stock of GLOX containing 50 µl of 10 mM Tris-HCl pH 8, 3.5 mg glucose oxidase (Sigma-Aldrich #G2133), and 12.5 µl of catalase (Sigma-Aldrich C100) was prepared, sonicated for 5 minutes and centrifuged for 3 minutes at 13000 rpm at 4˚C. This stock was kept at 4˚C and used within a week. Finally, 50 ml of Buffer B, containing 200 mM Tris-HCl pH 8, 10 mM NaCl, and 10% w/v glucose was prepared, kept at 4˚C, and used within 6 months. Right before mounting the coverslip the final MEA-GLOX buffer was mixed by adding a ratio of 89:10:1 of Buffer B: MEA: GLOX. Final concentration of the components in this imaging buffer were 10 mM MEA, 0.56 mg/ml

glucose oxidase, and 34 µg/ml catalase. Coverslips were sealed with Twinsil (Picodent, Germany) and aluminum tape to reduce oxygen permeation.

Super-resolution images were generated using a super-resolution ground-state depletion system (SR-GSD, Leica) equipped with high-power lasers (488 nm, 1.4 kW/cm^2; 532 nm, 2.1 kW/cm^2; 642 nm, 2.1 kW/cm^2) and an additional 30 mW, 405 nm laser. Images were obtained using a 160× HCX Plan-Apochromat (NA 1.43) oil-immersion lens and an EMCCD camera (iXon3 897; Andor Technology). For all experiments, the camera was running in frame-transfer mode at a frame rate of 100 Hz. Fluorescence was detected through Leica high-power TIRF filter cubes (488 HP-T, 532 HP-T, 642 HP-T) with emission band-pass filters of 505-605 nm, 550-650 nm, and 660-760 nm.

Super-resolution localization images were reconstructed using the coordinates of centroids obtained by fitting single-molecule fluorescence signals with a 2D Gaussian function using LASAF software (Leica). A total of 35,000 images were used to construct the images. The localization accuracy of the system is limited by the statistical noise of photon counting. Thus, assuming the point-spread functions are Gaussian, the precision of localization is proportional to DLR/√N, where DLR is the diffraction-limited resolution of a fluorophore and N is the average number of detected photons per switching event (*251, 252*). Accordingly, we estimated a lateral localization accuracy of 16 nm for Alexa 647 (≈1900 detected photons per switching cycle).

For this paper we re-analyzed previously published super resolution images of $Ca_V1.2$ channels from ventricular myocytes (*240*) as well as $Ca_V1.3$ channels from hippocampal neurons and tsA-201 cells (*241*) and TRPV4 channels from arterial smooth muscle cells (*242, 243*). The figure legends in the present report differentiate data derived from those studies versus data derived from new experiments. Detailed experimental procedures on the treatment and imaging of the re-analyzed cells can be found in the original papers cited above.

2.3.2 tsA-201 cell transfection

tsA-201 cells (Sigma-Aldrich) were cultured in Dulbecco's Modified Eagle Medium (DMEM; Gibco) supplemented with 10% fetal bovine serum and 1% penicillin/streptomycin at 37˚C in a humidified 5% CO_2 atmosphere. Cells were plated onto 25 mm round 1.5 coverslips and transiently transfected using jetPEI (Polyplus Transfection). For the $Ca_V1.2$ experiments, cells were transfected with plasmids encoding the rabbit $Ca_V1.2$ (α_{1C}) conjugated to (600 ng), and rat auxiliary subunits $Ca_V\alpha_2\delta$ (300 ng), and $Ca_V\beta_3$ (600 ng), (kindly provided by Dr. Diane Lipscombe; Brown University, Providence, RI). For the TRPV4 experiments cells were transfected with 600 ng of a plasmid encoding the mouse TRPV4-EGFP (kindly provided by Dr. Philipp Slusallek, Saarland University, Saarbrücken, Germany) in which the GFP moiety has been mutated to prevent oligomerizarion. For photoactivation experiments, cells were transfected with $Ca_V1.2$ tagged at their C-terminus with photoactivatable GFP (GenScript, 600 ng) and auxiliary subunits stated above or TRPV4 tagged at their C-terminus with photoactivable GFP (GenScript, 600 ng).

2.3.3 Time-lapse confocal microscopy

The live-cell imaging of photoactivatable experiments were performed on an Olympus Fluoview 3000 (FV3000) confocal laser-scanning microscope equipped with an Olympus PlanApo 60x/1.40 NA oil-immersion objective. We used 405 nm laser light to photoactivate the PA-Ca_V1.2 and PA-TRPV4 channels. Pre-stimulation images were collected in order to normalize fluorescence signal. Upon excitation, robust GFP fluorescence emission was observed. Normalized fluorescence time courses were compiled by averaging line scans of various ROIs from each cell. Regions of interest were resliced and quantified over time.

2.3.4 Stochastic self-assembly model

To simulate the aggregation process of channels within cell membranes, we developed a simplified stochastic self-assembly model of cluster growth modified from stochastic self-assembly algorithms proposed for bacterial proteins and ryanodine receptors (*244, 250, 253*). As was done by Baddeley, Jayasinghe, Lam, Rossberger, Cannell and Soeller (*244*) for ryanodine receptors, our model does not consider channel diffusion for cluster formation. The observation that voltage-gated Na^+ channels in the sarcolemma of skeletal muscle fibers are immobile, suggests that lateral channel diffusion, at least in native muscle cells, may not be a significant determinant of cluster growth (*254*).

In our model, the cell membrane is represented by a 10 x 10 μm virtual two-dimensional square grid ($Grid_{ij}$). This space is subdivided into 10^6 'grid sites', each of which measures 10 x 10 nm and represents the space that can be occupied by an individual

ion channel molecule. Particles simulating ion channels were inserted randomly into the grid with cluster growth and density determined by three model parameters representing nucleation (P_n), growth (P_g), and removal (P_R) probabilities.

We first assume that at time t = 0 there are no channels present in the grid ($Grid_{ij} = 0$). Then, in each iteration, there are three processes; (1) nucleation, (2) cluster growth, (3) removal.

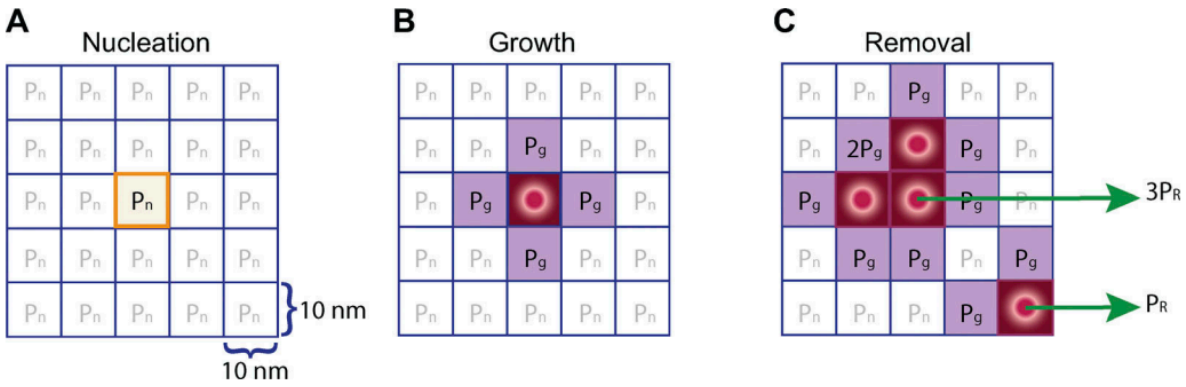

Figure 2.1 ***In silico stochastic self-assembly model.*** (A) Nucleation process. Channels are inserted into the grid randomly with nucleation probability P_n at each time step. '1' represents occupied grid sites. (B) If a nucleating channel exists, channels are randomly inserted into any one of the four available grid sites immediately adjacent to the nucleating channel with growth probability P_g at each time step. (C) After that, the growth probability of a cluster is P_g × the number of available neighbors. Clusters are randomly removed with the removal probability, P_R × the number of channels.

(1) Nucleation. Channels are inserted into the grid randomly with nucleation probability P_n at each time step (**Figure 2.1A**). In this study, each iteraion is equal to 18 seconds.

(2) Cluster growth. If a grid site becomes occupied by a channel ($Grid_{ij} = 1$) cluster growth is induced.

$$Grid_{ij} = \begin{cases} 1, & occupied \\ 0, & empty \end{cases}$$

For simplicity, cluster growth is simulated by random insertion of a channel in any one of the four available grid sites immediately adjacent to a nucleating channel with growth probability P_g at each time step (**Figure 2.1B**). Once one channel is added to the existing nucleating channel, a cluster is formed. After that, the growth probability of a cluster is $Pg \times the\ number\ of\ available\ neighbors$.

(3) Removal of clusters. Concurrently with growth, in each time step there is a removal probability, P_R, for clusters already formed on the grid. It is important to note that we have defined a cluster to be a group of two or more channels. Clusters dwell in the membrane for some time before they are recycled or degraded. Therefore, the removal probability, P_R, of a cluster increases depending on its size ($P_R \times the\ number\ of\ channels$) (**Figure 2.1C**). Because clusters will grow until they are recycled or degraded the removal probability sets a limit for maximal cluster size.

The parameters P_n, P_g, and P_R were specified using two methods. In the first, we defined probabilities P_n (t), P_g (t), and P_R (t) . The probabilities P_g (t) and P_n (t) were defined to be sigmoid functions based on a correlation between the experimental fitting of mean cluster area and density and P_g and P_n, respectively. In addition, P_R was defined to be an increasing sigmoid function to account for the observation that $Ca_V1.2$ channel internalization increases as the number of channels increases (*255*). These parameters were based on the experimental data using the time course of the distribution of cluster sizes and the values were determined by a non-linear least-squares method (**Figures 2.4 and 2.5; Table 2.1**).

In our second method, the parameters P_n, P_g, and P_R have a feedback mechanism. In this feedback model, $Ca_V1.2$ and TRPV4 expression is regulated by the number of channels. In this study, P_n, P_g, and P_R linearly increase or decrease until they reach steady state values. Then, the basic feedback model is described by the following differential equations,

$$\frac{dP_n}{dt} = r_n N\left(1 - \frac{P_n}{K_n}\right), \qquad (1)$$

$$\frac{dP_g}{dt} = r_g N\left(1 - \frac{P_g}{K_g}\right), \qquad (2)$$

$$\frac{dP_R}{dt} = r_R N\left(1 - \frac{P_R}{K_R}\right), \qquad (3)$$

where r_n, r_g, and r_R are growth rates of P_n, P_g, and P_R, respectively, and K_n, K_g, and K_R are steady state values of P_n, P_g, and P_R , respectively, and N is the number of channels per unit area.

2.4 Results

2.4.1 The distributions of $Ca_V1.2$, $Ca_V1.3$, BK and TRPV4 channel cluster sizes are fit by an exponential function

Over the last five years, our research team has been using super-resolution imaging to determine the spatial organization of Ca^{2+}-permeable and Ca^{2+}-sensitive ion channels in the surface membrane of multiple cell types. In this paper, we have re-analyzed our previously published super-resolution data on $Ca_V1.2$ channels in cardiomyocytes (Dixon, Moreno, Yuan, Opitz-Araya, Binder, Navedo and Santana (*240*), two isoforms of the $Ca_V1.3$ channel in hippocampal neurons and heterologous cells (Moreno et al., 2016), and TRPV4 channels in arterial myocytes (Tajada, Moreno, O'Dwyer, Woods, Sato, Navedo and Santana (*242*) to provide a broad, quantitative examination of how different types of channels are organized in the plasma membrane with nanometer resolution. To this extensive data set, we have added new, equivalent measurements on $Ca_V1.2$ channels and the large-conductance Ca^{2+}-activated K^+ (BK) channels in the sarcolemma of arterial myocytes. As was the case in our prior analyses, we found that the $Ca_V1.2$ channels were expressed into dense clusters of different size along the surface membrane with a mean cluster area 2488 ± 140 nm^2, similar to that we found in ventricular myocytes (2555 ± 82 nm^2; Dixon, Moreno, Yuan, Opitz-Araya, Binder,

Navedo and Santana (*240*) (**Table 2.2**). The BK channels also formed clusters along the sarcolemma of the arterial myocytes with a mean cluster area of 3008 ± 223 nm^2 .

Figure 2.2 displays samples of the super-resolution images we have generated for five different channel proteins (BK, $Ca_V1.2$, TRPV4, $Ca_V1.3_s$, and $Ca_V1.3_L$) in four different kinds of cell membranes (arterial myocytes, cardiomyocytes, hippocampal neurons and tsA-201 cells). In each case, we found that the channels are arranged into dense clusters with a wide range of sizes throughout the cell membranes. In the same figure, we have plotted the frequency distributions of cluster sizes for each of our data sets that remarkably reveal that each can be fit by a single exponential function.

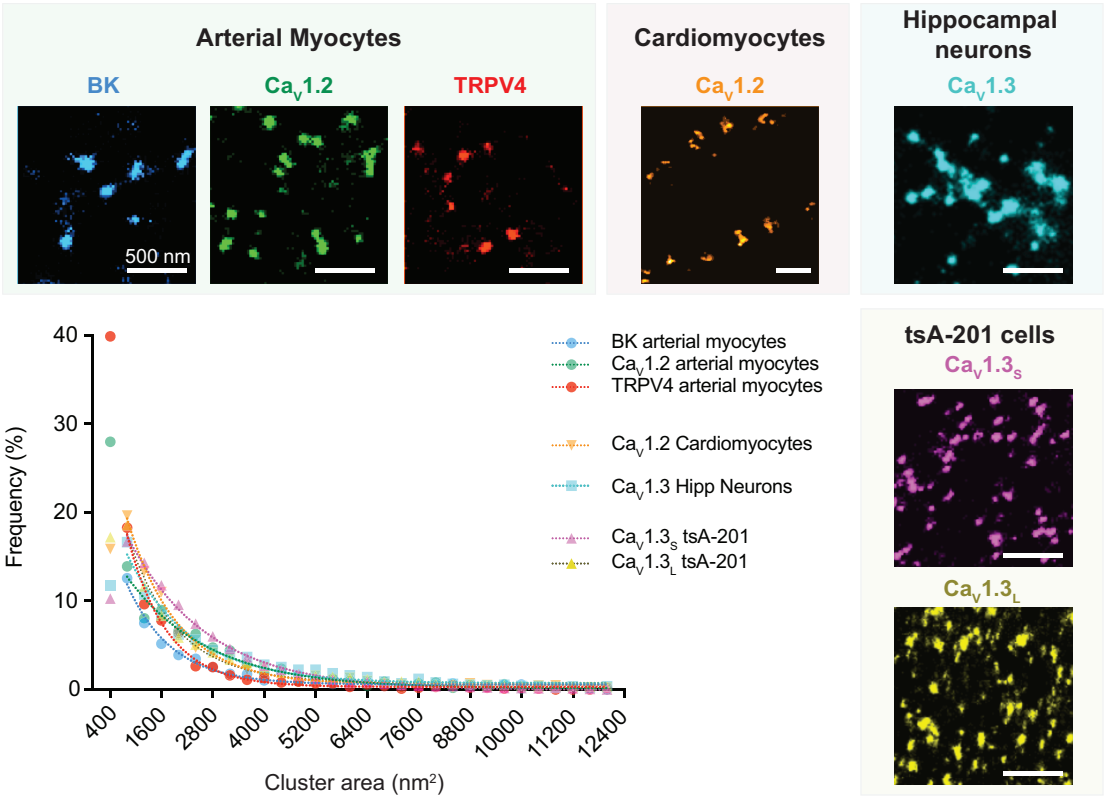

Figure 2.2 BK, $Ca_V1.2$, TRPV4, and $Ca_V1.3$ channels organize in clusters in multiple cell types exhibiting an exponential cluster area distribution.

Representative super-resolution ground state depletion images of the cluster organization of endogenous BK (blue), $Ca_V1.2$ (green), and TRPV4 (red) channels in arterial myocytes, endogenous $Ca_V1.2$ (orange) channels in cardiomyocytes, endogenous $Ca_V1.3$ (light blue) channels in hippocampal neurons, and the two splicing variants $Ca_V1.3_S$ (pink) and $Ca_V1.3_L$ (yellow) expressed in tsA-201 cells. The plot summarizes the frequency distribution of the cluster areas for each channel. All the distributions were fit with a single exponential function. Average cluster areas and densities for each channel are presented in Table 2. TRPV4 data were modified from Tajada et al. (2017), $Ca_V1.2$ in cardiomyocytes was modified from Dixon et al. (2015), and $Ca_V1.3$ data were modified from Moreno et al. (2016).

2.4.2 Stochastic self-assembly may account for the formation of homogeneous clusters of membrane channels in neurons, cardiomyocytes, and smooth muscle cells

Our finding that the size distributions of clusters for five different channel proteins could all be described by exponential functions, the hallmark of a Poisson process, strongly suggested that the clusters are formed stochastically in a continuous, independent, and memory-less fashion. A similar proposal was advanced by Wang, Wingreen and Mukhopadhyay (*250*) and Greenfield, McEvoy, Shroff, Crooks, Wingreen, Betzig and Liphardt (*253*) to account for the spatial organization of chemotactic proteins in bacterial membranes and by Baddeley, Jayasinghe, Lam, Rossberger, Cannell and Soeller (*244*) for ryanodine receptors in ventricular myocytes. To test our hypothesis, we modified the approach employed by Baddeley, Jayasinghe, Lam, Rossberger, Cannell and Soeller

(*244*) to create a new model to reproduce our cluster distributions and make testable predictions regarding plasma membrane protein organization.

Our modeling begins with the generation of a 10 x 10 μm grid composed of 10^6 pixels. The dimension of each pixel (100 nm^2) in this grid is similar to the size of individual Ca_V1 (*115*) and TRPV4 channels (*256, 257*). Particles simulating ion channels were inserted randomly into the grid with cluster growth and density determined by three model parameters representing nucleation (P_n), growth (P_g) and cluster removal (P_R). These parameters are probability functions meant to represent different biological processes. P_n is the probability that a vesicle containing an ion channel (or channels) will be randomly inserted at any site in the membrane. Nucleation is the first step in the formation of a new structure via self-assembly or self-organization. In our model, P_n values are uniform across the grid. At the beginning of the simulation, most "seeding" events involve the insertion of single channels. However, once cluster growth has initiated, the model allows for the stochastic insertion of multiple channels at any particular site. P_g is the probability of a channel to be inserted immediately adjacent to pre-existing channels. In our model, cluster growth is simulated by random insertion of a channel in any one of the four available grid sites immediately adjacent to a nucleating channel. The growth probability of a cluster is $Pg \times$ *the number of available neighbors*. Once a channel or small cluster is "seeded" in the membrane, the probability of insertion of a new channel adjacent to it increases, inducing cluster growth. The final parameter, P_R, represents the probability of a channel or cluster of channels being removed from

the membrane by endocytosis and/or degradation. Individual channels and clusters were randomly removed every iteration.

The key question was whether or not this simple model could reproduce the cluster area distributions we measured from our super-resolution images of endogenous channels in arterial myocytes, cardiomyocytes, hippocampal neurons, as well as channels expressed exogenously in tsA-201 cells. Because we could not observe the formation of the channel clusters as the cells develop, we assumed that the cluster area and density distributions we measured represented steady-state conditions and set the parameters P_n, P_g, and P_R to constant values.

As shown in **Figure 2.3,** our stochastic self-assembly model effectively reproduced the steady-state size distributions and mean cluster areas that we measured for all five channels proteins embedded in the membrane of four different cell types: arterial myocyte BK channels (**Figure 2.3A**), arterial myocyte $Ca_V1.2$ channels (**Figure 2.3B**), arterial myocyte TRPV4 channels (**Figure 2.3C**), ventricular myocyte $Ca_V1.2$ channels (**Figure 2.3D**), neuronal $Ca_V1.3$ channels (**Figure 2.3E**), tsA-201 $Ca_V1.3_L$ channels (**Figure 2.3F**), and tsA-201 $Ca_V1.3_S$ channels (**Figure 2.3G**).

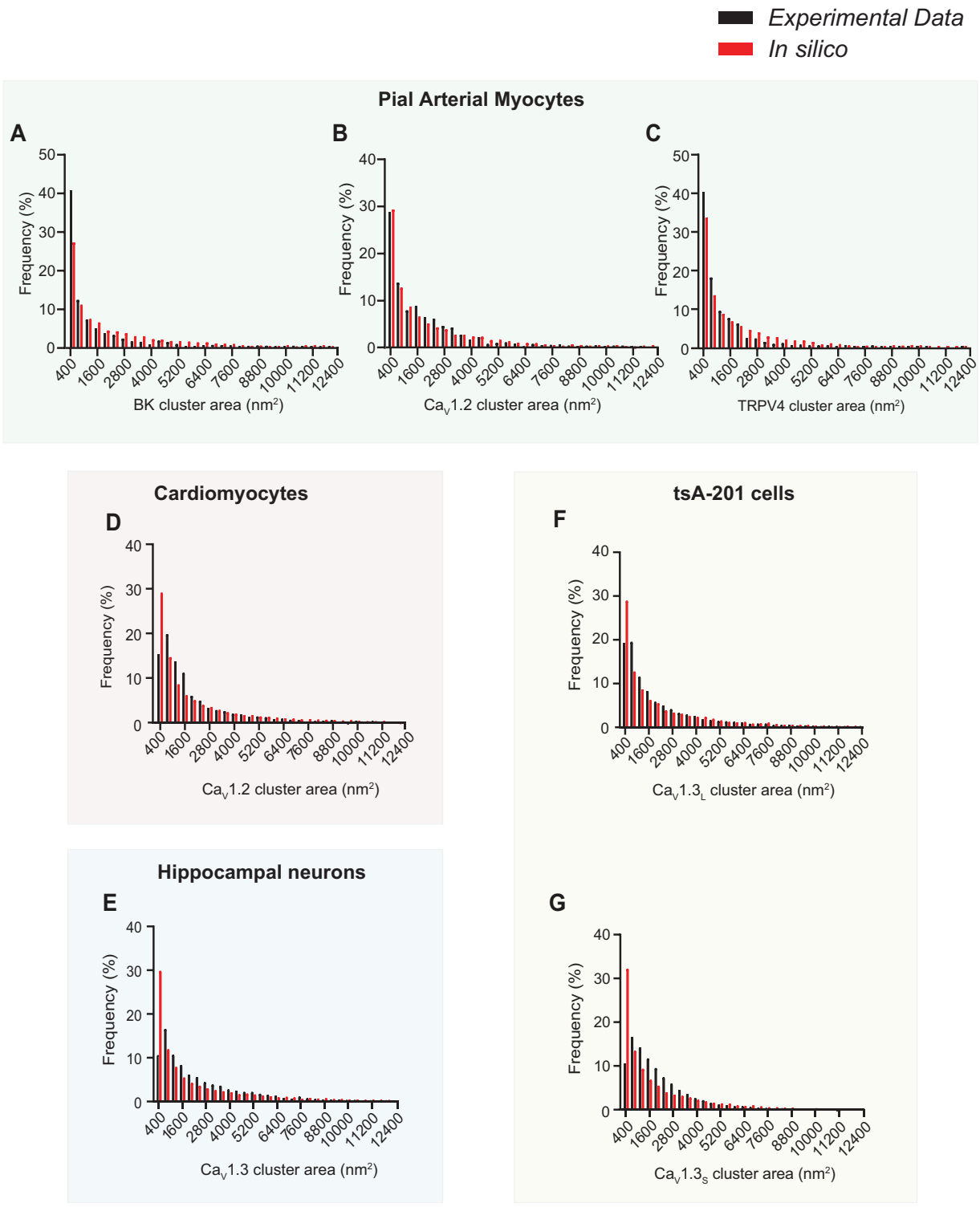

Figure 2.3 The distributions of $Ca_V1.2$, TRPV4, and BK channels in smooth muscle, $Ca_V1.2$ in ventricular myocytes, and $Ca_V1.3$ in neurons and tsA-201 cells could be explained by a stochastic self-assembly of clusters. Histograms of the

experimental (black bars) and simulated (red bars) clusters area distributions of (A) BK, (B) $Ca_V1.2$, and (C) TRPV4 channels in arterial myocytes, (D) $Ca_V1.2$ in ventricular myocytes, (E) $Ca_V1.3$ channels in hippocampal neurons, and (F) $Ca_V1.3_L$ and (G) $Ca_V1.3_S$ channels in tsA-201 cells.

2.4.3 Time-dependent assembly of $Ca_V1.2$ and TRPV4 channel clusters

As mentioned above, the super-resolution images from which we measured channel cluster sizes and densities present only a snapshot of the cell membrane. We had no information as to how the channel clusters develop and are maintained over time. To address this issue, we expressed $Ca_V1.2$-EGFP (**Figure 2.4**) or TRPV4-EGFP channels (**Figure 2.5**) in tsA-201 cells, fixed the cells at 0, 4, 6, 12, 24, 36, and 48 hours after transfection, immunolabeled the channels, and acquired super-resolution images of the channels in the membrane. These images permitted us to determine how the distribution of channel cluster sizes changed over a 48 hour period. In **Figure 2.4A**, we show super-resolution images of a tsA-201 cell at different time points following transfection with the $Ca_V1.2$-EGFP plasmid. The images were analyzed to quantify the area and densities of the $Ca_V1.2$ channel clusters (**Figure 2.4B-E**). The frequency histograms of cluster areas were generated from the images acquired at each time point. This analysis revealed that although the number of clusters varied with time, the size distributions could all be fit with single exponential functions that differed mainly in their amplitude (**Figure 2.4B**). Accordingly, histograms generated using the percentage of total clusters within each bin of cluster area were similar (**Figure 2.4C**). These data reveal that the mean size of the $Ca_V1.2$ clusters within the population of tsA-201 cells

increased rapidly over the first 12 hours post-transfection and then reached a plateau at about 24 hours (**Figure 2.4D**).These data could be fit with exponential functions with a half amplitude ($T_{1/2}$) at 5.8 hours after transfection. $Ca_V1.2$ cluster density, like mean cluster area, also reached a plateau by about 24 hours and was could be fit with a sigmoidal function with a half amplitude at 11.5 hours (**Figure 2.4E**).

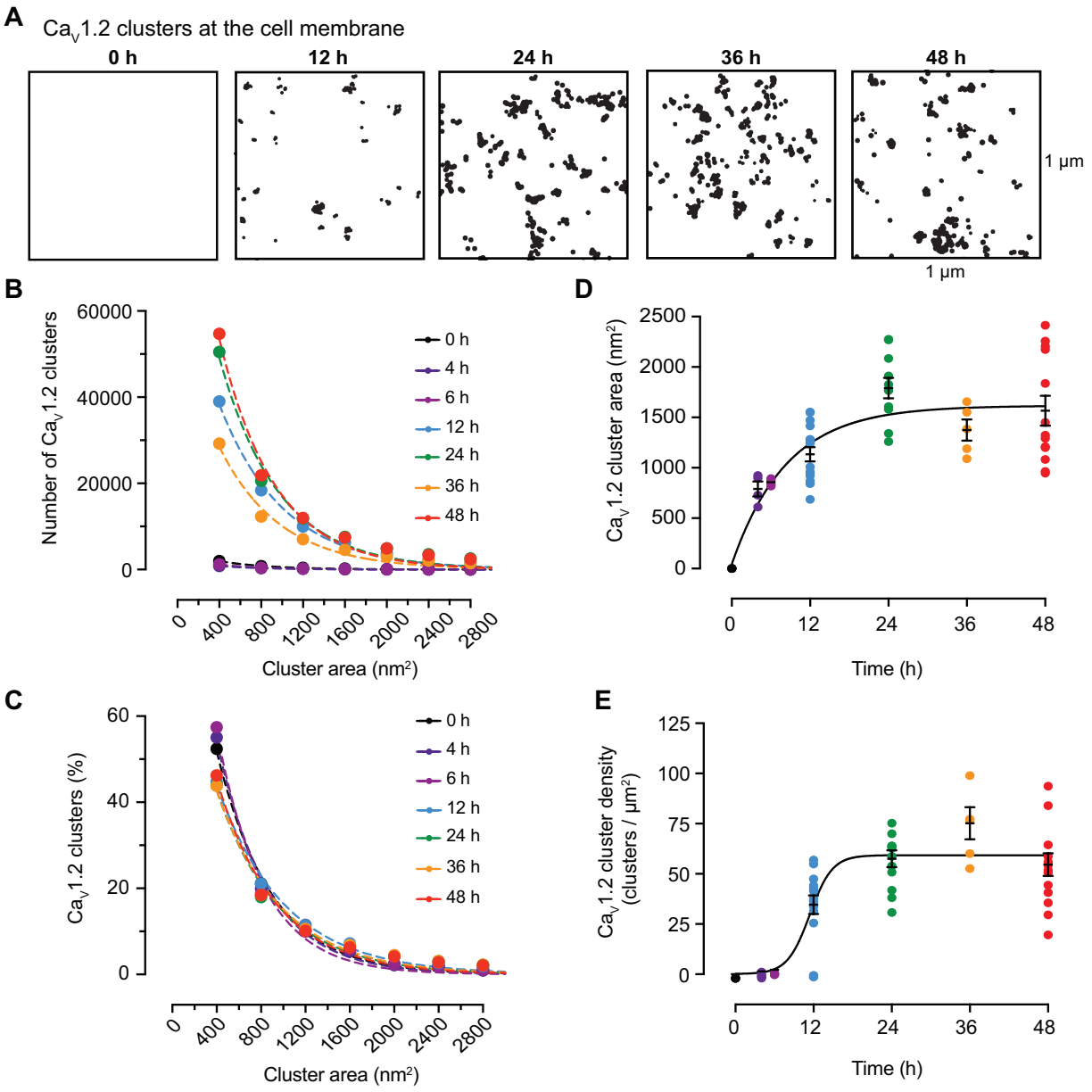

Figure 2.4 Time course of the formation of $Ca_V1.2$ channel clusters in tsA-201 cells. (A) Representative super-resolution GSD binary masks of immunolabeled $Ca_V1.2$ channels expressed in tsA-201 cells at 0, 12, 24, 36, and 48 h after transfection. (B) Frequency distribution of $Ca_V1.2$ channels cluster areas at each time point. (C) Relative frequency distribution of $Ca_V1.2$ channels cluster areas expressed as percentages. Dashed color lines in B and C represent the best single exponential decay function fit for each dataset. (D) Change of mean $Ca_V1.2$ channel cluster area at different time points after transfection. Data are presented as mean ± SEM for individual cells at each time point. Mean cluster area data were fit with a one-phase exponential equation (solid black line). The tau value of the fit is 8.37 h. (E) Change of $Ca_V1.2$ channel cluster density at different time points after transfection. Data are presented as mean ± SEM for individual cells at each time point. Mean cluster density data were fit with a sigmoidal function (solid black line). The $logIC_{50}$ fit is 11.42 h. (B–E) All data were compiled as follows: 4 h: n = 1,497 clusters from 4 cells; 6 h: n = 2,100 clusters from 4 cells; 12 h: n = 87,209 clusters from 16 cells; 24 h: n = 114,805 clusters from 11 cells; 36 h: n = 66,769 clusters from 5 cells; 48 h: n = 118,281 clusters from 13 cells.

In **Figure 2.5A**, we show super-resolution images of representative tsA-201 cells at 0, 12, 24, 36, and 48 hours after transfection with the TRPV4-EGFP plasmid. As was the case for $Ca_V1.2$ channels, the sizes of the TRPV4 clusters followed exponential distributions at each time point (**Figure 2.5B-C**). As we found for $Ca_V1.2$ channels, the mean area and density of TRPV4 channel clusters increased rapidly over a period of about 12 hours and reached a plateau at about 24 hours (**Figure 2.5D-E**). Similarly, the

TRPV4 cluster size and density data were fit with exponential functions with $T_{1/2}$ at 6.4 and 5.7 hours after transfection for cluster size and cluster density, respectively. The common finding that the cluster sizes and cluster densities of these two types of channels increase rapidly over a short period following transfection and expression, but then reach a steady state, suggests the presence of a regulatory, feedback mechanism controlling channel cluster size and density.

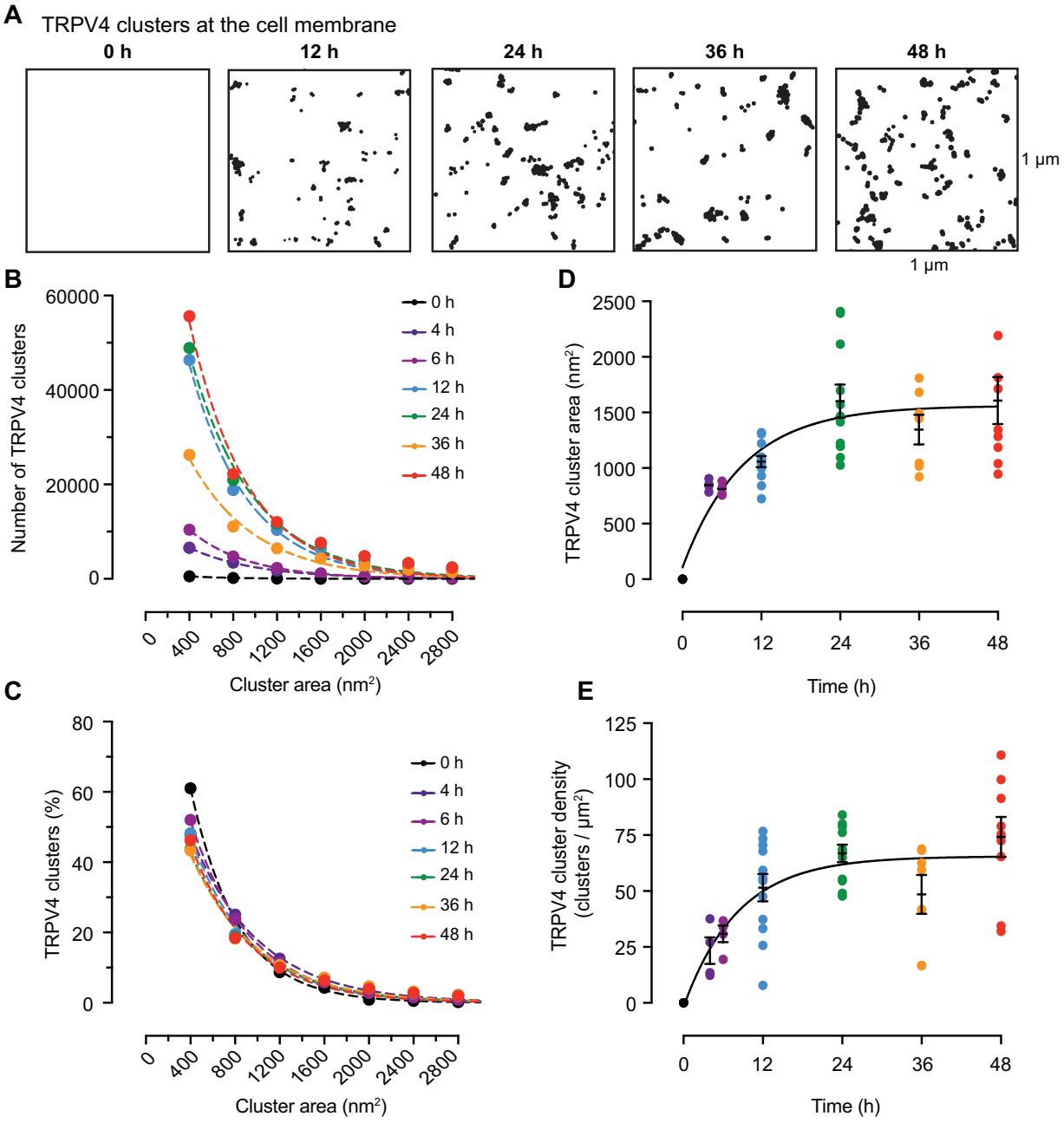

Figure 2.5 Time course of the formation of TRPV4 channel clusters in tsA-201 cells. (A) Representative superresolution GSD binary masks of immunolabeled TRPV4 channels in transfected tsA-201 cells at 0, 12, 24, 36, and 48 h after transfection. (B) Frequency distribution of TRPV4 channels cluster areas at each time point. (C) Relative frequency distribution of TRPV4 channels cluster areas expressed as percentages.

Dashed color lines in B and C represent the best single exponential decay function fit for each dataset. (D) Change of mean TRPV4 channel cluster area at different time points after transfection. Data are presented as mean ± SEM for individual cells at each time point. (E) Change of TRPV4 channel cluster density at different time points after transfection. Data are presented as mean ± SEM for individual cells at each time point. Mean cluster area data (D) and mean cluster density data (E) were fit with a one-phase exponential equation (solid black line). The tau values for cluster area and cluster density are 9.17 and 8.22 h, respectively. (B–E) All data were compiled as follows: 4 h: n = 13,734 from 4 cells; 6 h: 20,004 clusters from 4 cells; 12 h: n = 96,295 clusters from 12 cells; 24 h: n = 111,632 clusters from 11 cells; 36 h: n = 60,518 clusters from 7 cells, 48 h: n = 120,416 from 12 cells.

2.4.4 Turnover rate of Cav1.2 and TRPV4 channels in the membrane of tsA-201 cells

By tuning the three parameters in our model through iterative simulations, we found a connection between P_g and P_R to channel cluster size and between P_n channel cluster density.

Thus, properly constraining our model required information about channel turnover rates within cell membranes. To this end, we expressed photoactivatable-GFP tagged $Ca_V1.2$ or TRPV4 channels (PA-$Ca_V1.2$ and PA-TRPV4) in tsA-201 cells. Photoactivatable-GFP is non-fluorescent until it is exposed to a brief blue light pulse. Thus, PA-$Ca_V1.2$ and PA-TRPV4 fluorescence is limited to the set of channels expressed at the time of

photoactivation. PA-Ca_V1.2 and PA-TRPV4 fluorescence intensity is therefore proportional to the number of channels expressed and could be used to determine dwell time, i.e., the time these channels spend in the membrane.

For these experiments, cells expressing PA-Ca_V1.2 or PA-TRPV4 (**Figure 2.6**) were imaged before and after a 10 seconds exposure to 405 nm light to activate the PA-GFP. In **Figure 2.6A**, we show a confocal image from a center section of a representative tsA-201 cell expressing PA-Ca_V1.2. As expected, after photoactivation the fluorescence was largely limited to the surface membrane of the cell. For analysis, we measured the spatially-averaged fluorescence and generated pseudo line-scans from multiple regions in the membrane from 2D image stacks. The time course of fluorescence intensity in three sites in the membrane is shown to the right of the 2D image in **Figure 2.6A**. Note that at each site, over a period of 90 min after photoactivation, PA-Ca_V1.2 fluorescence nearly disappears, suggesting that most channels are removed from the membrane within this period. **Figure 2.6B** shows the averaged, normalized fluorescence intensity from all the membrane sites analyzed from multiple cells. The decaying phase of the curve was fit with a single exponential function with a $T_{1/2}$ of 9.74 minutes.

In **Figure 2.6C**, we show the results of equivalent experiments for cells expressing PA-TRPV4. As in the case of PA-Ca_V1.2, PA-TRPV4 fluorescence in the membrane increased following 405 illumination, and decayed with time. However, unlike PA-Ca_V1.2, PA-TRPV4 fluorescence seems to reach a steady state around 45% of the initial maximum signal. **Figure 2.6D** shows the averaged (with SEM), normalized

fluorescence and decay of all the analyzed sites. These data suggest that while a population of TRPV4 channels is removed from the membrane, a larger subset of channels either remains embedded within the membrane or is removed but then recycled back to it. A $T_{1/2}$ of 11.59 minutes for the first population was estimated by fitting a single exponential function.

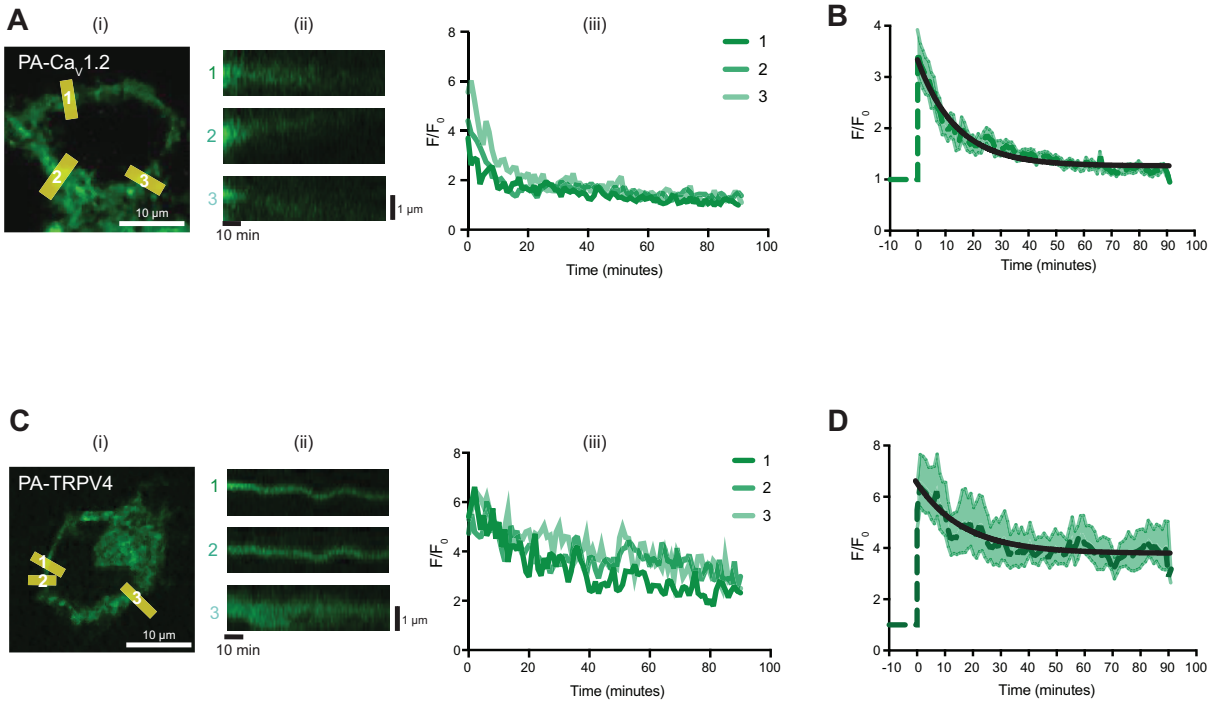

Figure 2.6 Dwell times for Ca$_V$1.2 and TRPV4 channels in tsA-201 cells are fast. (A) Representative image of a tsA-201 cell transfected with Ca$_V$1.2-PA-GFP immediately after stimulation (i), with corresponding labeled ROI slices (ii), and fluorescent traces of the ROI slices (iii). F, fluorescence. (B) Mean time course of Ca$_V$1.2-PA-GFP normalized fluorescence (dark green dashed line) and SEM at each time (light green shaded area) of all normalized ROIs. Time course was fit with an exponential function (black line). 26 ROIs from nine cells were averaged. (C) Representative image of a tsA-201 cell transfected with TRPV4-PA-GFP immediately after stimulation (i), with

corresponding labeled ROI slices (ii), and fluorescent traces of the ROI slices (iii). (D) Mean time course of TRVP4-PA-GFP normalized fluorescence (dark green dashed line) and SEM at each time (light green shaded area) of all normalized ROIs. Time course was fit with an exponential function (black line). 17 ROIs from 6 cells were averaged.

2.4.5 Model captures dwell times and time-dependent assembly of $Ca_V1.2$ and TRPV4 channel clusters

Our goal in acquiring the experimental measurements of the time course of channel cluster formation and channel turnover rate or dwell time described above was to extend our model beyond its successful representation of steady-state conditions (**Figure 2.3**). That is, could our model replicate the time-dependent assembly of $Ca_V1.2$ and TRPV4 channel clusters that we observed experimentally in tsA-201 cells (**Figure 2.4** and **2.5**) while incorporating the membrane dwell times that we measured (**Figure 2.6**).

Figure 2.7 shows the relationship between channel and cluster dwell times and model parameters, P_g and P_R. Channel and cluster dwell times are independent of model parameter, P_n, as dwell times correspond to events following nucleation. Note that decreasing P_R or decreasing P_g increases the membrane dwell times for both individual channels (**Figure 2.7A**) and channel clusters (**Figure 2.7B**). Further, these data suggest that the dwell times of a channel or a cluster in the membrane is determined by individual P_g values. For example, the predicted dwell times in the membrane of a

cluster in a cell with P_g = 0.07 and P_R = 0.0007 (P_g/P_R = 100) is 12 minutes, while a cell with P_g = 0.1 and P_R = 0.001 (P_g/P_R = 100) is 9 minutes.

We plotted the distributions of membrane dwell times for individual channels and channel clusters with a P_g of 0.01 and P_R of 0.0001 (**Figure 2.7C**) or 0.001 (**Figure 2.7D**). Regardless of the magnitude of P_g and P_R, our model generated exponential membrane dwell time distributions for individual channels that were exponential and Gaussian dwell time distributions for channel clusters. The mean dwell times in the membrane obtained from our model for both individual channels (60 min) and channel clusters (75 min) using a P_R of 0.0001 were similar to those suggested for $Ca_V1.2$ in neuronal dendrites (≈1 hour) (*258*).

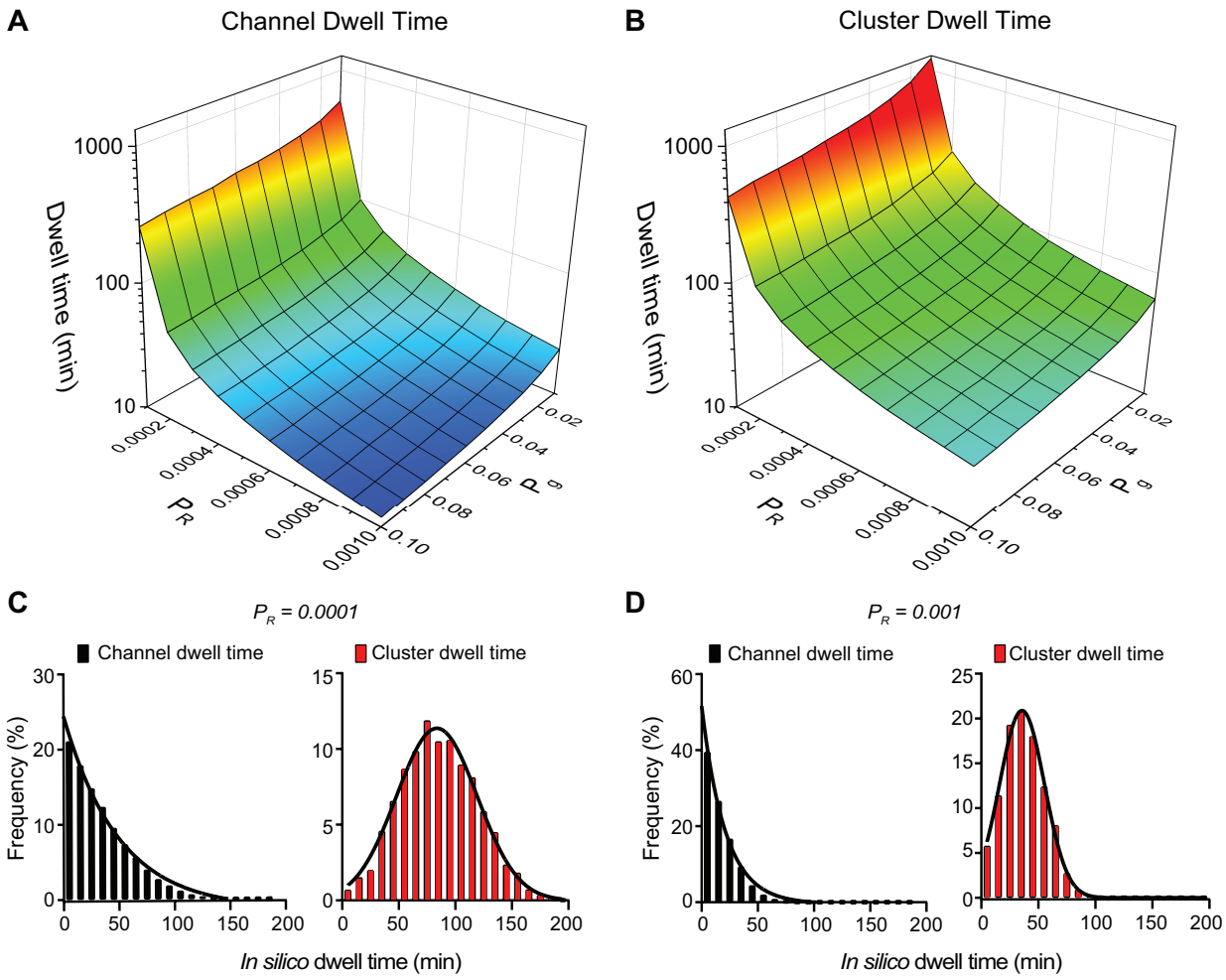

Figure 2.7 P_g and P_R determine channel and cluster dwell time. (A and B) Surface plots showing the relationships between P_g, P_R, and channel dwell time (A) or cluster dwell time (B). (C and D) Frequency distributions of channel and cluster dwell times with P_R equal to 0.0001 (C) or 0.001 (D). For the simulations in C and D, P_g and P_n were 0.01 and 0.00006, respectively.

Because the single channel and channel cluster membrane dwell times are predominantly set by the value of P_g in our model, we examined the effects of the paraments P_R and P_n on cluster area and densities after setting P_g to 0.07, the value that reproduced our experimental measurements of the area of $Ca_V1.2$ and TRPV4

channel clusters (**Figures 2.4** and **2.5**). As shown in **Figure 2.8A**, we found that setting the values of P_g and P_R in ratios ranging from 20-100 resulted in increasing channel cluster areas and that a P_g/P_R ratio > 50 was required to generate clusters with areas similar to those measured in our experiments for $Ca_V1.2$ and TRPV4 in tsA-201 cells 48 hours after transfection. This is important as it indicates that channel cluster sizes are determined by the P_g/P_R ratio and not by individual P_g and P_R values.

We also found that the influence of P_g/P_R ratios on channel cluster formation in our model is affected by P_n. For example, cluster area decreases as P_n is increased. This can be explained by the fact that when the P_n value is small, the probability of channel insertion decreases, and the channel clusters grow according to the specific values of P_g and P_R. However, when P_n is increased, the probability of channel insertion increases, resulting in the initiation of multiple clusters with large variations in size and a decrease in mean cluster area as shown in **Figure 2.8A.** In contrast, cluster density is independent of the P_g/P_R ratio and mainly determined by P_n (**Figure 2.8B**).

To further illustrate the effects of P_R and P_n on channel cluster area, we show the results of a series of simulations using two different P_n values (**Figure 2.8C**): 0.00045 (black trace) and 0.00005 (red trace). Similarly, the effects of P_R and P_n on channel cluster density are shown in **Figure 2.8D.** These two P_n values were chosen because they generated simulated channel cluster areas similar to those observed in tsA-201 cells expressing $Ca_V1.2$-EGFP (**Figure 2.4**) or TRPV4-EGFP (**Figure 2.5**) (i.e., P_n =

0.00045), or to those reported in studies in the endogenous channels native cells (i.e., P_n = 0.00005) (*240, 242, 243*).

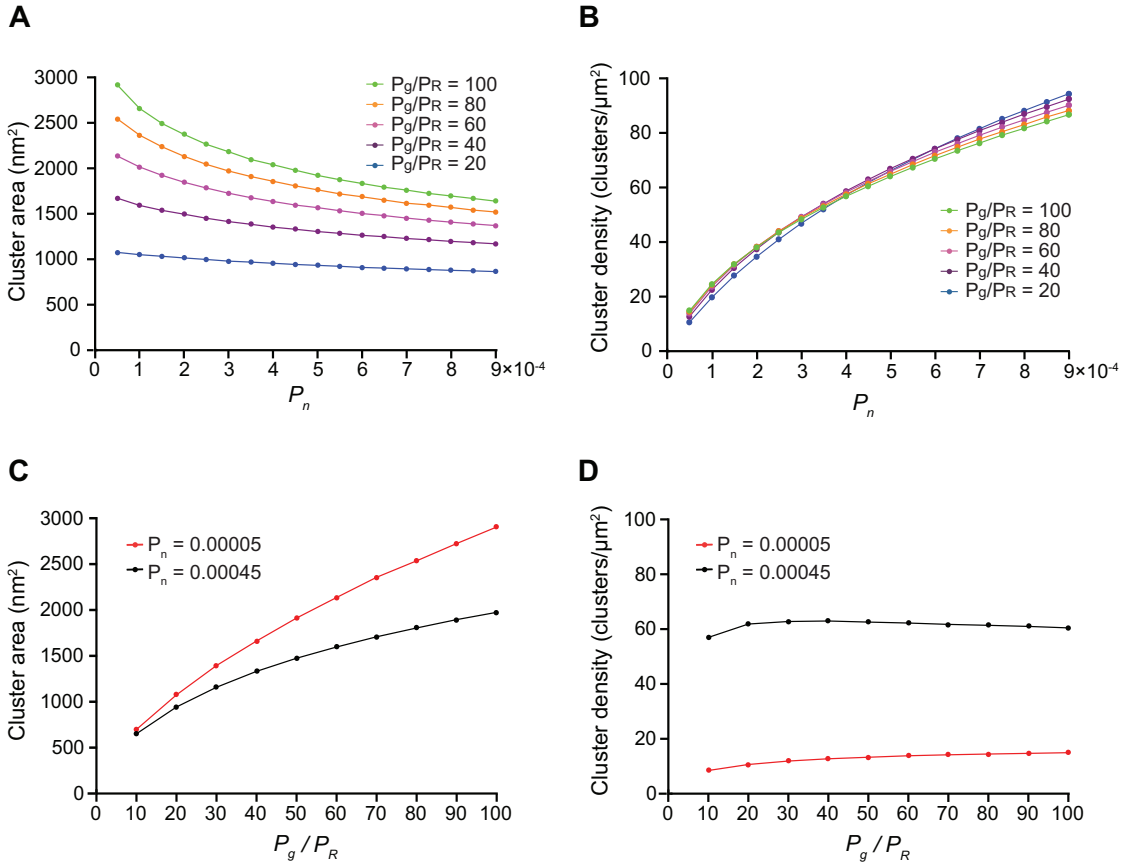

Figure 2.8 *In silico* stochastic self-assembly of protein clusters with realistic sizes and densities. (A) Plot of the relationships between P_n and cluster area at P_g/P_R ratios equal to 20 (P_g = 0.07, P_R = 0.0035), 40 (P_g = 0.07, P_R = 0.00175), 60 (P_g = 0.07, P_R = 0.001166667), 80 (P_g = 0.07, P_R = 0.000875), and 100 (P_g = 0.07, P_R = 0.0007). (B) Relationships between P_n and cluster density at P_g/P_R ratios equal to 20 (P_g = 0.07, P_R = 0.0035), 40 (P_g = 0.07, P_R = 0.00175), 60 (P_g = 0.07, P_R = 0.001166667), 80 (P_g = 0.07, P_R = 0.000875), and 100 (P_g = 0.07, P_R = 0.0007). For simulations in A and B, we averaged cluster area and density values at steady state for 2,000 iterations. (C) Effect of P_g/P_R ratios on cluster area. (D) Effect of P_g/P_R ratios on cluster density. (C and D)

For these simulations, we set the value of P_n = 0.00005 (red traces) and P_n = 0.00045 (black traces), P_g = 0.07 and P_R ranged between 0.007 and 0.0007 to achieve P_g/P_R ratios of 10–100.

2.4.6 In silico stochastic self-assembly of $Ca_V1.2$ and TRPV4 clusters

As our model successfully simulated the creation of channel clusters with size, densities, and dwell times similar to those observed experimentally, we set out to use this model to replicate the experimental data we acquired on the time courses of $Ca_V1.2$ and TRPV4 channel cluster formations expressed in tsA-201 cells (**Figures 2.4** and **2.5)**. To do so, images were generated on every iteration of the model using time-dependent probability functions P_g, P_n, and P_R. In **Figures 2.9A and 2.10A,** we defined the time-dependent probability functions of P_g, P_n, and P_R to be sigmoid functions. The rationale for this was our own data showing that the time course of $Ca_V1.2$ and TRPV4 cluster growth (P_g) and densities (P_n) followed a sigmoidal distribution and the work by Green, Barrett, Bultynck, Shamah and Dolmetsch (*255*) suggesting that $Ca_V1.2$ channel internalization in neurons (i.e., P_R) increased as $Ca_V1.2$ channel number increased. The range of P_n values used were determined by the density data in **Figures 2.4-2.5** as well as the P_n-density relationships in **Figure 2.8**.

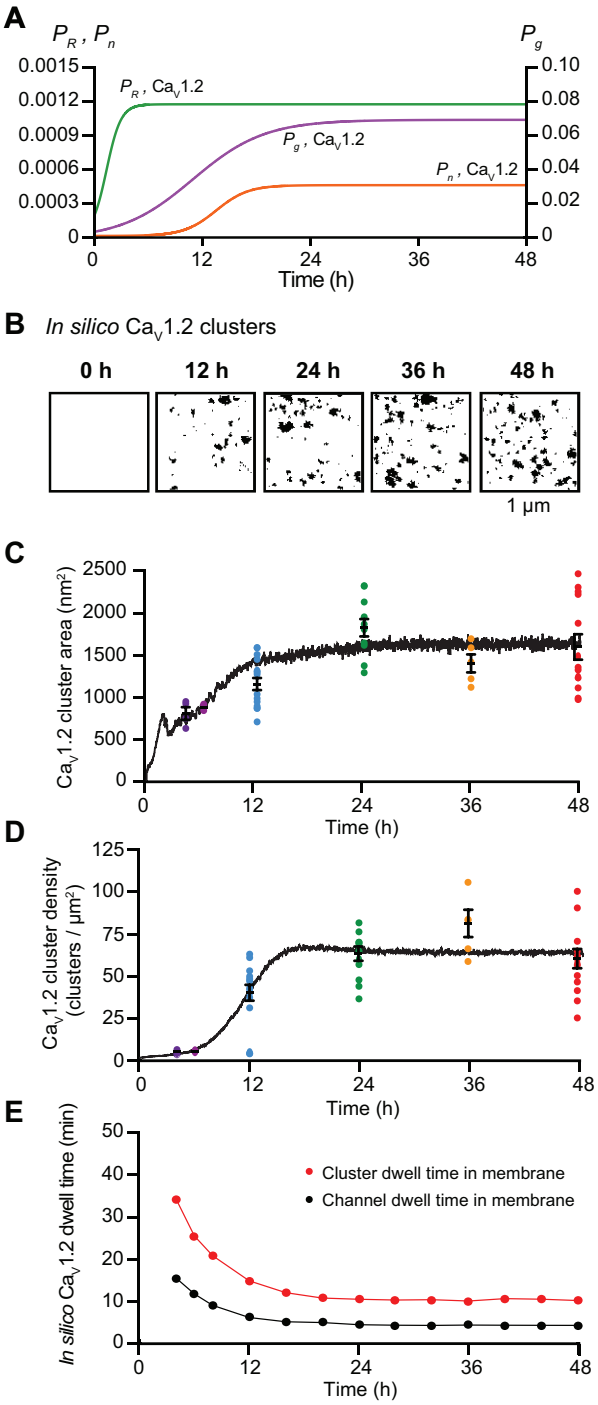

Figure 2.9 Sigmoidal time-dependent changes in P_g, P_n, and P_R reproduce the time course of $Ca_V1.2$ cluster formation in the plasma membrane of tsA-201 cells.

(A) Plots of $P_{g,Cav1.2}$ (purple), $P_{n,Cav1.2}$ (orange), and $P_{R,Cav1.2}$ (green) versus time. $P_{R,Cav1.2}$=1/1+5e-60t*0.001166667, $P_{g,Cav1.2}$=1/1+15e-12t*0.07, and

$P_{n,Cav1.2}$= 1/1+2000e-27t*0.00045. (B) *In silico* images of $Ca_V1.2$ clusters at 0, 12, 24, 36, and 48 h after the initiation of expression using the parameters in A. (C and D) The black trace depicts the time course of mean cluster area (C) and densities of simulated clusters (D). Colored dots represent the superimposed experimental data from Fig. 3. (E) Mean $Ca_V1.2$ channel (black) and cluster (red) dwell times based on the sigmoidal functions P_g, P_n, and P_R.

In the case of $Ca_V1.2$ channels, the time-dependent probability functions $P_{g,Cav1.2}$ and $P_{n,Cav1.2}$ reached steady-state in about 18 hours. Similarly, in the case of TRPV4 channels, $P_{g,TRPV4}$ and $P_{n,TRPV4}$ reached steady-state in about 20 hours. $P_{R,Cav1.2}$ and $P_{R,TRPV4}$ however, reached their steady-states in about 8 hours, which is critical as the ratio between P_R and P_g controls the cluster area. **Figures 2.9B** and **2.10B** show computer-generated 2D images of $Ca_V1.2$ and TRPV4 channel clusters at various iterations corresponding to 0, 12, 24, 36, and 48 hours after transfection.

In **Figures 2.9C-D** and **2.10C-D**, we plotted the results obtained from the model simulations (black trace) relative to our experimental data points for the sizes and densities of channel clusters. Cluster sizes for $Ca_V1.2$ and TRPV4 channels are similar, but there is a key difference in their densities. The cluster density for $Ca_V1.2$ channels is low relative to TRPV4 at 4 and 8 hours. This behavior is reproduced by the time-dependent probability function for P_n.

We could extract the membrane dwell times for individual channels and channels clusters of $Ca_V1.2$ (**Figure 2.9E**) and TRPV4 channels (**Figure 2.10E**) from these simulations. The dwell times in the membrane of individual $Ca_V1.2$ and TRPV4 channels (≈ 15 minutes) and channel clusters (≈ 35 minutes) were initially high, but decreased to lower steady-state levels after approximately 12 hours. At 48 hours, the predicted dwell times of both individual channels ($Ca_V1.2$ and TRPV4 : 4.2 minutes) and channel clusters ($Ca_V1.2$ and TRPV4: 10.3 minutes) were quite similar for the two channel types.

These data suggest that steady-state channel organization for either channel type can be attained by time-dependent changes in P_g and P_n and a relatively rapid turnover rate for both individual channels and clusters. Further, the data suggest feasible set points for P_g and P_n in living cells.

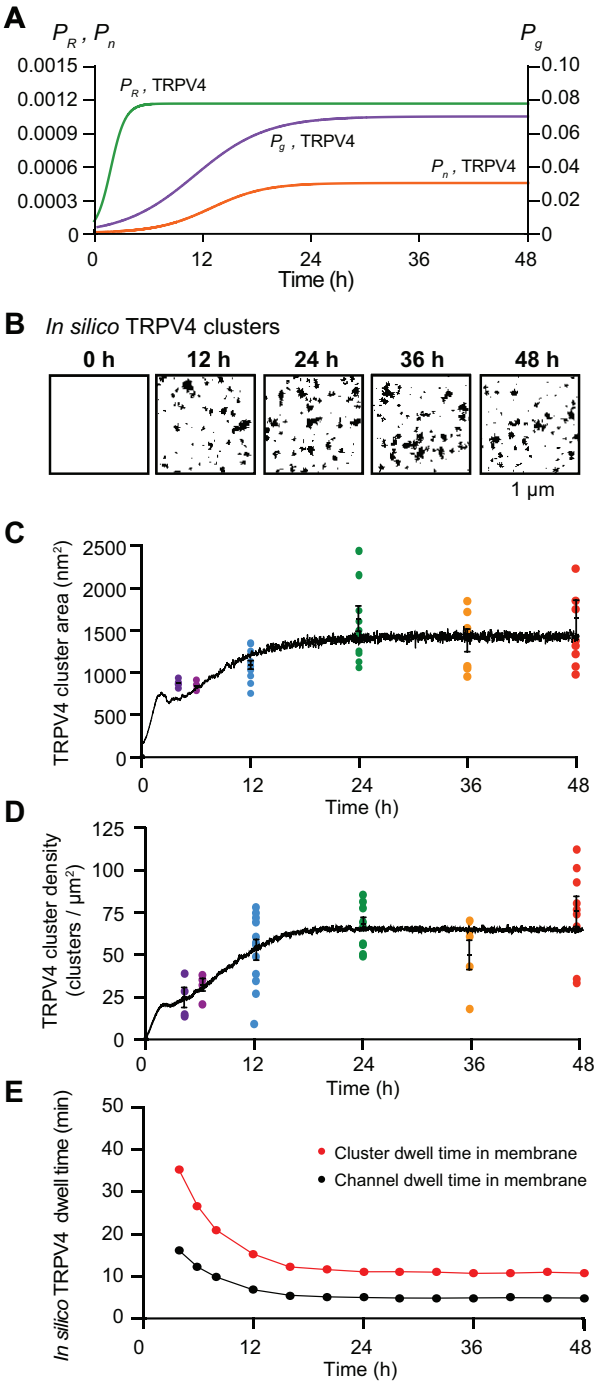

Figure 2.10 Sigmoidal time-dependent changes in P_g, P_n, and P_R reproduce the time course of TRPV4 cluster formation in the plasma membrane of tsA-201 cells.

(A) Plots of $P_{g,TRPV4}$ (purple), $P_{n,TRPV4}$ (orange), and $P_{R,TRPV4}$ (green) versus time. PR,TRPV4= 1/1+10e-60t*0.001166667, Pg,TRPV4= 1/1+15e-12t*0.07, and

Pn,TRPV4=1/1+75e-16t*0.00045. (B) In silico images of TRPV4 clusters at 0, 12, 24, 36, and 48 h after the initiation of expression using the parameters in A. (C and D) The black trace depicts the time course of mean cluster area (C) and densities of simulated clusters (D). Colored dots represent the superimposed experimental data from Fig. 4. (E) Mean TRPV4 channel (black) and cluster (red) dwell times based on the sigmoidal functions P_g, P_n, and P_R.

2.4.7 Feedback control of the stochastic self-assembly of $Ca_V1.2$ and TRPV4 clusters

As mentioned earlier, Green, Barrett, Bultynck, Shamah and Dolmetsch (*255*) suggested that $Ca_V1.2$ channel internalization increases as the number of channels increases, indicating some level of feedback between channel number and P_R, presumably as mediated through intracellular Ca^{2+} levels. Thus, we augmented our model to demonstrate how $Ca_V1.2$ and TRPV4 channel cluster size and density might be regulated by a feedback mechanism dependent on the number of channels present on the grid. To do so, we set the rates of cluster growth proportional to the number of channels present, represented by the first term (r_xN; $x = n, g,$ or R) in equations 1, 2, and 3 in the Methods. This term provides the positive feedback component of the model. The second term (P_x/K_x; $x = n, g,$ or R) in equations 1, 2, and 3 is responsible for the negative feedback component of the model. When the number of channels is small, the positive feedback process dominates. As the number of channels becomes larger, the negative feedback process dominates.

The impact of these additional terms in the model are shown in **Figure 2.11** for $Ca_V1.2$ and in **Figure 2.12** for TRPV4 channels. **Figures 2.11A** and **2.12A** show simulated images of $Ca_V1.2$ and TRPV4 channel clusters at 0, 12, 24, 36, and 48 hours after transfection. The positive and negative feedback processes create sigmoidal curves for P_g, P_R, and P_n (**Figures 2.11B** and **2.12B**). The time course of cluster growth is governed by the product of the P_g and P_R curves. Accordingly, depending on the shape of P_g and P_R curves, the cluster sizes may have two phases. Cluster density was mainly determined by a sigmoidal P_n curve.

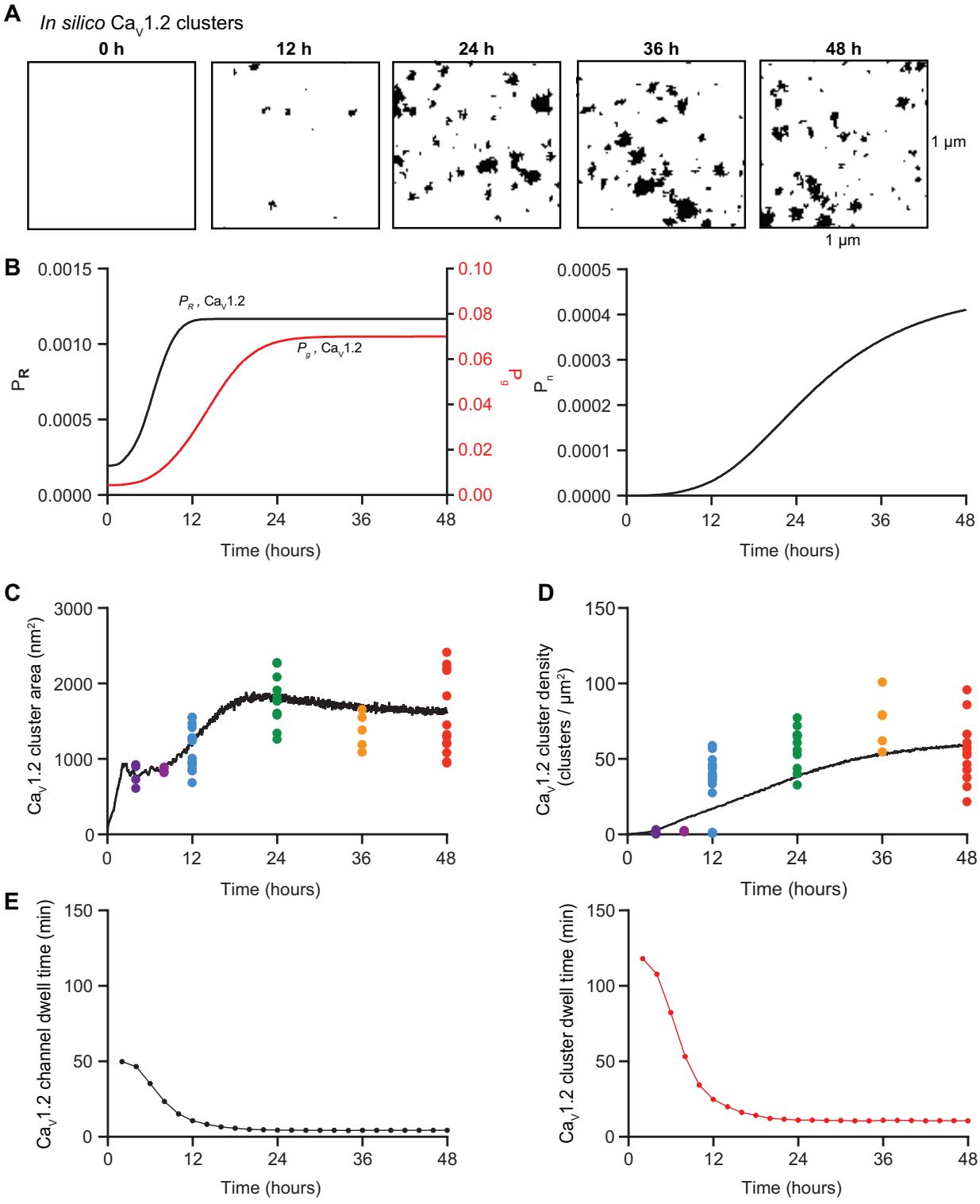

Figure 2.11 Feedback model for Cav1.2 cluster formation. (A) In silico images of $Ca_V1.2$ clusters at 0, 12, 24, 36, and 48 h after the initiation of expression. (B) Solutions

to the feedback model equations dPRdt, dPgdt, and dPndt. (C and D) The black trace depicts the time course of mean cluster area (C) and density (D) of simulated $Ca_V1.2$ clusters. Colored dots represent the superimposed experimental data from Fig. 3. (E) Predicted mean $Ca_V1.2$ channel (black) and cluster dwell times (red) based on the feedback model.

In **Figures 2.11C-D** and **2.12C-D**, we plotted the simulated and experimentally-measured and cluster sizes and densities for $Ca_V1.2$ and TRPV4 channels. The simulations show that increasing $P_{n,Cav1.2}$ (from 2e-07 to 0.00045), $P_{g,Cav1.2}$ (from 0.004 to 0.07), and $P_{R,Cav1.2}$ (from 0.0002 to 0.0012) (**Figure 2.11B**) or $P_{n,TRPV4}$ (from 0.000006 to 0.00045), $P_{g,TRPV4}$ (from 0.004 to 0.07), and $P_{R,TRPV4}$ (from 0.0001 to 0.0012) (**Figure 2.12B**) increases channel cluster areas and densities over time to levels similar to those observed experimentally. In the case of $Ca_V1.2$, $P_{g,Cav1.2}$, $P_{R,Cav1.2}$ and $P_{n,Cav1.2}$ reached plateau levels at about 24, 10, and 16 hours after transfection, respectively. In the case of TRPV4, $P_{g,TRPV4}$, $P_{R,TRPV4}$ and $P_{n,TRPV4}$ values plateaued about 24, 6, and 24 hours, respectively.

We also extracted the membrane dwell times of individual $Ca_V1.2$ (**Figure 2.11E**) and TRPV4 channels (**Figure 2.12E**) and clusters from simulations using the feedback model. With the parameters used in our simulations, the mean channel ($Ca_V1.2$ = 50 minutes; TRPV4 = 60 minutes) and channel cluster ($Ca_V1.2$ = 120 minutes; TRPV4 = 140 minutes) membrane dwell times were initially high. However, these values quickly (i.e., after about 4 hours) decreased and then remained relatively stable over time for

both channels types, such that at 48 hours the predicted channel and cluster dwell times for $Ca_V1.2$ were 4.3 and 10.5 minutes, respectively, and for TRPV4 were 4.3 and 10.9 minutes, respectively. To demonstrate how our feedback model works, we created videos of simulations of $Ca_V1.2$ and TRPV4 trafficking and cluster formation in the membrane using the P_g, P_R, and P_n values in **Figures 2.11** and **2.12**.

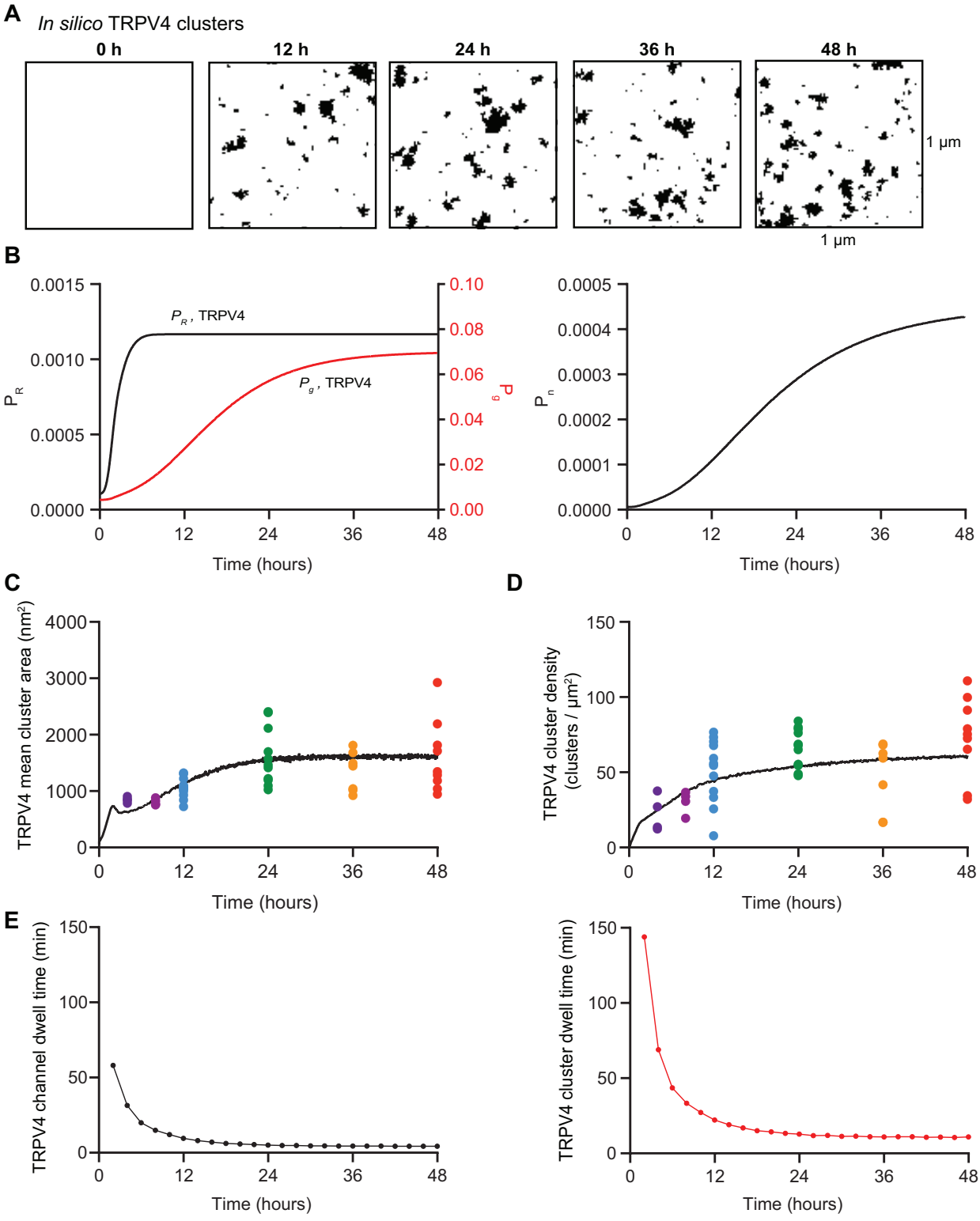

Figure 2.12 Feedback model for TRPV4 cluster formation. (A) In silico images of TRPV4 clusters at 0, 12, 24, 36, and 48 h after the initiation of expression. (B) Solutions

to the feedback model equations dPRdt, dPgdt, and dPndt. (C and D) The black trace depicts the time course of mean cluster area (C) and density of simulated TRPV4 clusters (D). Colored dots represent the superimposed experimental data from Fig. 4. (E) Predicted mean TRPV4 channel (black) and cluster dwell times (red) based on the feedback model.

The two methods we used to reproduce our experimental measurements of cluster formation for $Ca_V1.2$ (**Figure 2.4**) and TRPV4 (**Figure 2.5**) channels data are complementary and supportive of the concept that channel cluster size and density are regulated via feedback mechanisms. In the first method, we used empirically-derived assumptions regarding time-dependent changes in P_R, P_n, and P_g**.** This first model predicts that in order to reach a plateau phase in cluster size and density, we must increase the parameters P_n, P_g, and P_R until reaching a constant or equilibrium level. We proposed that the curves should be sigmoidally-shaped such that changes in cluster size and density would be constrained to the desired values of P_n, P_g, and P_R we observed in tsA cells. In the second method, the behavior of P_n, P_g, and P_R through time was modeled using differential equations coupled by the total number of channels, allowing us to explicitly include a feedback mechanism.

2.5 Discussion

Using a combination of experimental and computer modeling approaches, we have made five important observations regarding the formation of ion channel clusters and trafficking in living cells. First, the distributions of clusters of the five types of channels

studied ($Ca_V1.2$, BK, TRPV4, $Ca_V1.3_s$ and $Ca_V1.3_s$) were all described by a single exponential function regardless of the type of cell they are expressed in, supporting the hypothesis that the presence of ion channels clusters in cell membranes is consequent to a stochastic, self-assembly process. Second, $Ca_V1.2$ and TRPV4 channel clusters form in tsA-201 cells with an initial period of rapid growth in size, after which they are maintained in a steady-state. Third, this steady-state form in tsA-201 cells is maintained by a relatively fast turnover rate of $Ca_V1.2$ and TRPV4 channels. Fourth, our model predicts that steady-state size distributions of membrane channel clusters could be sustained by a range channel turnover rate. While we are aware of the possibility that our measurements are based solely on a heterologous expression system and might differ from those made in other cell types, our fifth observation is that both our experimentally-measured and predicted membrane dwell times are similar to those reported for $Ca_V1.2$ in cultured cardiac HL-1 cells (*259*) and in primary neurons (*258*), as well as to mean transcript and protein dwell times (*260*).

To illustrate how our model could be used by physiologists interested in investigating the role of a particular interacting protein in ion channel clustering, we have considered three potential scenarios in which a change in a physiological process alters ion channel cluster area or density via changes in one of the three model parameters (i.e., P_n, P_g or P_R). In the first scenario, let us propose that the insertion of channels at the plasma membrane is enhanced by the upregulation or activation of a signaling pathway. In our model, this process would result in an increase in the parameter P_n. An example of this could be the Ca^{2+}-dependent upregulation of K^+ channels expression via the activation

of the calcineurin/NFAT signaling pathway. As first demonstrated by Amberg, Rossow, Navedo and Santana (*261*) and Rossow et al (*262-264*), Kv4 and Kv2 channel expression is tightly regulated by intracellular Ca^{2+} in cardiac and vascular cells. BK channel expression is also regulated by Ca^{2+} levels in smooth muscle (*265, 266*). In this scenario, the increase in the expression of the channels will increase the available pool of channels that can be inserted at the plasma membrane, increasing cluster density. Interestingly, the differences in $Ca_V1.2$ and TRPV4 cluster densities reported here among tsA-201 cells, smooth muscle, and ventricular myocytes were simulated by variations in the P_n among these cells. These data suggest that the level of expression of these channels and/or the proteins related with the trafficking and delivery of these channels to the plasma membrane vary between cells.

In the second scenario, we consider the possibility that the insertion of new channels is favored to occur in the same sites where other channels have been previously inserted because of the upregulation of an interacting protein. In our model, this process would increase P_g. An example of such a protein is BIN1, which binds to the inner face of the plasma membrane and forms lattices via the cooperative binding of other molecules, thus creating membrane microfolds (*267*). In ventricular myocytes, BIN1 has been implicated in the formation of membrane curvatures (*268*) and in anchoring microtubules where newly synthesized $Ca_V1.2$ channels are delivered to the surface membrane (*269, 270*). As such, BIN1 could function to increase the local concentration of $Ca_V1.2$ channels at specific sites in the plasma membrane, enhancing their clustering. Consistent with this, De La Mata, Tajada, O'Dwyer, Matsumoto, Dixon,

Hariharan, Moreno and Santana (*271*) found that overexpression BIN1 in human embryonic stem cell-derived cardiomyocytes increased $Ca_V1.2$ cluster size. Thus, BIN1 could be acting to direct the directed insertion of $Ca_V1.2$ channels in the sarcolemma of cardiac myocytes which would increase the P_g of these channels. Importantly, in the case of channels that undergo functional coupling (i.e. L-type Ca^{2+} channels), the increase in cluster size could strengthen the coupling between these channels resulting in a further increase in the amplitude of ion flux.

Finally, in the third scenario, we imagine a situation in which the removal of individual ion channels or ion channel clusters from the plasma membrane is enhanced by an interacting protein. In our model, this process would result in an increase in the parameter P_R. An example of this could be the activation of the HECT ubiquitin ligase ALP4, which has been linked to TRPV4 channel internalization (*272*). Another example is the tumor suppressor eIF3e/Int6 (eukaryotic initiation factor 3 subunit e), which induces internalization of $Ca_V1.2$ channels in neurons (*255*). In this scenario, the activation of these proteins will likely be associated with an overall decrease in channel membrane dwell time and a decrease in clusters size.

An important observation we made in the course of this study is that whereas the sizes and densities of $Ca_V1.2$ and TRPV4 channel clusters expressed in tsA-201 cells increased rapidly after transfection, both parameters reach a plateau within 24 hours. These results suggest that plasma membrane expression levels and clustering of exogenously expressed $Ca_V1.2$ and TRPV4 channels is under the control of a feedback

mechanism. Indeed, recent live-cell imaging experiments indicate that $Ca_V1.2$ containing vesicles in tsA-201 cells could have multiple mechanisms for interacting and delivering channel to the plasma membrane (*229*). Similar proposals have been put forth for endogenous $Ca_V1.2$ in cardiac myocytes (*273*) and neurons (*255*). The latter report suggested that action potential firing rate, channel activity, and a Ca^{2+}-driven increase in $Ca_V1.2$ internalization (i.e., P_R) was responsible for regulating plasma membrane expression levels of $Ca_V1.2$. Our feedback model relies exclusively on channel number and does not take into account the state of the channel (e.g., open, deactivated, inactivated, desensitized). Thus, a desensitized or inactivated channel would have the same probability of being removed by internalization or endocytosis than a deactivated or open channel. Mechanisms determining steady-state levels of these ion channels in cardiac and smooth muscle will need further study.

Another intriguing question posed by our work is whether the membrane dwell times and time course of clustering of $Ca_V1.2$ and TRPV4 channels in native cells are similar to those we found operating in tsA-201 cells. The work by De La Mata, Tajada, O'Dwyer, Matsumoto, Dixon, Hariharan, Moreno and Santana (*271*) suggests that in hESC-CMs, $Ca_V1.2$ cluster sizes and densities increased from the induction of differentiation until day 30. Interestingly, the channel cluster sizes and densities achieved at this time point were similar to those in adult ventricular myocytes, raising the possibility that they had reached an intrinsically-defined level of steady-state expression and clustering. Regardless of whether a steady state had been reached or not, these hESC-CM data suggests that the rates of cluster nucleation, growth, removal,

and thus channel membrane dwell times are likely different among cells at different levels of differentiation. A testable hypothesis is that the membrane dwell time of channels is higher in rapidly dividing cells like tsA-201 cells, than in fully differentiated, non-dividing cells like ventricular myocytes, and that upon stimulation (e.g., autonomic nervous system, physiological and pathological hypertrophy) changes in gene expression, channel delivery, recycling and/or protein degradation could increase channel dynamics.

Another key question raised by our study is whether membrane channels are internalized individually or through the removal of entire clusters. Our experimental data and model simulations do not provide a definitive answer, but simulations in which channels were exclusively removed one at a time predicted the formation of a large number of macro-clusters with parameters similar to those used to reproduce experimental data from cardiac myocytes, smooth muscle cells, neurons, and tsA-201 cells. Yet, macro-clusters predicted by the model were not observed experimentally. Accordingly, we modified the model so that channel internalization would be stochastic and involve individual channels as well as channel clusters of varied sizes. Considering that the area of an endocytic vesicle could range from 1200 to 1.26 $x10^5$ nm^2 and the mean cluster areas reported here range from about 1900 to 3700 nm^2 this assumption seems reasonable. Future experiments will be required to test this hypothesis.

Finally, while our data reveal that in smooth muscle and tsA-201 cells, channels are clustered randomly throughout the entire cell surface, it is important to mention that

variations in channel expression both between and within cells are commonly observed and reported. To cite just a few examples, Na_V1 channels are highly concentrated in the nodes of Ranvier of myelinated axons, but largely absent from the internodal membrane (*274*), $Ca_V1.2$ channel are preferentially expressed in along the T-tubules of ventricular myocytes (*240*), the Na^+/H^+ exchanger is absent from the T-tubules (*275*), and the Na^+/K^+α2ATPase proteins are distributed preferentially in the T-tubules and surface sarcolemma (*276*). While these regional variations in channel expression may seem incompatible with our model, they could still be the result of a stochastic, self-assembly process operating within a restricted cellular domain. For example, our data suggest that $Ca_V1.2$ channel clusters are stochastically self-assembled along the T-tubules of ventricular myocytes, but not throughout the entire cell. These seemingly contradictory observations can be reconciled by proposing that there may be variations in P_n, P_g, or P_R in different compartments of the same cell that lead to stochastic self-assembly of clusters therein. The possibility of regional variations in P_n, P_g, and P_r should be addressed in further studies.

In summary, we have provided a set of experimental measurements and computer simulations that support the hypothesis that the formation of ion channel clusters in the surface membrane of excitable cells reflects the operation of a stochastic self-assembly process without the involvement of any active mechanism of aggregation, such as agrin-induced recruitment of acetylcholine receptors into the post-synaptic motor endplate (*277*), ankyrin G-mediated clustering of voltage-gated Na^+ channels and Kv7 channels et nodes of Ranvier (*278*), and Kv2 channel clustering by VAPA and VAPB

proteins (*279, 280*). Indeed, our data are consistent with the view that membrane channel clustering is the default organization for multiple types of channels in the surface membranes of four different cell types. Notably, our model incorporates a self-regulating mechanism that assumes a feedback process between channel number and channel cluster formation. Our model may be broadly applicable to the distributions of many different types of membrane (bound proteins and channels) in health and disease states. We certainly cannot rule out the possibility that one or more proteins will be found that are not randomly distributed along the surface membrane. Whether or not there is a functional consequence of clustering for all the types of ion channels, as we have found for $Ca_V1.2$, $Ca_V1.3$, BK, and TRPV4 channels, remains an open question, but a very important one.

Table 2.1 Feedback model parameters and initial conditions.

	K_n	K_g	K_R	r_n	r_g	r_R	Initial P_n	Initial P_g	Initial P_R
$Ca_V1.2$	0.00045	0.07	0.001166667	0.000002	0.0018	0.0003	0.000000225	0.004375	0.00019444
TRPV4	0.0004	0.07	0.001166667	0.000002	0.0005	0.0003	0.000005921	0.004375	0.00010606

Table 2.2 Summary of experimental super-resolution data.

Ion channel	Cluster area (nm^2)	Cluster density (clusters/μm^2)
Smooth muscle		
$Ca_V1.2$	2488 ± 140	9.7 ± 0.4
TRPV4	1834 ± 117	7.8 ± 0.2
BK	3008 ± 223	9.2 ± 0.5
Cardiac muscle		
$Ca_V1.2$	2555 ± 82	21.9 ± 1.5
Hippocampal neurons		
$Ca_V1.3$	3660 ± 80	23.3 ± 1.8
*tsA-201 cells**		
$Ca_V1.2$	1566 ± 148	54.6 ± 5.7
$Ca_V1.3_S$	2119 ± 73	15.8 ± 4.3
$Ca_V1.3_L$	2543 ± 50	14.9 ± 4.3
TRPV4	1605 ± 212	73.4 ± 8.9

Table 2.3 Summary of *in silico* steady-state data.

Ion channel	Cluster area (nm^2)		Cluster density (clusters/μm^2)		*Steady state P_g, P_R, P_n*	
	Short dwell time	Long dwell time	Short dwell time	Long dwell time	Short dwell time	Long dwell time
Smooth muscle						
$Ca_V1.2$	2481	2479	9.7	9.7	P_g = 0.1 P_R = 0.0012803 P_n = 0.000043648	P_g = 0.01 P_R = 0.0001609 P_n = 0.00000519639
TRPV4	1819	1851	7.8	7.8	P_g = 0.1 P_R = 0.0020398 P_n = 0.000039526	P_g = 0.01 P_R = 0.00027071 P_n =0.000004824
BK	2981	3030	9.2	9.24	P_g = 0.1 P_R = 0.00097263 P_n = 0.000036651	P_g = 0.01 P_R = 0.000119 P_n = 0.000004355
Cardiac muscle						
$Ca_V1.2$	2559	2543	21.9	21.8	P_g = 0.1 P_R = 0.0010796 P_n = 0.00011952	P_g = 0.01 P_R = 0.00013367 P_n = 0.000014258
Hippocampal neurons						
$Ca_V1.3$	3657	3697	23.2	23.4	P_g = 0.1 P_R = 0.00052117 P_n = 0.0001249	P_g = 0.01 P_R = 0.000062953999 P_n = 0.000014666
tsA-201 cells						
$Ca_V1.3_S$	2103	2127	17.1	15.8	P_g = 0.05 P_R = 0.00086217 P_n = 0.000044351	P_g = 0.005 P_R = 0.00010066 P_n = 0.000004763112
$Ca_V1.3_L$	2539	2558	14.8	15.0	P_g = 0.05 P_R = 0.00058827 P_n = 0.000036252	P_g = 0.005 P_R = 0.0000787855 P_n = 0.0000042249

Chapter 3: The formation of $K_V2.1$ macro-clusters is required for sex-specific differences in $Ca_V1.2$ clustering and function in arterial myocytes

3.1 Abstract

In arterial myocytes, the canonical function of voltage-gated $Ca_V1.2$ and $K_V2.1$ channels is to induce myocyte contraction and relaxation through their responses to membrane depolarization, respectively. Paradoxically, $K_V2.1$ also plays a sex-specific role by promoting the clustering and activity of $Ca_V1.2$ channels. However, the impact of $K_V2.1$ protein organization on $Ca_V1.2$ function remains poorly understood. We discovered that $K_V2.1$ forms micro-clusters, which can transform into large macro-clusters when a critical clustering site (S590) in the channel is phosphorylated in arterial myocytes. Notably, female myocytes exhibit greater phosphorylation of S590 and macro-cluster formation compared to males. Contrary to current models, the activity of $K_V2.1$ channels seems unrelated to expression density in arterial myocytes. Disrupting the $K_V2.1$ clustering site ($K_V2.1_{S590A}$) eliminated $K_V2.1$ macro-clustering and sex-specific differences in $Ca_V1.2$ cluster size and activity. We propose that the degree of $K_V2.1$ clustering tunes $Ca_V1.2$ channel function in a sex-specific manner in arterial myocytes.

3.2 Introduction

Activation of dihydropyridine-sensitive, voltage-gated L-type $Ca_V1.2$ channels plays a crucial role in the development of myogenic tone (*281*), a process of autoregulation that enables arteries to regulate their diameter in response to changes in intravascular

pressure (*282*). This mechanism, independent of neural or hormonal influences, is critical to maintain constant blood flow despite changes in blood pressure.

The current model of the myogenic response proposes that mechanical stretch of the membrane leads to the activation of TRPC6 (*90*), TRPM4 (*283*), and TRPP1/2 (PKD2) (*91*) channels, which depolarizes arterial myocytes, activating $Ca_V1.2$ channels (*281*). Activation of a single or a small cluster of $Ca_V1.2$ channels results in a local increase in intracellular Ca^{2+} concentration ($[Ca^{2+}]_i$) termed a "$Ca_V1.2$ sparklet" (*92, 93, 284*). Summation of multiple $Ca_V1.2$ sparklets leads to a global increase in $[Ca^{2+}]_i$ that triggers muscle contraction.

$Ca_V1.2$ channels form clusters in the plasma membrane via a stochastically self-assembly mechanism (*285*). $Ca_V1.2$ channels within these clusters can gate cooperatively in response to Ca^{2+}-driven physical interactions of adjacent channels (*143, 240*). $Ca_V1.2$ channels in this configuration allow for larger Ca^{2+} influx compared to random, independent openings of individual channels. In vascular smooth muscle, cooperative gating of $Ca_V1.2$ channels has been estimated to contribute up to ~50% of Ca^{2+} influx during the development of myogenic tone (*94*).

One route of negative feedback regulation of membrane depolarization and Ca^{2+} influx via $Ca_V1.2$ channels occurs through the depolarization-mediated activation of delayed rectifier voltage-gated $K_V2.1$ channels (*105, 286*). In its canonical role, $K_V2.1$ proteins in arterial smooth muscle cells form ion conducting voltage-gated K^+ channels whose

activation results in membrane potential hyperpolarization in these cells, thereby affecting myocyte $[Ca^{2+}]_i$ and myogenic tone (*105*). Until recently, the accepted role of $K_V2.1$ protein in arterial myocytes was to form K^+ conducting channels. However, our recent work suggests that that only about 1% of the $K_V2.1$ channels in the plasma membrane of arterial smooth muscle are conductive (*287*). Indeed, a growing body of evidence suggests that $K_V2.1$ proteins have dual conductive and structural roles in the surface membrane of smooth muscle cells and neurons (*287-289*).

In neurons and HEK293T cells, $K_V2.1$ is expressed in large macro-clusters (*161, 170, 279, 288, 290-292*). A 26 amino acid region within the C-terminus of the channel called the proximal restriction and clustering (PRC) domain was determined to be responsible for this expression pattern (*164*). The high-density clustering of $K_V2.1$ channels is influenced by phosphorylation of serine residues within the PRC domain (*293-295*). Additionally, in heterologous expression systems, the majority of $K_V2.1$ channels within macro-clusters are considered non-conductive (*168, 170, 290*). Little to no channel activity was detectable within $K_V2.1$ clusters, whereas currents could be recorded in areas with diffuse $K_V2.1$ expression (*170*). One of the structural roles of $K_V2.1$ is to promote clustering of $Ca_V1.2$ channels, thus increasing the probability of $Ca_V1.2$-to-$Ca_V1.2$ interactions within these clusters (*288, 289*).

Both, the conductive and structural roles of $K_V2.1$, depend on the level of expression of this protein, which in arterial myocytes varies with sex (*287*). In female myocytes, where expression of $K_V2.1$ protein is higher than in male myocytes, $K_V2.1$ has both conductive

and structural roles. Female myocytes have larger $Ca_V1.2$ clusters, $[Ca^{2+}]_i$, and myogenic tone than male myocytes. In contrast, in male myocytes, $K_V2.1$ channels regulate membrane potential, but not $Ca_V1.2$ channel clustering.

Based on these data, a model was proposed in which $K_V2.1$ function varies with sex(*287*). In males, $K_V2.1$ channels primarily control membrane potential, but in female myocytes $K_V2.1$ plays dual electrical and $Ca_V1.2$ clustering roles. Currently, it is unclear whether the conductive and structural functions of $K_V2.1$ in native arterial myocytes rely on its clustering ability, and if this relationship is sex-dependent.

In this study, we tested the hypothesis that conductive and structural roles of $K_V2.1$ channels in male and female arterial myocytes depend on their capacity to form clusters in studies of WT and S586A mutant rat $K_V2.1$ channels expressed in heterologous cells, and in arterial myocytes from a novel gene edited knock-in mouse expressing the S590A mutation. We focused on serine 586 within the PRC domain (amino acids 573-598) of rat $K_V2.1$ because a point mutation changing this amino acid to a non-phosphorylatable alanine decreases the $K_V2.1$ clustering phenotype (*164*). This corresponds to a S590A point mutation in the mouse $K_V2.1$ channel. Our data show that $K_V2.1$ is expressed into large macro-clusters composed of micro-clusters that can only be resolved with super-resolution microscopy. The $K_V2.1_{S586A}$ point mutation nearly eliminated $K_V2.1$ macro-clusters but had a minimal impact on micro-clusters. Notably, we find that $K_V2.1$ channel function is not dependent on its ability to form macro-clusters in arterial myocytes of either sex. Rather, $K_V2.1$ macro-clustering enhances $Ca_V1.2$

channel clusters and activity. Based on these results, we propose a new model in which macro-clustering of $K_V2.1$ in arterial myocytes alters $Ca_V1.2$ channel organization and function in a sex-specific manner but has no impact on its conductive function.

3.3 Materials and Methods

3.3.1 Generation of the CRISPR/Cas9-edited $K_V2.1_{S590A}$ (KCNB1 S590A) knock-in mouse

The KCNB1 S590A mutation changes a AGC codon to GCC in Exon 2, thus converting a serine to an alanine (S590A) in the $K_V2.1$ polypeptide. The knock-in mouse was generated in collaboration with the UC Davis Mouse Biology Program by using Crispr/CAS mediated homology directed repair. KCNB1 S590A mice were generated by introducing a mixture of gRNA (15 ng/L), single-stranded oligodeoxynucleotide (ssODN) repair template and Cas9 protein (30 ng/μL) by pronuclear microinjection into C57BL/6J mouse zygotes. Twenty zygotes were injected and implanted into the oviducts of one surrogate dam. A total of 6 pups were born, and genomic DNA was extracted from tail biopsies followed by PCR amplification using a specific primer set to identify a single male founder (F0). DNA-Seq analysis was used to confirm the mouse genotype. The correctly integrated single mutant F0 male mouse was further backcrossed with WT C57BL/6J female mice to produce offspring (F1) followed by intercrossing for two additional generations to obtain KCNB1 S590A heterozygotes which were used for breeding. Heterozygous and homozygous mutants were identified by a PCR genotyping protocol.

3.3.2 Animals

Mice were euthanized with a single, lethal dose of sodium pentobarbital (250 mg/kg) intraperitoneally. All experiments were conducted in accordance with the University of California Institutional Animal Care and Use Committee guidelines.

3.3.3 Arterial myocyte isolation

Third and fourth order mesenteric arteries were carefully cleaned of surrounding adipose and connective tissue, dissected out, and placed in ice-cold dissecting solution (Mg^{2+}-PSS; 5 mM KCl, 140 mM NaCl, 2mM $MgCl_2$, 10 mM glucose, and 10 mM HEPES) adjusted to pH 7.4 with NaOH. Arteries were first placed in dissecting solution supplemented with 1.23 mg/ml papain (Worthington Biochemical, Lakewood, NJ) and 1 mg/ml DTT at 37˚C for 14 min. This was immediately followed by a five-min incubation in dissecting solution supplemented with 1.6 mg/ml collagenase H, 0.5 mg/ml elastase (Worthington Biochemical), and 1 mg/ml trypsin inhibitor from *Glycine max* at 37˚C. Arteries were rinsed three times with dissection solution and single cells obtained by gentle trituration with a wide-bore glass pipette. Myocytes were maintained at 4˚C until used.

3.3.4 HEK293T cell culture and transfection

HEK293T (AATC #CRL-3216) cells were cultured in Dulbecco's Modified Eagle Medium (Gibco #11955) supplemented with 10% fetal bovine serum (Gibco #26140) and 1% penicillin/streptomycin (Gibco #15140122) and maintained at 37°C in a humidified 5% CO_2 atmosphere. Cells were transiently transfected using JetPEI (Polyplus Transfection

#101000053) according to manufacturer's protocol and passaged 24 hours later onto 25 mm square #1.5 coverslips or 18 mm square collagen coated #1.5 coverslips (Neuvitro Corporation #GG-18-15-Collagen) for GSD experiments. Plasmids encoding DsRed-Kv2.1$_{WT}$, DsRed-Kv2.1$_{S586A}$, DsRed-Kv2.1$_{P404W}$, and DsRed-Kv2.1$_{P404W,\ S586A}$ were previously described(*279, 289*). mScarlet-tagged versions of these plasmids were generated by GenScript, replacing the sequence encoding dsRed with sequence encoding mScarlet(*296*). For the bimolecular fluorescence experiments, cells were transfected with the pore-forming subunit of the rabbit $Ca_V1.2$ (α1c, kindly provided by Dr. Diane Lipscombe; Brown University, Providence, RI) with the carboxy tail fused to either the N-fragment (VN) or the C-fragment (VC) of the Venus protein (27097, 22011; Addgene, Cambridge, MA), auxiliary subunits $Ca_V\alpha_2\delta$, $Ca_V\beta_3$ (kindly provided by Dr. Diane Lipscombe, Brown University, Providence, RI) and either DsRed-$K_V2.1_{P404W}$ or DsRed-$K_V2.1_{P404W,\ S586A}$-dsRed. HEK293T cells were transfected with $Ca_V1.2$-VN, $Ca_V1.2$-VC, $Ca_V\alpha_2\delta$, $Ca_V\beta_3$ and DsRed-$K_V2.1$-dsRed in a 1.0:1.0:1.0:1.5:0.4 ratio.

3.3.5 Live cell confocal imaging

HEK293T cells transfected with 200 ng of mScarlet-Kv2.1$_{WT}$ or mScarlet-Kv2.1$_{S586A}$ and seeded onto 25-mm square 1.5 coverslips approximately 16 hours before experiments. Imaging was performed in Tyrode III solution consisting of (in mM) 140 NaCl, 5.4 KCl, 1 $MgCl_2$, 1.8 $CaCl_2$, 5 HEPES, and 5.5 glucose, pH 7.4 with NaOH. Cells were imaged with an Olympus Fluoview 3000 confocal laser-scanning microscope equipped with an Olympus Plan-Apochromat 60x oil immersion lens (NA = 1.40). Image stacks were analyzed using Imaris software.

Stacks of images were analyzed using Imaris 10 (Andor, Belfast). Briefly, K_V2.1-associated mScarlet signal was mapped to x/y/z centroid co-ordinates in each image stack using the Spots tool. Spots were assigned to all signal surpassing a fixed signal threshold and restricted to puncta greater than 100 nm (x/y) and 150 nm diameter (z), such that any bright signal with a volume greater than two voxels was identified as a K_V2.1 cluster. 'Region Growing' was utilized (with a fixed manual threshold) to apply variable sizing to K_V2.1 Spots, in line with the volume and brightness of mScarlet puncta. Finally, the Cell segmentation function was used to estimate cell boundaries based on low-intensity mScarlet signal and obtain an approximate cell volume.

3.3.6 K_V2.1 immunofluorescence immunocytochemistry

Immunofluorescence labeling was performed on freshly dissociated arterial myocytes. Cells were left to adhere for one hour at room temperature prior to fixation, fixed with 4% formaldehyde (Electron Microscopy Sciences #50980487) diluted in phosphate-buffered saline (PBS) (Fisher Scientific, Hampton, NH) for 15 minutes at room temperature, washed, and incubated with 50 mM glycine (BioRad, Hercules, CA) for 10 min to reduce aldehydes. The surface membrane was stained with wheat germ agglutinin (WGA) Alexa Fluor 488 (1 µM, ThermoFisher #W11261) for 10 minutes at room temperature followed by washing. Cells were then incubated in blocking buffer made of 3% w/v bovine serum albumin and 0.25% Triton X-100 in PBS, followed by incubation with mouse anti-Kv2.1 (mAb K89/34; RRID: AB_2877280; NeuroMab, Davis, CA, 1:200) diluted in blocking buffer for one hour at room temperature. Myocytes were

washed, incubated at room temperature for one hour with Alexa Fluor 647-conjugated donkey anti-mouse IgG diluted in blocking buffer (2 µg/ml, Molecular Probes, Cat #A31571) followed by washes in PBS. For experiments investigating K_V2.1 phosphorylation state, double labeling was performed with the mouse anti-K_V2.1 pS590 phosphospecific mAb L100/1(*297*) together with rabbit anti-Kv2.1 (KC(*292*); Trimmer laboratory, RRID:AB_2315767; 1:100). Myocytes were washed, incubated at room temperature for one hour with Alexa Fluor 568-conjugated goat anti-mouse IgG (2 µg/ml, Molecular Probes, Cat #A11004) and Alexa Fluor 647-conjugated donkey anti-rabbit IgG (2 µg/ml, Molecular Probes, Cat #A31571) diluted in blocking buffer followed by washes in PBS. All washes were performed with PBS three times for 10 minutes. Coverslips were mounted onto microscope slides in Vectashield mounting medium (Vector Labs) and sealed with clear nail polish. Images were collected on a Dragonfly 200 spinning disk confocal (Andor), coupled to a DMi* Leica microscope (Leica, Wetzlar, Germany) equipped with a 60x oil immersion objective (NA = 1.40) and acquired using an Andor iXon EMCCD camera. Images were collected via Fusion software, in optical planes with a z-axis of 0.13 µm/step. Image files were analyzed using Imaris.

Image stacks were segmented and analyzed in Imaris 10. WGA-488 signal was background-subtracted and a fixed threshold applied to consistently map the plasma membrane, using the Surfaces tool. Alexa Fluor-647 signal (denoting K_V2.1 puncta) was assessed using the Spots tool, as described above. Spots marking K_V2.1 clusters were

categorized into internal and plasma membrane-restricted components, with the latter utilized for analysis.

3.3.7 Super-resolution microscopy

HEK293T cells transfected with 200 ng mScarlet-Kv2.1$_{WT}$ or mScarlet-Kv2.1$_{S586A}$-mScarlet and arterial myocytes were plated onto collagen coated glass coverslips (Neuvitro Corporation, #GG-18-1.5-Collagen) followed by fixation with 3% formaldehyde and 0.1% glutaraldehyde diluted in PBS for 15 min at room temperature. After washing with PBS, cells were incubated with 50 mM glycine (BioRad, Hercules, CA) for 10 min to quench aldehydes. Cells were washed and incubated for one hour at room temperature with a blocking buffer made with 3% w/v BSA and 0.25% Triton X-100 in PBS. Cells were then incubated with either mouse anti-Kv2.1 (HEK293T experiments, mAb K89/34; RRID: AB_2877280; UC Davis/NIH Neuromab Facility, Davis, CA; 1:20) or mouse anti-Ca_V1.2 (arterial myocytes experiments, mAb L57/23; RRID: AB_2802123; 1:5). After extensive washings with PBS (three quick washes followed by three 30-min washes), cells were incubated at room temperature for one hour with Alexa Fluor 647-conjugated goat anti-mouse diluted in blocking buffer to a concentration of 2 µg/ml and afterwards extensively washed with PBS.

The imaging buffer contained 10 mM MEA, 0.56 mg/ml glucose oxidase, 34 µg/ml catalase, and 10% w/v glucose in TN buffer (200 mM Tris-HCl pH 8, 10 mM NaCl). A super resolution ground state deletion system (SR-GSD, Leica, Wetzlar, Germany) based on stochastic single-molecule localization was used to generate super-resolution

images of $Ca_V1.2$ and $K_V2.1$ labeling. The Leica SR-GSD is a Leica DMI6000B TIRF microscope system equipped with a 160x HCX Plan-Apochromat (NA 1.43) oil-immersion lens and an EMCCD camera (iXon3 897, Andor Technology, Belfast, United Kingdom). Fluorophores were excited with a 642 nm laser (used for both pumping to the dark state and image acquisition). For all experiments, the camera was running in frame-transfer mode at a frame rate of 100 Hz (11 ms exposure time). Fluorescence was detected through Leica high power TIRF filter cubes (488 HP-T, 532 HP-T, 642 HP-T) with emission band-pass filters of 505-605 nm, 550-650 nm, and 660-760 nm. A total of 35,000 images were collected per cell and used to construct the super resolution localization images. Fluorescence signals in each image were fit with a 2D Gaussian function which localized the coordinates of centroids of single molecule fluorescence within the LASAF software (Leica). Images were rendered at 20 nm/pixel (normalized Gaussian mode), threshold (# photons/event) using the GSD software and exported as binary TIF images. Particle analyses were determined in ImageJ. Representative images were rendered down to 2 nm for visualization purposes.

To accomplish the Gaussian blur, the GSD generated pixel in an image was replaced by a weighted average of 200 nm of its neighboring pixels. The amount of blur applied to the image was controlled by the size of the kernel, which determines the radius of the neighboring pixels used in the calculation, such that the larger the kernel, the more pixels are included in the calculation, and the stronger the blur effect.

3.3.8 Quantitative PCR

Total RNA was isolated using the RNeasy Mini Kit (Qiagen) as per manufacturer's instructions. Isolated mRNA was then reverse transcribed using the AffinityScript qPCR cDNA Synthesis Kit (Agilent) following manufacturer's protocol. Quantitative PCR (qPCR) analysis was performed using a QuantStudio 7 Pro Real-time PCR System (Applied Biosystems), using PowerUP SYBR Green Master Mix (Thermo Fisher Scientific) as the fluorescence probe. The cycling conditions were 50°C for 2 minutes and 95°C for 10 minutes, followed by 40 cycles of 95°C for 15 s and 56°C for 1 minute. A dissociation curve protocol (ramping temperatures between 60°C and 95°C) was added at the end to verify amplification specificity of each qPCR reaction.

Specific primers were designed in this experiment, including **β-actin** (NM_007393.5): sense nt (895-914): CCAGCCTTCCTTCTTGGGTA, antisense nt (989-967): AGAGGTCTTTACGGATGTCAACG; and **$Ca_V1.2$** (NM_009781.4): sense nt (5-23): CTGAAAGCAGAAGCTCGGA, antisense nt (181-163): CATTGTGGCTTCCAGTTGG. Primer efficiencies were tested to be in between 90% and 110%. The relative abundance of $Ca_V1.2$ transcript was normalized to β-actin transcript expression.

3.3.9 Proximity Ligation Assay

A Duolink In Situ PLA kit (Sigma) was used to detected $K_V2.1$-$K_V2.1$ and $K_V2.1$-$Ca_V1.2$ complexes in freshly isolated mesenteric arterial myocytes. All protocols post incubation of primary antibodies were followed in accordance with the manufacturer's instructions. Briefly, cells were plated on glass coverslips and allowed to adhere for 1 hour at room temperature. Cells were fixed with 4% paraformaldehyde for 20 minutes, quenched in

10mM glycine for 15 min, washed in PBS two times for three minutes, and permeabilized 20 minutes in 0.1% Triton X-100. After blocking for 1 hour at 37˚C in Duolink Blocking Solution, cells were incubated overnight at 4˚C using the following primary antibodies: mouse anti-Kv2.1 (mAb K89/34; RRID: AB_2877280; UC Davis/NIH Neuromab Facility, Davis, CA; 1:200), rabbit anti-Kv2.1 (KC(*292*); RRID:AB_2315767; 1:100) and rabbit anti-$Ca_V1.2$. The anti-$Ca_V1.2$ rabbit polyclonal antibody "$Ca_V1.2$ II-III" was generated by immunizing two New Zealand white rabbits with a His-tagged recombinant protein fragment corresponding to a.a. 785-900 of mouse $Ca_V1.2$ (accession number Q01815). Antibodies were affinity purified from serum on nitrocellulose strips containing the $Ca_V1.2$ II-III His-tagged recombinant protein fragment following the method of Olmsted(*298*). Cells incubated with only one primary antibody served as negative controls. Secondary oligonucleotide-conjugated antibodies (PLA probes: anti-mouse MINUS and anti-rabbit PLUS) were used to detect $K_V2.1$ and $Ca_V1.2$ interactions. Fluorescent signal was detected using an Olympus FV3000 confocal microscope equipped with a 60x oil immersion lens (NA = 1.40). Images were collected with a z-axis of 0.5 µm/step optical planes. Stacks of images were combined in ImageJ and used for analysis of puncta/μm^2 per cell.

3.3.10 Patch-clamp electrophysiology

All electrophysiological recordings were acquired at room temperature using an Axopatch 200B amplifier and Digidata 1440 digitizer (Molecular Devices, Sunnyvale, CA). Borosilicate patch pipettes were pulled and polished to resistances of 3-6 MΩ using a micropipette puller (model P-97, Sutter Instruments, Novato, CA).

$I_{Kv2.1}$ was measured in arterial myocytes using conventional whole-cell voltage-clamp electrophysiology at a frequency of 50 kHz and low-pass filter of 2 kHz. Cells were continuously perfused with an external solution containing (in mM) 130 NaCl, 5 KCl, 3 $MgCl_2$, 10 glucose, and 10 HEPES adjusted to pH 7.4 with NaOH. Micropipettes were filled with an internal solution containing (in mM) 87 K-aspartate, 20 KCl, 1 $CaCl_2$, 1 $MgCl_2$, 5 MgATP, 10 EGTA, and 10 HEPES pH 7.2 with KOH. A liquid junction potential of 13 mV was corrected for offline. To measure current-voltage relationships, cells were subjected to a series of 500 ms test pulses increasing from -70 mV to +70 mV. In order to isolate the RY785-sensitive Kv2 current, cells were first bathed and recorded in external solution. Cells were then exposed to 1μM RY785 (MedChemExpress) to inhibit Kv2.1 activity. RY785-sensitive currents were calculated by subtracted the RY785 exposed traces from the composite I_K traces.

I_{Ca} was measured in isolated arterial myocytes using conventional whole-cell electrophysiology. Currents were measured at a frequency of 50 kHz and low-pass filtered at 2 kHz. Myocytes were continuously bathed in an external solution with (in mM) 115 NaCl, 10 TEA-Cl, 0.5 $MgCl_2$, 5.5 glucose, 5 CsCl, 20 $BaCl_2$, and 10 HEPES adjusted to a pH of 7.4 using CsOH. Micropipettes were filled with (in mM) 20 CsCl, 87 aspartic acid, 1 $MgCl_2$, 10 HEPES, 5 MgATP, and 10 EGTA adjusted to pH 7.2 via CsOH. A voltage error of 9.4 attributed to the liquid junction potential of the recording solutions was corrected for offline. Cells were exposed to a series of 300 ms

depolarizing pulses from a holding potential of -70 mV to test potentials ranging from -70 mV to +60 mV to attain current-voltage relationships.

3.3.11 Bimolecular fluorescence complementation

Spontaneous interactions of $Ca_V1.2$ channels were assayed using biomolecular fluorescence complementation. HEK293T cells were transfected with $Ca_V1.2$ channels tagged at their C-terminus to either a non-fluorescent N-(VN(1-154, I152L)) or C-terminal (VC(155-238, A206K)) halves of a 'split' Venus fluorescent protein. When $Ca_V1.2$-VN and $Ca_V1.2$-VC are brought close enough together to interact, the full Venus protein can fold into its functional, fluorescent conformation. The scale of Venus fluorescence emission can therefore be an indicator of $Ca_V1.2$-$Ca_V1.2$ interactions. Venus fluorescence was monitored using TIRF microscopy.

For whole-cell current recordings from HEK293T cells, pipettes were filled with a solution containing (mM) 84 Cs-aspartate, 20 CsCl, 1 $MgCl_2$, 10 HEPES, 1 EGTA, and 5 MgATP adjusted to pH 7.2 using CsOH. HEK293T cells were continuously perfused with an external solution comprising of (in mM) 5 CsCl, 10 HEPES, 10 glucose, 140 NMDG, 1 $MgCl_2$, and 20 $CaCl_2$ with a pH of 7.4 (HCl).

3.3.12 $Ca_V1.2$ sparklets

Ca^{2+} sparklets were recorded using a through-the-lens TIRF microscope built around an inverted microscope (IX-70; Olympus) equipped with a Plan-Apochromat (60X; NA 1.49) objective (Olympus) and an electron-multiplying charge-coupled device (EMCCD)

camera (iXON; Andor Technology, UK). Myocytes were loaded via the patch pipette with a solution containing (in mM) 0.2 Fluo-5F (Invitrogen # F14221), 87 Cs-aspartate, 20 CsCl, 1 $MgCl_2$, 5 MgATP, 10 HEPES, 10 EGTA, pH 7.2 with CsOH. Cells were perfused in an external solution containing 140 NMDG, 5 CsCl, 51 $MgCl_2$, 10 glucose, 10 HEPES, 2 $CaCl_2$, pH 7.4 with HCl. After obtaining a GΩ seal in 2mM Ca^{2+} external solution, the cell was broken into and allowed to dialyze for 3 minutes. The external solution was exchanged with a solution containing (in mM) 120 NMDG, 5 CsCl, 1 $MgCl_2$, 10 glucose, 10 HEPES, 20 $CaCl_2$, pH 7.4 with HCl. Images for the detection of sparklets were recorded at a frequency of 100 Hz using TILL Image software. Cells were held to a membrane potential of −70 mV using the whole-cell configuration of the patch-clamp technique. Sparklets were automatically detected and later analyzed using custom software (Source code 2) written in MATLAB (RRID:SCR_001622) as previously described (*240*).

3.3.13 In silico modeling

Simulations were performed using the Sato et al. (*285*) and Hernandez-Hernandez et al. (*299*) mathematical models for cluster formation and smooth muscle electrophysiology, respectively.

3.3.14 Chemicals and statistics

All chemical reagents were acquired from Sigma-Aldrich (St. Louis, MO) unless otherwise stated. Data was expressed as mean ± SEM and analyzed using GraphPad Prism software. Statistical significance was determined using appropriate paired or

unpaired T-tests, non-parametric tests, or one-way analysis of variance (ANOVA). $P < 0.05$ was considered statistically significant and denoted by * in the figures.

3.4 Results

3.4.1 $K_V2.1$ macro-clusters are composed of micro-clusters of $K_V2.1$ and are declustered by the $K_V2.1_{S586A}$ mutation

We began our study by determining the spatial distribution in heterologous cells of exogenously expressed wild-type rat $K_V2.1$ ($K_V2.1_{WT}$) channels and $K_V2.1$ channels in which serine at position 586 was mutated to an alanine ($K_V2.1_{S586A}$) using confocal and super-resolution ground state depletion (GSD) microscopy (**Figure 3.1**). Both channels were tagged at their N-terminus with the red-shifted fluorescent protein mScarlet.

Figure 3.1A shows confocal maximum intensity projection images of 3D reconstructions of representative HEK293T cells expressing $K_V2.1_{WT}$ (left) and $K_V2.1_{S586A}$ (right). To the right of each image, we show single plane images from the bottom (top panel) and center (bottom panel) of each cell. **Figure 3.1B-E** shows a quantitative analysis of the number and volume of $K_V2.1$ clusters from these 3D confocal images. The frequency distributions of $K_V2.1_{WT}$ (black) and $K_V2.1_{S586A}$ (blue) cluster volumes could be fit with a single exponential function. Of note, the number of clusters were smaller in most volume bins for the $K_V2.1_{S586A}$ mutation compared to $K_V2.1_{WT}$. For example, in the same number of cells (n = 7), we detected a total of 6,344 $K_V2.1_{WT}$ clusters, but only 3,335 $K_V2.1_{S586A}$ clusters. The number of clusters per cell was 594.4 ± 52.7 in $K_V2.1_{WT}$ (median = 542 clusters) and 318.2 ± 42.7 clusters in $K_V2.1_{S586A}$ (median = 299 clusters)

(P = 0.0003) (**Figure 3.1C**). The total cluster volume per cell of $K_V2.1_{WT}$ was 50.8 ± 5.7 μm^3 (median = 47.8 μm^3) compared to 25.4 ± 4.7 μm^3 in cells expressing $K_V2.1_{S586A}$ (median = 19.8 μm^3) (P = 0.001) (**Figure 3.1D**). Interestingly, the mean cluster volumes were not significantly different between $K_V2.1_{WT}$ channels at 0.09 ± 0.01 μm^3 (median = 0.08 μm^3) and $K_V2.1_{S586A}$ at 0.09 ± 0.01 μm^3 (median = 0.08 μm^3) (**Figure 3.1E**). These data suggest that $K_V2.1_{WT}$ channels are expressed into clusters and that $K_V2.1_{S586A}$ expression is more diffuse and exhibits a more uniform distribution.

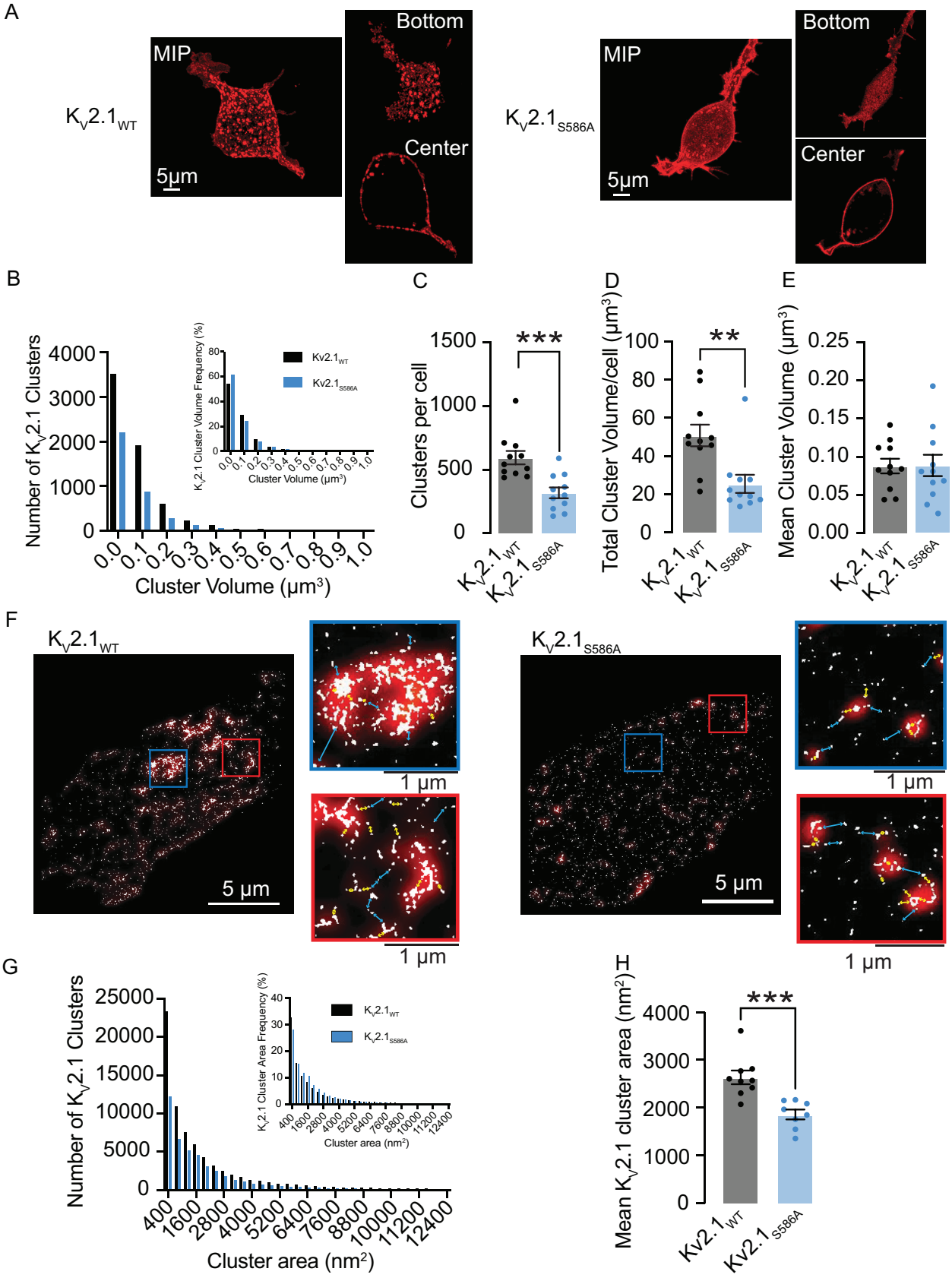
A
$K_V2.1_{WT}$
MIP
5µm
Bottom
Center
$K_V2.1_{S586A}$
MIP
5µm
Bottom
Center
B
Number of $K_V2.1$ Clusters
Cluster Volume (µm³)
$K_V2.1$ Cluster Volume Frequency (%)
Cluster Volume (µm³)
$Kv2.1_{WT}$
$Kv2.1_{S586A}$
C
Clusters per cell
***
$K_V2.1_{WT}$
$K_V2.1_{S586A}$
D
Total Cluster Volume/cell (µm³)
**
$K_V2.1_{WT}$
$K_V2.1_{S586A}$
E
Mean Cluster Volume (µm³)
$K_V2.1_{WT}$
$K_V2.1_{S586A}$
F
$K_V2.1_{WT}$
5 µm
1 µm
1 µm
$K_V2.1_{S586A}$
5 µm
1 µm
1 µm
G
Number of $K_V2.1$ Clusters
Cluster area (nm²)
$K_V2.1$ Cluster Area Frequency (%)
$K_V2.1_{WT}$
$K_V2.1_{S586A}$
Cluster area (nm²)
H
Mean $K_V2.1$ cluster area (nm²)
***
$Kv2.1_{WT}$
$Kv2.1_{S586A}$

Figure 3.1 $K_V2.1$ macro-clusters are declustered into micro-clusters with the $K_V2.1_{S586A}$ point mutation. (A) Confocal maximum intensity projection images of HEK293T cells transfected with $K_V2.1_{WT}$ (left) or $K_V2.1_{S586A}$ (right) tagged with mScarlet. Insets show single plane images of the bottom or center of each cell. (B) Number of $K_V2.1$ cluster volumes of $K_V2.1_{WT}$ (black) and $K_V2.1_{S586A}$ (blue) in transfected HEK293T cells. Insets quantify relative frequency histograms as a percentage of $K_V2.1$ volumes. Plots representing (C) number of clusters per cell, (D) total cluster volume per cell, and (E) mean cluster volumes. (F) Representative super-resolution GSD images of immunolabeled $K_V2.1$ channels in transfected HEK293T cells. Insets show 4 μm^2 regions of interest. Red overlay depicts Gaussian blur. Cyan lines indicate distances of greater than 200 nm while yellow arrows represent distances less than 200 nm. (G) Number of clusters of $K_V2.1_{WT}$ (black) and $K_V2.1_{S586A}$ (blue) by cluster area in transfected HEK293T cells. Insets quantify relative frequency histograms as a percentage of $K_V2.1$ areas. (H) Summary plot of mean $K_V2.1$ cluster areas from super-resolution images. *P < 0.05, **P < 0.01, ***P < 0.001. Error bars indicate mean ± SEM.

Figure 3.1F provides representative super-resolution GSD TIF images (lateral resolution ≈ 40 nm) from representative cells expressing $K_V2.1_{WT}$ or $K_V2.1_{S586A}$. Note that data are provided on an area basis since we are imaging a single plane footprint of the cell in contrast to capturing multiple Z-slices. We also provide two regions of interest (boxed areas) by each image. $K_V2.1_{WT}$ and $K_V2.1_{S586A}$ channels are organized into clusters of varied sizes (**Figure 3.1G**), and consistent with the lower resolution confocal data, the distribution of $Kv2.1_{S586A}$ channel clusters was more diffuse than that of

$K_V2.1_{WT}$. It should be noted that the regions of interest (ROI) of our GSD images reveal that the macro-clusters observed at the confocal level are, in fact, made up of numerous micro-clusters.

To increase our confidence in this observation, we utilized a Gaussian blur (shown in red) to decrease the resolution of the GSD signal to match that of confocal microscopy. Cyan arrows indicate distances greater than 200 nm between signals produced by GSD, while yellow arrows indicate distances less than 200 nm (**Figure 3.1F, insets**). Notably, our GSD image with a Gaussian blur accurately reproduced the clustering phenotype of $K_V2.1_{WT}$ at the confocal level, providing further evidence that macro-clusters are composed of micro-clusters. Although we do not observe the large macro-clusters in $K_V2.1_{S586A}$ expressing cells, we can still resolve $K_V2.1$ micro-clusters.

The frequency distribution of the cluster areas of $K_V2.1_{WT}$ and $K_V2.1_{S586A}$ obtained from GSD imaging could both be fit with an exponential function (**Figure 3.1G**). The mean cluster area of $K_V2.1_{WT}$ was 2634 ± 143 nm^2 (median = 2568 nm^2), larger than that of $K_V2.1_{S586A}$ channels which was 1860 ± 104 nm^2 (median = 1907 nm^2) (P = 0.0003) (**Figure 3.1H**). This is likely due to the absence of larger clusters in cells expressing $K_V2.1_{S586A}$. Notably, cluster density was 41 ± 5 clusters per micron and 29 ± 4 clusters per micron for $K_V2.1$ and $K_V2.1_{S586A}$, respectively.

Our finding that the size distributions of $K_V2.1_{WT}$ and $K_V2.1_{S586A}$ clusters could be described by exponential functions, the hallmark of a *Poisson* process, suggests that

these clusters are formed stochastically (*300*). To test this hypothesis, we implemented the stochastic modeling approach employed by Sato et al. (*285*) to determine whether we could reproduce our cluster distributions and make testable predictions regarding plasma membrane protein organization. As shown in **Figure 3.2,** our stochastic self-assembly model effectively reproduced the steady-state size distributions that we measured for $K_V2.1_{WT}$ and $K_V2.1_{S586A}$ proteins embedded in the surface membrane of HEK293T cells. The parameters used in the model are summarized in **Figure 3.2C**. These *in silico* data suggest that in HEK293T cells, $K_V2.1_{WT}$ has a higher probability of nucleation (i.e., P_n) and cluster growth (i.e., P_g) than $K_V2.1_{S586A}$ channels. The probability of channel removal (P_R) was similar.

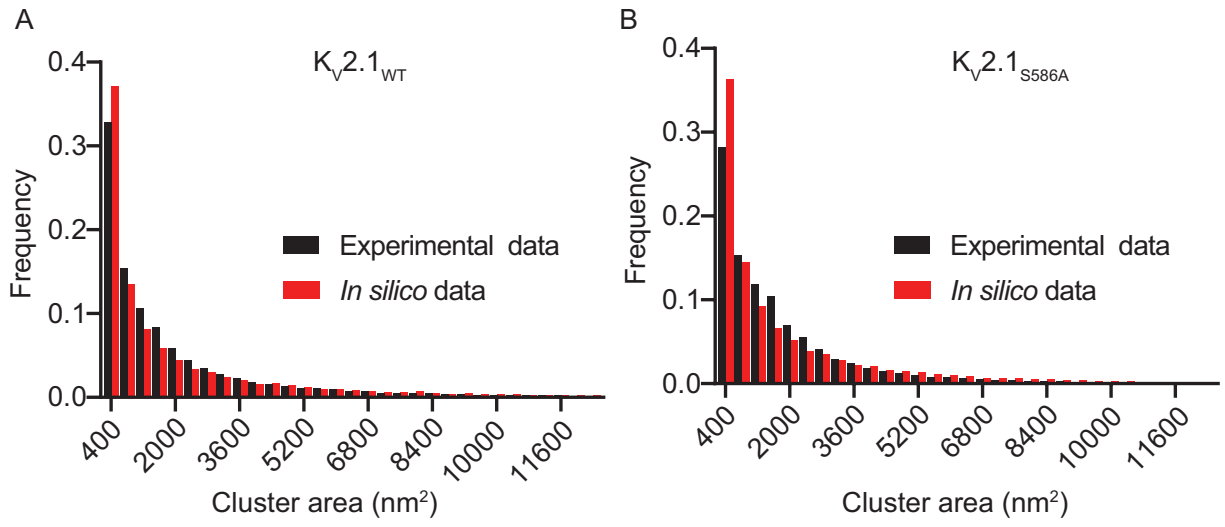

C

Channel	P_n	P_g	P_R	Mean experimental cluster size (nm^2)	Mean *in silico* cluster size (nm^2)	Mean experimental cluster density (clusters/μm^2)	Mean *in silico* cluster density (clusters/μm^2)
$K_V2.1_{WT}$	0.00050303	0.16532	0.001	2634 ± 143	2634.1	41 ± 4.7	40.389
$K_V2.1_{S586A}$	0.000098767	0.050355	0.001	1860 ±104	1867.3	29 ± 3.7	28.758

Figure 3.2 The distributions of $K_V2.1_{WT}$ and $K_V2.1_{S586A}$ in HEK293T cells could be explained by a stochastic self-assembly mechanism. (A) Histograms of experimental (black bars) and simulated (red bars) cluster area distributions as a relative frequency of $K_V2.1_{WT}$ in HEK293T cells. (B) Histograms of experimental (black bars) and simulated (red bars) cluster area distributions as a relative frequency of $K_V2.1_{S586A}$ in HEK293T cells. (C) Summary of experimental and *in silico* data.

Analysis of our confocal microscopy data showed that in HEK293T cells, $K_V2.1_{WT}$ is expressed in clusters of different sizes but do in fact form large macro-clusters. Using this confocal microscopy analysis, we sought to define the size of a $K_V2.1$ macro-cluster. We began with the mean cluster volume of $K_V2.1_{WT}$ generated in **Figure 3.1E.** Our analysis provided a mean cluster volume of 0.09 μm^3. Assuming the volume of a cluster is spherical, we extrapolated the diameter of the macro-cluster to be 560 nm. The standard deviation of these measurements was 0.32. Thus, the mean minus 2 standard deviations provides a lower end limit with a 95% confidence and aligned with the lateral resolution of our confocal microscopy. Accordingly, we define the lower limit of a macro-cluster as a cluster that is larger than 0.03 μm^3 or 326 nm in diameter, with clusters smaller than this classified as micro-clusters.

3.4.2 $K_V2.1_{S590A}$ mutation does not affect overall $K_V2.1$ channel expression but declusters smooth muscle $K_V2.1$ channels in a sex-specific manner

Next, we investigated whether, as in heterologous expression system (i.e., **Figure 3.1**), $K_V2.1$ channels cluster in arterial myocytes and whether this clustering could be

disrupted via mutation of critical amino acids in the PRC domain. To do this, we used Crispr/CAS gene editing to generate a knock-in mouse line expressing the S590A point mutation, corresponding to the S586A mutation in rat $K_v2.1$, at the KCNB1 locus of a C57/BL6J mouse (see Methods section for a full description of how these mice were generated).

We isolated, fixed, permeabilized, and labeled arterial myocytes from both male and female $K_V2.1_{WT}$ and $K_V2.1_{S590A}$ knock-in mice. We double labeled with wheat germ agglutinin-488 (WGA488) to identify the sarcolemma and $K_V2.1$-specific antibodies in male and female $K_V2.1_{WT}$ and $K_V2.1_{S590A}$ myocytes using confocal microscopy. **Figure 3.3A and 3.3G** show representative 3D images of fixed mesenteric smooth muscle cells labeled with WGA488 and immunolabeled for $K_V2.1$.

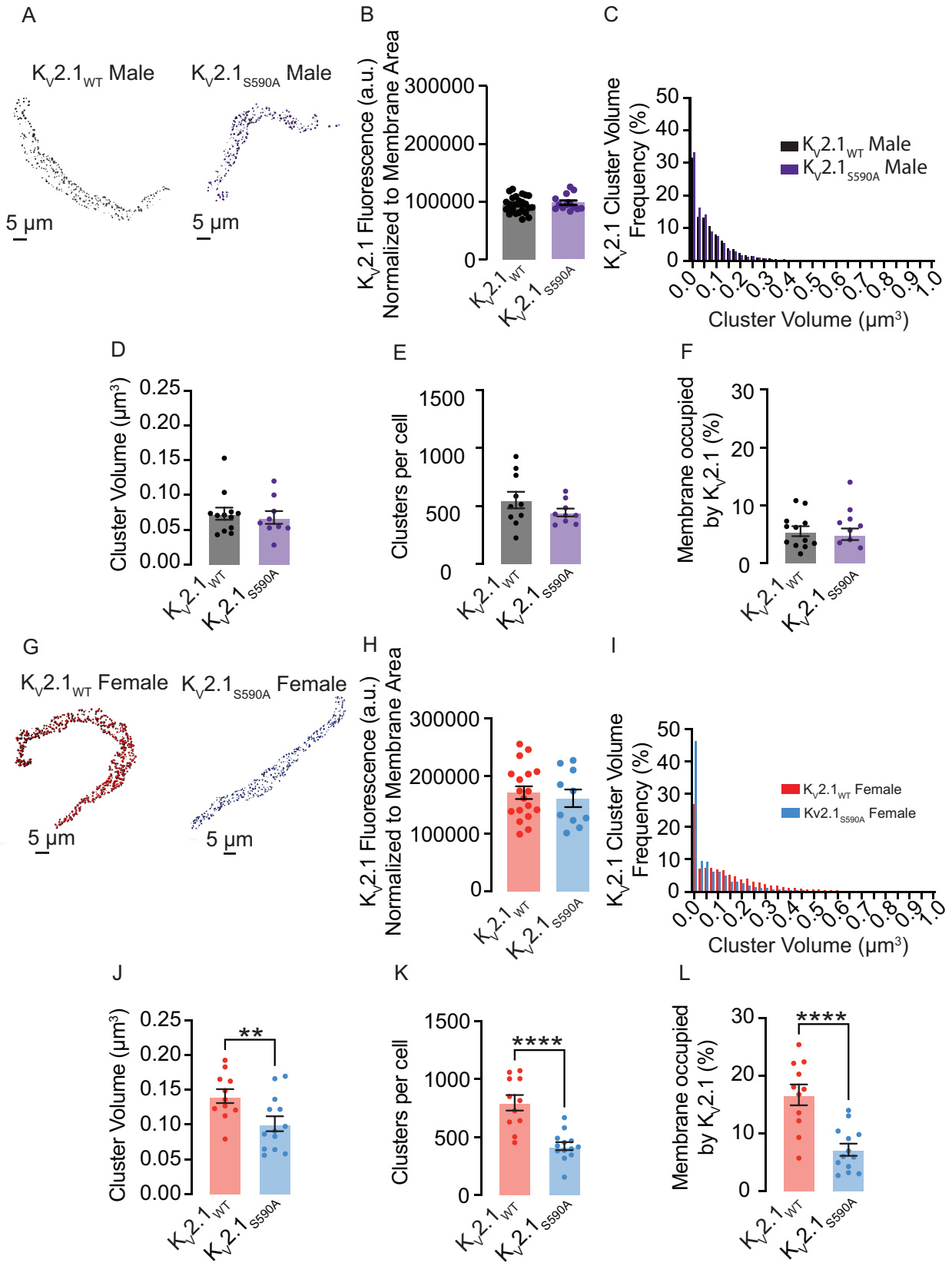
A
$K_V2.1_{WT}$ Male
$K_V2.1_{S590A}$ Male
5 µm
5 µm
B
$K_V2.1$ Fluorescence (a.u.) Normalized to Membrane Area
300000
200000
100000
0
$K_V2.1_{WT}$
$K_V2.1_{S590A}$
C
$K_V2.1$ Cluster Volume Frequency (%)
50
40
30
20
10
0
$K_V2.1_{WT}$ Male
$K_V2.1_{S590A}$ Male
0.0 0.1 0.2 0.3 0.4 0.5 0.6 0.7 0.8 0.9 1.0
Cluster Volume (µm³)
D
Cluster Volume (µm³)
0.25
0.20
0.15
0.10
0.05
0.00
$K_V2.1_{WT}$
$K_V2.1_{S590A}$
E
Clusters per cell
1500
1000
500
0
$K_V2.1_{WT}$
$K_V2.1_{S590A}$
F
Membrane occupied by $K_V2.1$ (%)
30
20
10
0
$K_V2.1_{WT}$
$K_V2.1_{S590A}$
G
$K_V2.1_{WT}$ Female
$K_V2.1_{S590A}$ Female
5 µm
5 µm
H
$K_V2.1$ Fluorescence (a.u.) Normalized to Membrane Area
300000
200000
100000
0
$K_V2.1_{WT}$
$K_V2.1_{S590A}$
I
$K_V2.1$ Cluster Volume Frequency (%)
50
40
30
20
10
0
$K_V2.1_{WT}$ Female
$Kv2.1_{S590A}$ Female
0.0 0.1 0.2 0.3 0.4 0.5 0.6 0.7 0.8 0.9 1.0
Cluster Volume (µm³)
J
Cluster Volume (µm³)
0.25
0.20
0.15
0.10
0.05
0.00
**
$K_V2.1_{WT}$
$K_V2.1_{S590A}$
K
Clusters per cell
1500
1000
500
0
****
$K_V2.1_{WT}$
$K_V2.1_{S590A}$
L
Membrane occupied by $K_V2.1$ (%)
30
20
10
0
****
$K_V2.1_{WT}$
$K_V2.1_{S590A}$

Figure 3.3 The $K_V2.1_{S590A}$ mutation declusters $K_V2.1$ channels in arterial smooth muscle in a sex-specific manner. (A, G) Representative maximum projection images of $K_V2.1$ channel clusters at the surface membrane of $K_V2.1_{WT}$ male (A**,** left), $K_V2.1_{S590A}$ male (A**,** right), $K_V2.1_{WT}$ female (G**,** left) and $K_V2.1_{S590A}$ female (G**,** right) myocytes. Quantification of immunofluorescence normalized to cell volume of labeled $K_V2.1$ in male (B) and female (H) myocytes. (C, I) Relative frequency as a percentage of $K_V2.1$ cluster volumes from $K_V2.1_{WT}$ male (C**,** black), $K_V2.1_{S590A}$ male (C**,** purple), $K_V2.1_{WT}$ female (I, red) and $K_V2.1_{S590A}$ female (I, blue) myocytes. Summary data of $K_V2.1$ clusters in male myocytes showing (D, J) mean cluster volumes, (E, K) clusters per cell, and (F, L) percent of the surface membrane occupied by $K_V2.1$ channels in male and female myocytes. *P<0.05, **P<0.01, ***P<0.001, ****P<0.0001. Error bars indicate mean ± SEM.

We investigated whether the $K_V2.1_{S590A}$ mutation leads to altered expression levels of the channel in arterial myocytes. Our analysis showed that total, cell-wide $K_V2.1$-associated fluorescence normalized to cell volume was similar in sex-matched $K_V2.1_{WT}$ and $K_V2.1_{S590A}$ myocytes (**Figure 3.3B, H**), suggesting that the $K_V2.1$ expression is similar in these cells.

Further analysis of $K_V2.1$ clusters was restricted to those that overlapped with the WGA-mapped plasma membrane. In both, the $K_V2.1_{WT}$ and $K_V2.1_{S590A}$ males, the frequency distribution of $K_V2.1$ cluster sizes were similar in terms of relative values in all volume bins and could be fit with an exponential decay function (**Figure 3.3C**). The mean

cluster volume in $K_V2.1_{WT}$ males was 0.07 ± 0.01 μm^3 (median = 0.07 μm^3) compared to a mean of 0.07 ± 0.01 μm^3 (median = 0.06 μm^3) in $K_V2.1_{S590A}$ male myocytes. (P = 0.338) (**Figure 3.3D**). Additionally, total clusters per cell of 551.6 ± 71.1 clusters, (median = 505 clusters) in $K_V2.1_{WT}$ male myocytes were not significantly different from total clusters per cell of 444.2 ± 33.4 clusters (median = 419 clusters) in $K_V2.1_{S590A}$ males (P = 0.10) (**Figure 3.3E).** The percentage of the membrane occupied by clusters in $K_V2.1_{WT}$ male myocytes was on average 5.5 ± 0.9% (median = 5.1%), similar to the average in $K_V2.1_{S590A}$ males of 5.0 ± 1.0% (median = 4.6%) (P = 0.34) (**Figure 3.3F**).

In sharp contrast to male myocytes, $K_V2.1_{S590A}$ female myocytes exhibited an increased proportion of smaller clusters as compared to those from $K_V2.1_{WT}$ females (**Figure 3.3I**). Accordingly, mean cluster size of $K_V2.1_{WT}$ in female myocytes was 0.14 ± 0.10 μm^3 (median = 0.14 μm^3), significantly larger than mean cluster size of 0.10 ± 0.01 μm^3 (median = 0.09 μm^3) (P = 0.007) in $K_V2.1_{S590A}$ females (**Figure 3.3J).** $K_V2.1_{WT}$ female myocytes had 796 ± 67 clusters per cell, (median = 815 clusters) compared to only 422 ± 34 clusters per cell (median = 415 clusters) in $K_V2.1_{S590A}$ female myocytes (P < 0.0001) **(Figure 3.3K)**. Similarly, the percentage of the plasma membrane occupied by $K_V2.1$ was higher in $K_V2.1_{WT}$ female myocytes at 16.7 ± 1.8% (median = 17.7%) in contrast to $K_V2.1_{S590A}$ female myocytes in which $K_V2.1$ clusters occupied on average 7.2 ± 1.0% of the plasma membrane (median = 6.0) (P < 0.0001) (**Figure 3.3L).** The significantly lower $K_V2.1$ clustering profile in all metrics measured indicates that unlike in males, the S590A mutation decreases channel clustering in female myocytes.

Using the threshold set from our confocal imaging (i.e., macro-clusters are >0.025μm^3), we quantified the number of macro-clusters expressed in myocytes from $K_V2.1_{WT}$ and $K_V2.1_{S590A}$ mice. Around 62% of clusters in $K_V2.1_{WT}$ male myocytes were identified as macro-clusters, with a similar percentage of 58% observed in samples from males with the $K_V2.1_{S590A}$ mutation. Approximately 70% of $K_V2.1$ clusters in $K_V2.1_{WT}$ female myocytes were classified as macro-clusters. Remarkably, in $K_V2.1_{S590A}$ female myocytes, macro-clusters accounted for approximately 49% of the total $K_V2.1$ clusters.

We also quantified $K_V2.1$ micro-clusters. Although the proportion of micro-clusters was similar in male $K_V2.1_{WT}$ and $K_V2.1_{S590A}$ myocytes (38% and 42%, respectively), female $K_V2.1_{S590A}$ myocytes exhibited a much larger proportion of micro-clusters (51%) compared to myocytes from $K_V2.1_{WT}$ females (30%). Hence, it can be reasoned that the S590A mutation has a sex-specific effect of reducing the extent of $K_V2.1$ macro-clustering in female but not male arterial myocytes without impacting channel expression.

3.4.3 $K_V2.1$ phospho-S590 phosphorylation is higher in myocytes from female versus male $K_V2.1_{WT}$ mice

To investigate the potential role of the S590 phosphorylation site in the sex-specific differences in $K_V2.1$ clustering, we conducted immunocytochemistry analyses on arterial myocytes (**Figure 3.4**). We tested the hypothesis that $K_V2.1_{WT}$ female myocytes exhibit a higher degree of $K_V2.1$ S590 phosphorylation compared to males, which could contribute to the observed sex-specific variations in $K_V2.1$ clustering. Accordingly, we

utilized a monoclonal antibody (mAb L100/1; (*297*)) specific for $K_V2.1$ that is phosphorylated at serine 590 (pS590). **Figure 3.4A** shows cells double immunolabeled for pS590 (left) and total $K_V2.1$ (right) using confocal microscopy.

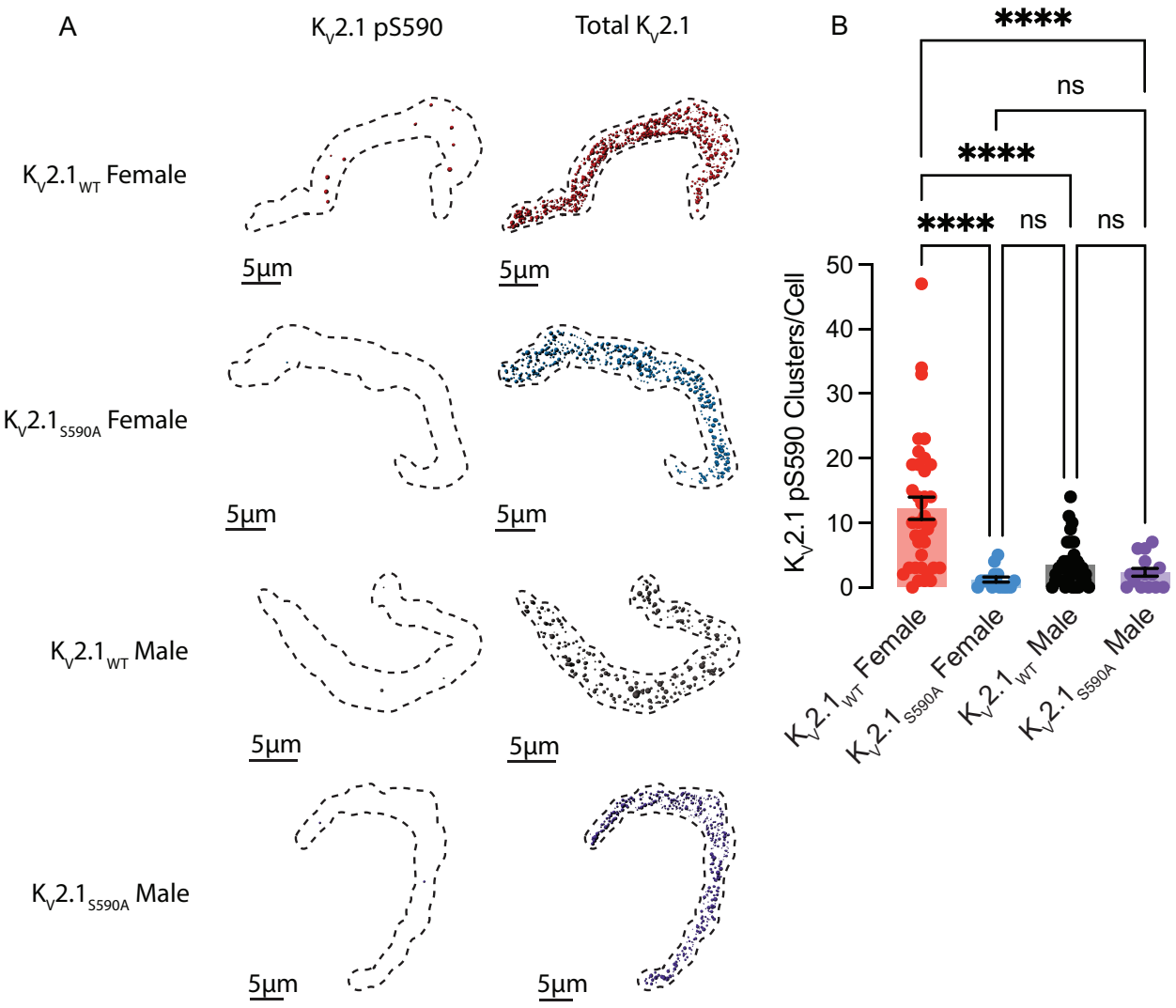

Figure 3.4 $K_V2.1_{WT}$ female myocytes exhibit more extensive $K_V2.1$ pS590 phosphorylation than those from $K_V2.1_{WT}$ males. (A) Representative maximum projection images of immunolabeling for pS590 $K_V2.1$ (left) and total $K_V2.1$channel clusters (right) at the surface membrane of $K_V2.1_{WT}$ female (red), $K_V2.1_{S590A}$ female (blue), $K_V2.1_{WT}$ male (black), and $K_V2.1_{S590A}$ male (purple) cells. (B) Summary data of

pS590 $K_V2.1$ clusters per cell. *P<0.05, **P<0.01, ***P<0.001, ****P<0.0001. Error bars indicate mean ± SEM.

One advantage of our study is that our $K_V2.1_{S590A}$ mice serve as an ideal negative control. As expected, $K_V2.1_{S590A}$ males exhibited 2.3 ± 0.6 clusters (median = 2.0 clusters) per cell and $K_V2.1_{S590A}$ females exhibited 1.2 ± 0.4 clusters (median = 1.0 clusters) per cell confirming the specificity of this mAb for $K_V2.1$ phosphorylated at S590. Remarkably, phosphorylated $K_V2.1$ clusters were observed in $K_V2.1_{WT}$ females (**Figure 3.4B**) exhibiting on average 12.2 ± 1.7 of phosphorylated clusters (median = 10.0 clusters) per cell, whereas $K_V2.1_{WT}$ males exhibited 3.4 ± 0.6 clusters (median = 2.5 clusters) per cell. Collectively, these findings suggest that basal levels of $K_V2.1$ S590 phosphorylation are higher in $K_V2.1_{WT}$ females, which could account for their increased clustering of $K_V2.1$. Furthermore, these data support the notion that $K_V2.1$ phosphorylation in $K_V2.1_{WT}$ male myocytes is constitutively low, making the S590A mutation functionally indistinguishable from non-phosphorylated $Kv2.1_{WT}$ and thus ineffective in altering $K_V2.1$ clustering in male myocytes.

3.4.4 Expression of clustering impaired $K_v2.1_{S590A}$ does not affect channel activity in arterial myocytes

Three studies, one using Xenopus oocytes(*168*), one using HEK293T cells (*170*) and another from our group using arterial myocytes (*287*) have suggested that the vast majority of $K_V2.1$ channels (i.e., 98-99%) expressed in the plasma membrane of these cells are non-conductive. O'Connell *et al(170)* suggested that, at least in HEK293T

cells, $K_V2.1$ channel activity depends on their density and that channels within large, dense macro-clusters are non-conductive. A testable hypothesis raised by these data is that a larger fraction of $K_V2.1_{S590A}$ should be conductive and hence the amplitude of $K_V2.1$ currents in native arterial myocytes should differ between cells from $K_V2.1_{WT}$ and $K_V2.1_{S590A}$ mice (**Figure 3.5**).

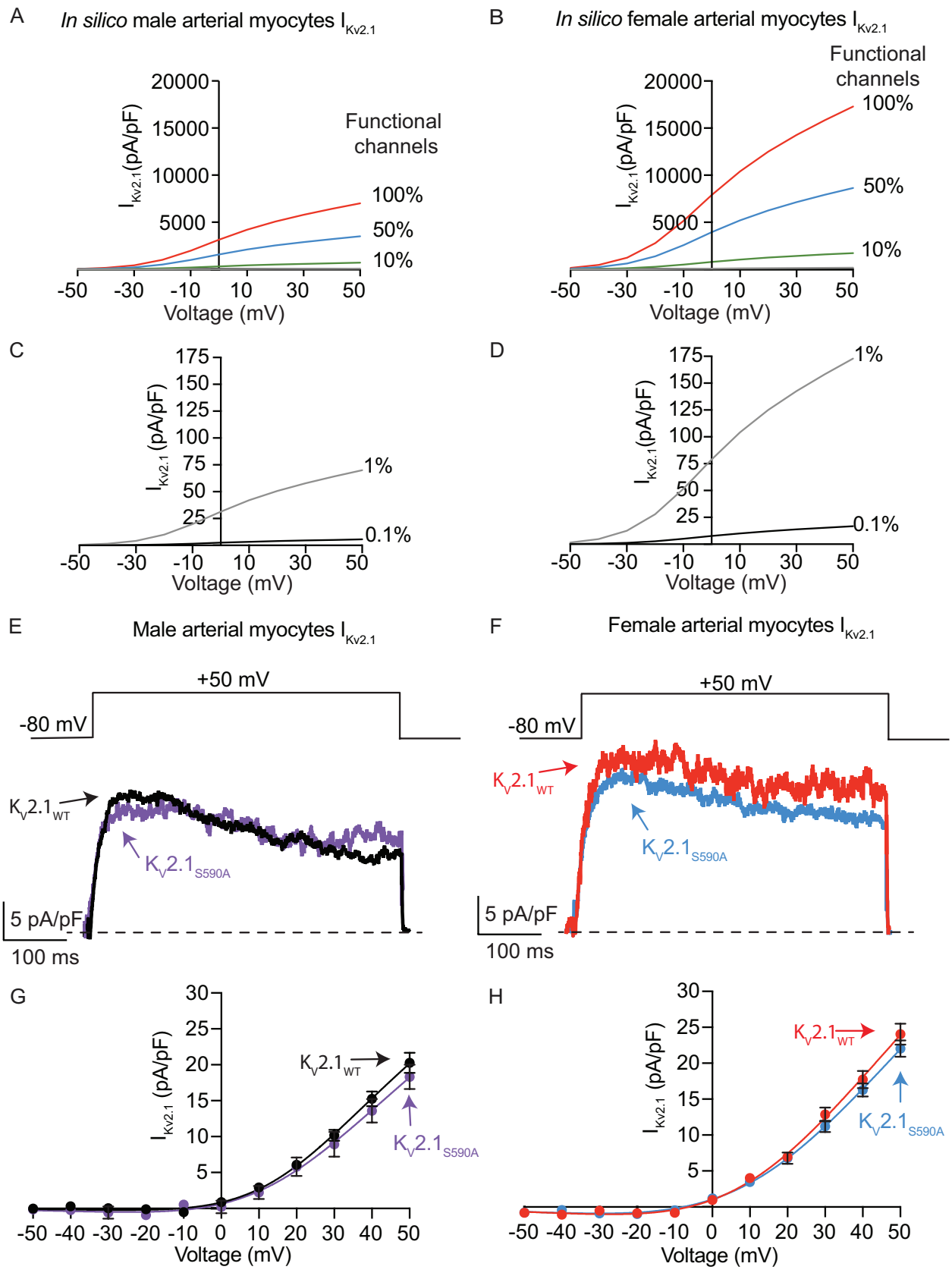
A
In silico male arterial myocytes I Kv2.1
I Kv2.1 (pA/pF)
Functional channels
100%
50%
10%
Voltage (mV)
B
In silico female arterial myocytes I Kv2.1
Functional channels
100%
50%
10%
Voltage (mV)
C
1%
0.1%
Voltage (mV)
D
1%
0.1%
Voltage (mV)
E
Male arterial myocytes I Kv2.1
+50 mV
-80 mV
K V 2.1 WT
K V 2.1 S590A
5 pA/pF
100 ms
F
Female arterial myocytes I Kv2.1
+50 mV
-80 mV
K V 2.1 WT
K V 2.1 S590A
5 pA/pF
100 ms
G
I Kv2.1 (pA/pF)
K V 2.1 WT
K V 2.1 S590A
Voltage (mV)
H
I Kv2.1 (pA/pF)
K V 2.1 WT
K V 2.1 S590A
Voltage (mV)

Figure 3.5 Expression of clustering impaired $K_V2.1_{S590A}$ does not affect $K_V2.1$ channel activity in arterial myocytes. Computationally modeled $I_{Kv2.1}$ in male (A) and female (B) myocytes assuming 100% (red), 50% (blue) or 10% (green) of $K_V2.1$ channels present in the plasma membrane are functional. Computationally modeled $I_{Kv2.1}$ in male (C) and female (D) myocytes assuming 1% (gray) and 0.1% (black) $K_V2.1$ channels are functional. (E) Representative $I_{Kv2.1}$ traces at +50 mV from $K_V2.1_{WT}$ male (black) and $K_V2.1_{S590A}$ male (purple) arterial myocytes. (F) Representative $I_{Kv2.1}$ traces at +50 mV from $K_V2.1_{WT}$ female (red) and $K_V2.1_{S590A}$ (blue) arterial myocytes. $I_{KV2.1}$ traces were obtained by subtracting currents after the application of RY785 from control I_K traces. Voltage dependence of $I_{Kv2.1}$ in $K_V2.1_{WT}$ and $K_V2.1_{S590A}$ male (G, black and purple) and $K_V2.1_{WT}$ and $K_V2.1_{S590A}$ female (H, red and blue) myocytes. Error bars indicate mean ± SEM.

We tested this hypothesis using a multipronged approach. First, we used a mathematical modeling approach (*299*) to determine the predicted changes in macroscopic $K_V2.1$ currents with varied levels of functional channels (i.e., 0.1, 1, 10, 50, or 100%) in male and female arterial myocytes (**Figure 3.5A-D**). The rationale for this analysis is that it provides a set of potential outcomes that can provide insights into the degree of $K_V2.1$ declustering in $K_V2.1_{S590A}$ myocytes. This model incorporated data (e.g., voltage-dependencies and number of channels in the sarcolemma) from O'Dwyer et al(*287*).

As shown in **Figure 3.5A**, the model predicts that with 100%, 50%, or 10% functional $K_V2.1$ channels in male myocytes would produce current densities at +50 mV of 7,006, 3,503, and 701 pA/pF, respectively. By contrast, at the same voltage, the *in silico* female arterial myocytes produce current densities of 17,293, 8,646, and 1,729 pA/pF with 100%, 50%, or 10% functional $K_V2.1$ channels (**Figure 3.5B**). We also simulated the current-voltage relationships in male (**Figure 3.5C**) and female (**Figure 3.5D**) myocytes assuming 1% and 0.1% of $K_V2.1$ channels are conductive, which are more within the range with previous experimental results in heterologous systems (*168, 170*) and native cells (*287*). The magnitude of *in silico* $K_V2.1$ current densities with 1% or 0.1% functional channels was 70.1 and 5.57 pA/pF in male myocytes and 173 and 16.7 pA/pF in female myocytes.

Next, we recorded voltage-gated K^+ (K_V) currents in male and female $K_V2.1_{WT}$ and $K_V2.1_{S590A}$ arterial myocytes in response to 500 ms depolarizations to voltages between -50 and +50 mV before and after applying the $K_V2.1$ blocker RY785 (1 μM) (*301, 302*). This compound decreases $K_V2.1$ currents by blocking the pore of these channels (*301*) rather than by immobilizing their voltage sensor, as stromatoxin does (*303*). As a first step in these experiments, we tested the specificity of the RY785 by recording Kv currents before and after the application of this molecule in male and female $K_V2.1_{WT}$ and $K_V2.1$ null ($K_V2.1^{-/-}$) myocytes (**Figure 3.6A-D)**. Notably, application of 1 μM RY785 decreased the amplitude of K^+ currents in $K_V2.1_{WT}$ but not in $K_V2.1^{-/-}$ myocytes of either sex. This indicates that RY785 is a specific blocker of $K_V2.1$ channels in arterial myocytes.

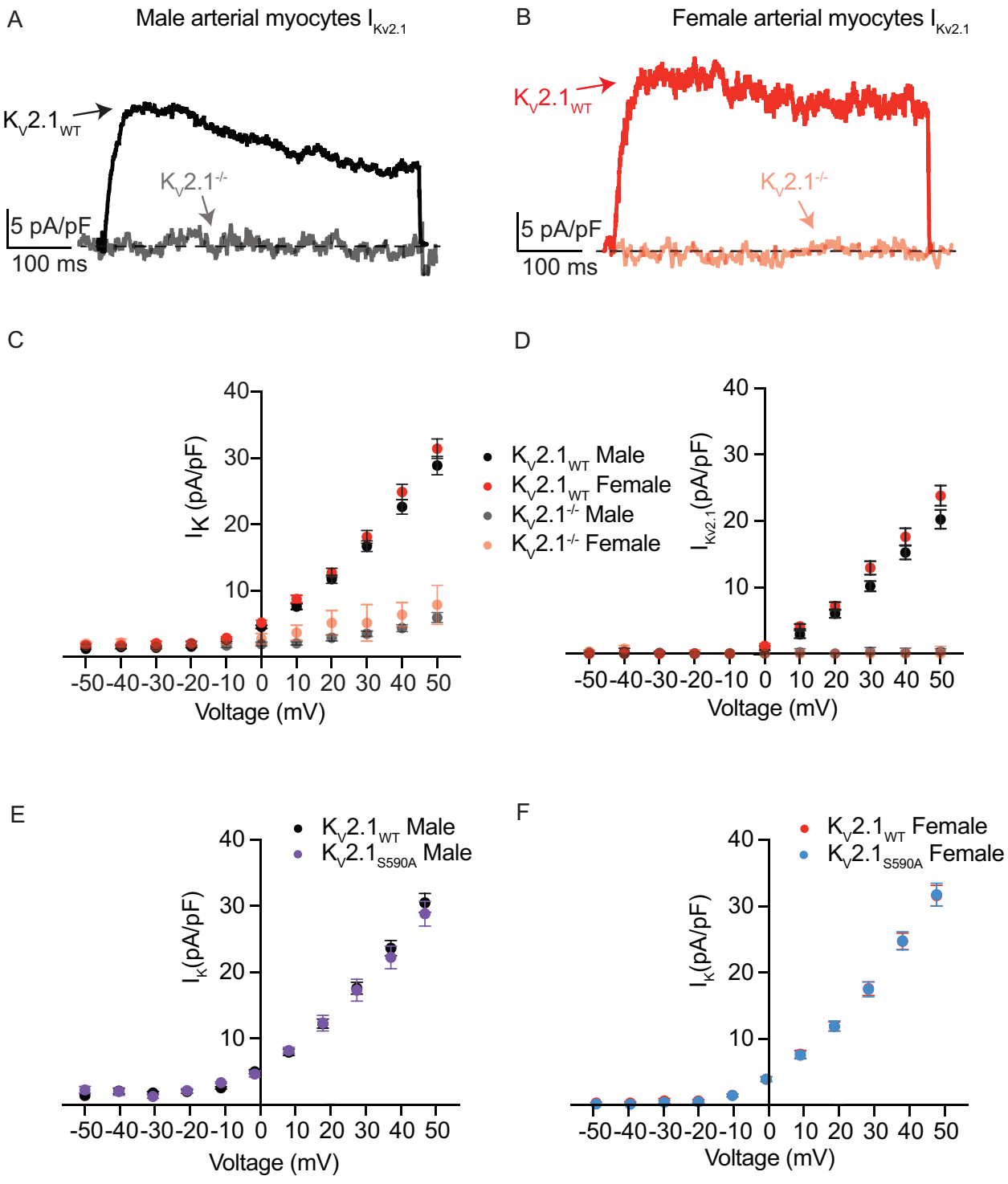

Figure 3.6 K^+ currents in $K_V2.1_{WT}$, $K_V2.1^{-/-}$ null and $K_V2.1_{S590A}$ myocytes. (A) Representative RY785-sensitive traces at +50 mV from $K_V2.1_{WT}$ (black) and $K_V2.1^{-/-}$ null

(gray) males myocytes. (B) Representative traces at +50 mV from $K_V2.1_{WT}$ (red) and $K_V2.1^{-/-}$ null (pink) female myocytes. (C) IV relationship of total K^+ current (I_K) recorded from $K_V2.1_{WT}$ male (black), $K_V2.1^{-/-}$ null male (gray), $K_V2.1_{WT}$ female (red), and $K_V2.1^{-/-}$ null female (pink) myocytes. (D) IV relationship of RY785-sensitive (Kv2.1) currents recorded from $K_V2.1_{WT}$ male (black), $K_V2.1^{-/-}$ null male (gray), $K_V2.1_{WT}$ female (red), and $K_V2.1^{-/-}$ null female (pink) myocytes. (E) IV relationship of total K^+ current (I_K) recorded from $K_V2.1_{WT}$ male (black) and $K_V2.1_{S590A}$ male (purple) myocytes. (F) IV relationship of total K^+ current (I_K) recorded from $K_V2.1_{WT}$ female (red) and $K_V2.1_{S590A}$ female (blue) myocytes.

Having completed these critical control experiments, we recorded K_V currents from $K_V2.1_{WT}$ and $K_V2.1_{S590A}$ myocytes. We noted that the amplitude of the composite K currents were similar in myocytes from $K_V2.1_{S590A}$ mice compared to myocytes from sex-matched $K_V2.1_{WT}$ littermates (**Figure 3.6C)**. Importantly, for both sexes, RY785-sensitive $K_V2.1$ currents were also similar in male (**Figure 3.5E, G**) and female (**Figure 3.5F, H**) $K_V2.1_{WT}$ and $K_V2.1_{S590A}$ myocytes. Indeed, a comparison of the experimental and in silico amplitudes of the macroscopic $K_V2.1$ currents suggests that less than 1% of the channels are functional in myocytes from both male and female $K_V2.1_{WT}$ and $K_V2.1_{S590A}$ mice. When taken together with our analyses of Kv2.1 clustering detailed above, these findings suggest that in arterial myocytes $K_V2.1$ channel activity is not determined by the extent and nature of its clustering.

3.4.5 The $K_V2.1_{S590A}$ mutation diminishes $K_V2.1$ and $Ca_V1.2$ interactions in female myocytes

We used the proximity ligation assay (PLA) to interrogate the impact of the $K_V2.1_{S590A}$ mutation on protein-protein interactions, at a resolution of approximately 40 nm (*304, 305*) (**Figure 3.7**). We first evaluated $K_V2.1$-$K_V2.1$ interactions within isolated mesenteric smooth muscle cells by using two different antibodies directed against different epitopes in the $K_V2.1$ cytoplasmic C-terminus. In this case both intra- and inter-molecular proximity of the two epitopes would yield a PLA signal. Inter-molecular interactions could be visualized as "puncta", and we hypothesized that more puncta would be exhibited in cells where $K_V2.1$ was more clustered since there would be increased proximity of epitopes due to intermolecular interactions, allowing for more PLA reactions to occur. Confocal images of $K_V2.1_{WT}$ and $K_V2.1_{S590A}$ myocytes subjected to PLA show that puncta of $K_V2.1$-$K_V2.1$ PLA signals were randomly distributed throughout the cell, and that PLA signal could be detected in all cells consistent with our confocal data above showing that $K_V2.1$ micro-clustering still occurs in mutant myocytes of both sexes (**Figure 3.7A**). The density of PLA puncta of 0.035 ± 0.003 puncta/μm^2 (median = 0.035 μm^2) in $K_V2.1_{WT}$ males was similar to 0.030 ± 0.003 puncta/μm^2 (median = 0.028 μm^2) in $K_V2.1_{S590A}$ male mice (P = 0.148) (**Figure 3.7B**). Consistent with the confocal imaging analysis, the density of $K_V2.1$- $K_V2.1$ PLA puncta was greater in $K_V2.1_{WT}$ females, with an average of 0.153 ± 0.011 puncta/μm^2 (median = 0.162 μm^2), compared to 0.046 ± 0.003 puncta/μm^2 (median = 0.037 μm^2) in $K_V2.1_{S590A}$ females (P < 0.0001) **Figure 3.7C**), suggesting that the $K_V2.1_{S590A}$ mutation reduces the level of $K_V2.1$ clustering in female myocytes.

Previous work from our group has shown that $K_V2.1$ expression promotes $Ca_V1.2$ clustering and activity in neurons (*288*) and arterial myocytes (*287*). Following from this and the data above, we hypothesize that in arterial myocytes $K_V2.1$ plays a sex-specific structural role as an organizer to bring $Ca_V1.2$ channels together in female but not male myocytes. We again used PLA to test the hypothesis that the declustering of $K_V2.1$ channels in female but not male myocytes from $K_V2.1_{S590A}$ mice would decrease $K_V2.1$-$Ca_V1.2$ channel interactions in a sex-specific manner. Representative images of $K_V2.1$-$Ca_V1.2$ PLA puncta show randomly distributed interactions across the cell (**Figure 3.7D**).

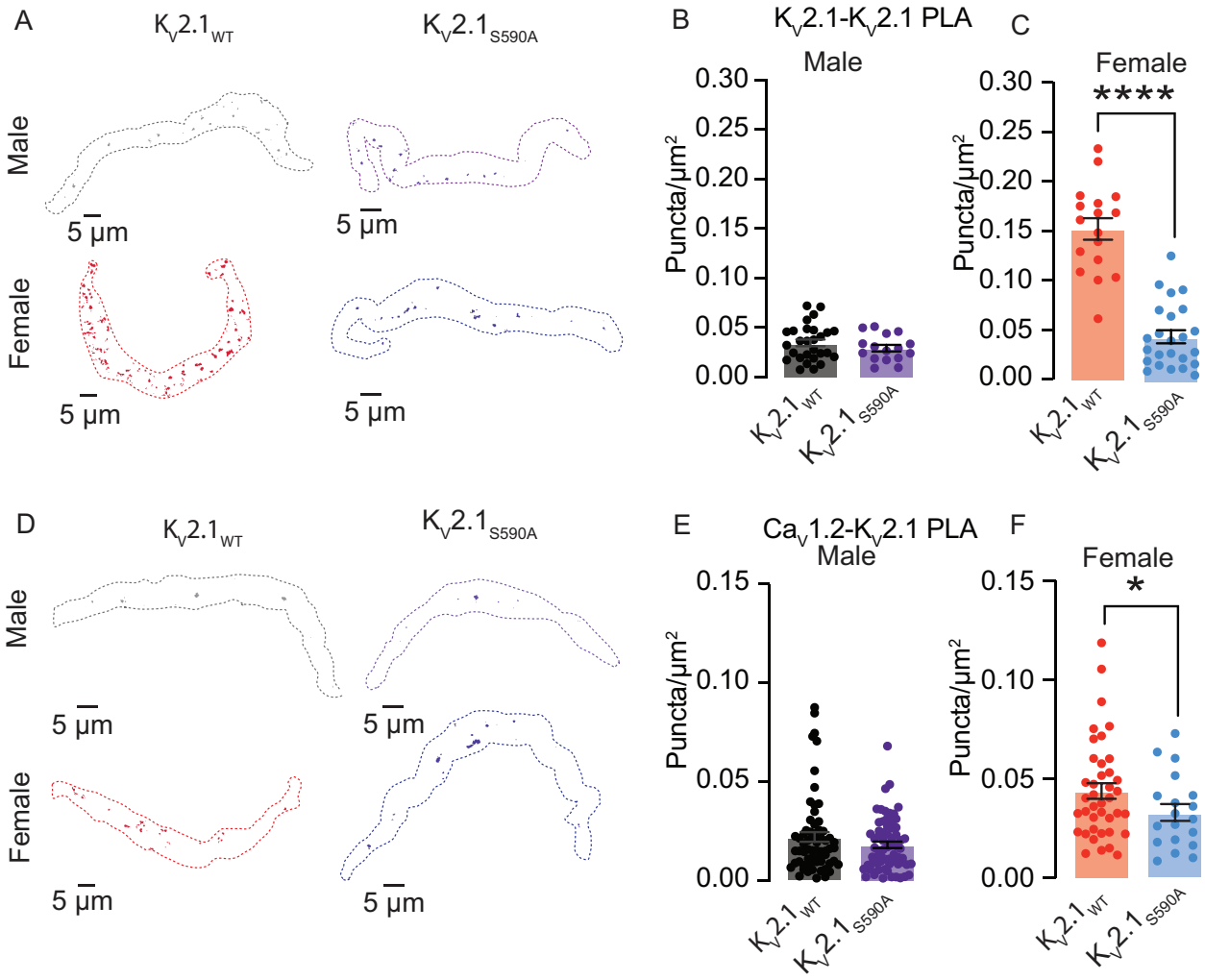

Figure 3.7 $K_V2.1$ and $Ca_V1.2$ interactions are decreased in female $K_V2.1_{S590A}$ myocytes (A) PLA images of representative $K_V2.1$-$K_V2.1$ channel interactions in arterial myocytes. Quantification of $K_V2.1$-$K_V2.1$ PLA puncta/µm^2 in male (B) and female (C) myocytes. (D) PLA images of representative $K_V2.1$-$Ca_V1.2$ channel interactions in arterial myocytes. Quantification of $K_V2.1$-$Ca_V1.2$ PLA puncta/µm^2 in male (E) and female (F). *P<0.05, **P<0.01, ***P<0.001, ****P<0.0001. Error bars indicate mean ± SEM.

Quantification showed that $K_V2.1$-$Ca_V1.2$ puncta density was unchanged in males between $K_V2.1_{WT}$ male myocytes with a mean of 0.022 ± 0.002 puncta/μm^2 (median = 0.016 puncta/μm^2) and $K_V2.1_{S590A}$ male myocytes with a mean of 0.018 ± 0.002 puncta/μm^2 (median = 0.016 puncta/μm^2; P = 0.217) (**Figure 3.7E**). However, $K_V2.1$-$Ca_V1.2$ interactions decreased in female $K_V2.1_{S590A}$ myocytes with a mean of 0.030 ± 0.004 puncta/μm^2 (median = 0.026 puncta/μm^2) compared to $K_V2.1_{WT}$ female myocytes with a mean of 0.044 ± 0.004 puncta/μm^2 (median = 0.026 puncta/μm^2; P = 0.013) (**Figure 3.7F**). These data further support a sex-specific structural role for $K_V2.1$ channels, facilitating $Ca_V1.2$-$Ca_V1.2$ clustering.

3.4.6 Female myocytes expressing $K_V2.1_{S590A}$ have reduced macroscopic $Ca_V1.2$ currents

We recorded macroscopic $Ca_V1.2$ currents (I_{Ca}) from male and female $K_V2.1_{WT}$ and $K_V2.1_{S590A}$ arterial myocytes (**Figure 3.8A-D**). I_{Ca} was activated by applying 300 ms voltage step depolarizations from a holding potential of -80 to +60 mV. We show I_{Ca} traces recorded during a depolarization to 0 mV from representative male (**Figure 3.8A**) and female (**Figure 3.8B**) $K_V2.1_{WT}$ and $K_V2.1_{S590A}$ arterial myocytes. Note that the amplitude and kinetics of I_{Ca} in these male $K_V2.1_{WT}$ and $K_V2.1_{S590A}$ arterial myocytes were similar. By contrast, we found that peak I_{Ca} was smaller in female $Kv2.1_{S590A}$ myocytes compared to those in $K_V2.1_{WT}$ cells. In **Figure 3.8C** and **D**, we show the voltage dependence of the amplitude of I_{Ca} from all the cells examined over a wider range of membrane potentials. This analysis shows that the amplitude of I_{Ca} is similar in $K_V2.1_{WT}$ and $K_V2.1_{S590A}$ male myocytes at all voltages examined. However, in female

myocytes, I_{Ca} was smaller in $K_V2.1_{S590A}$ than in $K_V2.1_{WT}$ at all voltages examined. Indeed, at 0 mV, I_{Ca} amplitude in $K_V2.1_{S590A}$ cells was approximately 50% of that of WT females.

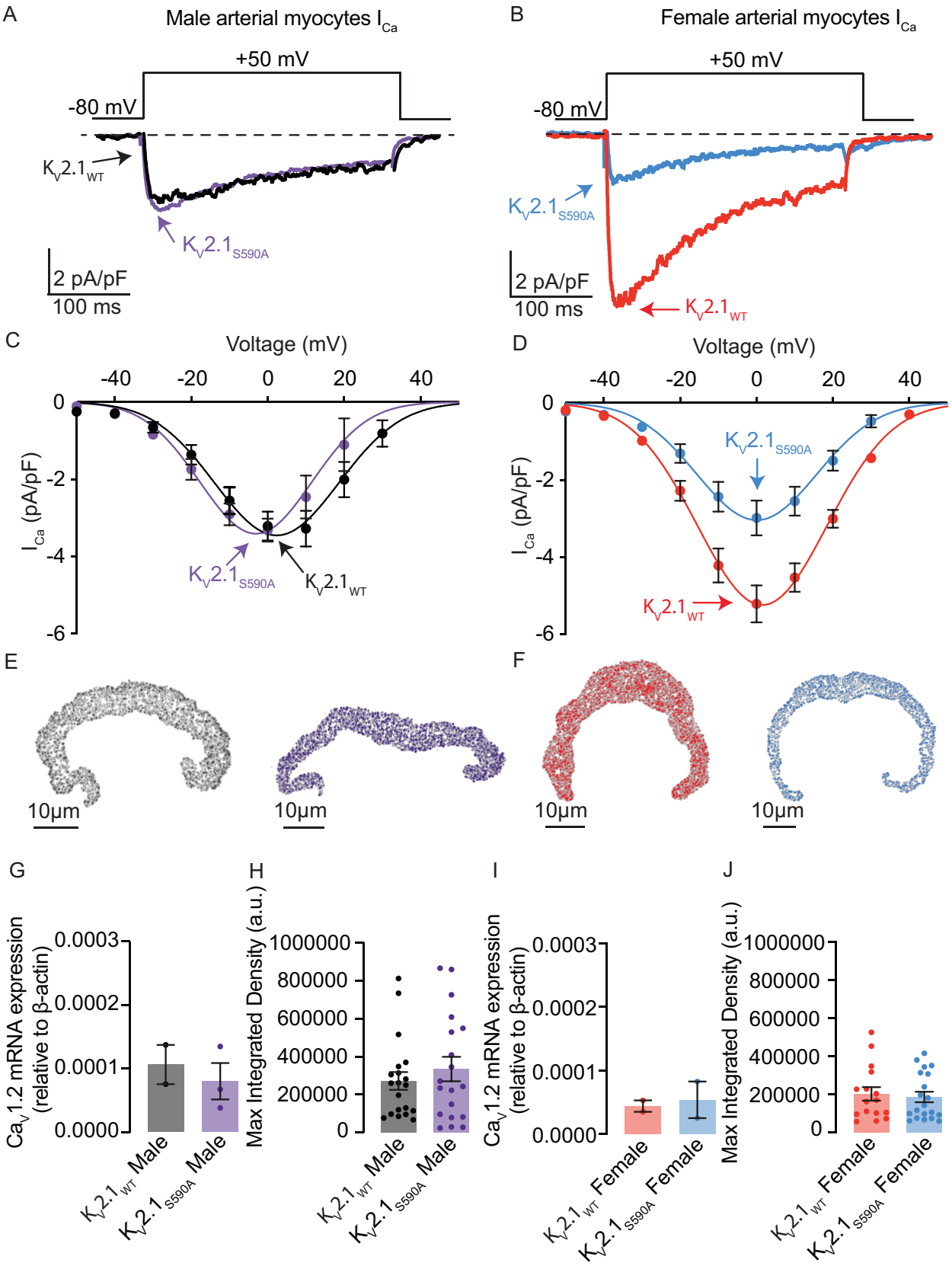
A
Male arterial myocytes I_{Ca}
+50 mV
-80 mV
$K_V2.1_{WT}$
$K_V2.1_{S590A}$
2 pA/pF
100 ms
B
Female arterial myocytes I_{Ca}
+50 mV
-80 mV
$K_V2.1_{S590A}$
2 pA/pF
100 ms
$K_V2.1_{WT}$
C
Voltage (mV)
-40 -20 0 20 40
0 -2 -4 -6
I_{Ca} (pA/pF)
$K_V2.1_{S590A}$
$K_V2.1_{WT}$
D
Voltage (mV)
-40 -20 0 20 40
0 -2 -4 -6
I_{Ca} (pA/pF)
$K_V2.1_{S590A}$
$K_V2.1_{WT}$
E
10µm
10µm
F
10µm
10µm
G
$Ca_V1.2$ mRNA expression (relative to β-actin)
0.0003 0.0002 0.0001 0.0000
$K_V2.1_{WT}$ Male
$K_V2.1_{S590A}$ Male
H
Max Integrated Density (a.u.)
1000000 800000 600000 400000 200000 0
$K_V2.1_{WT}$ Male
$K_V2.1_{S590A}$ Male
I
$Ca_V1.2$ mRNA expression (relative to β-actin)
0.0003 0.0002 0.0001 0.0000
$K_V2.1_{WT}$ Female
$K_V2.1_{S590A}$ Female
J
Max Integrated Density (a.u.)
1000000 800000 600000 400000 200000 0
$K_V2.1_{WT}$ Female
$K_V2.1_{S590A}$ Female

Figure 3.8 I_{Ca} is reduced in $K_V2.1_{S590A}$ female myocytes but unaffected in male arterial myocytes. I_{Ca} records (0 mV) from representative $K_V2.1_{WT}$ and $K_V2.1_{S590A}$ male (A) and $K_V2.1_{WT}$ and $K_V2.1_{S590A}$ female (B) myocytes. Voltage dependence of I_{Ca} from male (C) and female (D) myocytes at membrane potentials ranging from -50 to +50 mV. (E,F) Representative images of immunolabeled $Ca_V1.2$ in myocytes from $K_V2.1_{WT}$ male (E, black), $K_V2.1_{S590A}$ male (E, purple), $K_V2.1_{WT}$ female (F, red), and $K_V2.1_{S590A}$ female (F, blue) mice. Summary data from real-time quantitative PCR experiments of $Ca_V1.2$ mRNA expression relative to β-actin in male (G) and female (I) myocytes. Quantification of immunofluorescence of labeled $Ca_V1.2\alpha$ subunit in male (H) and female (J) myocytes. Error bars indicate mean ± SEM.

Next, we determined the level of expression of $Ca_V1.2$ protein in male and female $K_V2.1_{S590A}$ and $K_V2.1_{WT}$ vessels using immunocytochemistry (**Figure 3.8E, F, H, J**) and RT-PCR approaches (**Figure 3.8G and I**). Our analysis suggests that total $Ca_V1.2$ protein and mRNA expression is similar in male and female $K_V2.1_{S590A}$ and $K_V2.1_{WT}$ vessels. This suggests that the smaller I_{Ca} in female $K_V2.1_{S590A}$ than $K_V2.1_{WT}$ myocytes is not likely due to lower $Ca_V1.2$ expression in these cells

3.4.7 Declustering $K_V2.1$ in myocytes with the $Kv2.1_{S590A}$ mutation decreases $Ca_V1.2$ cluster sizes in female but not male arterial myocytes

In a previous study (*287*), we suggested a model that differences in I_{Ca} amplitude between female and male arterial myocytes were due to sex-specific differences in $K_V2.1$-mediated $Ca_V1.2$ clustering that impacted the probability of cooperative gating of

these channels. Our data above show differences in I_{Ca} amplitude between female $K_V2.1_{WT}$ and $K_V2.1_{S590A}$ myocytes in the absence of differences in $Ca_V1.2$ expression levels. Thus, we investigated whether $K_V2.1_{S590A}$ expression altered $Ca_V1.2$ channel clustering in a sex-specific manner using ground state depletion (GSD) super-resolution microscopy (**Figure 3.9**).

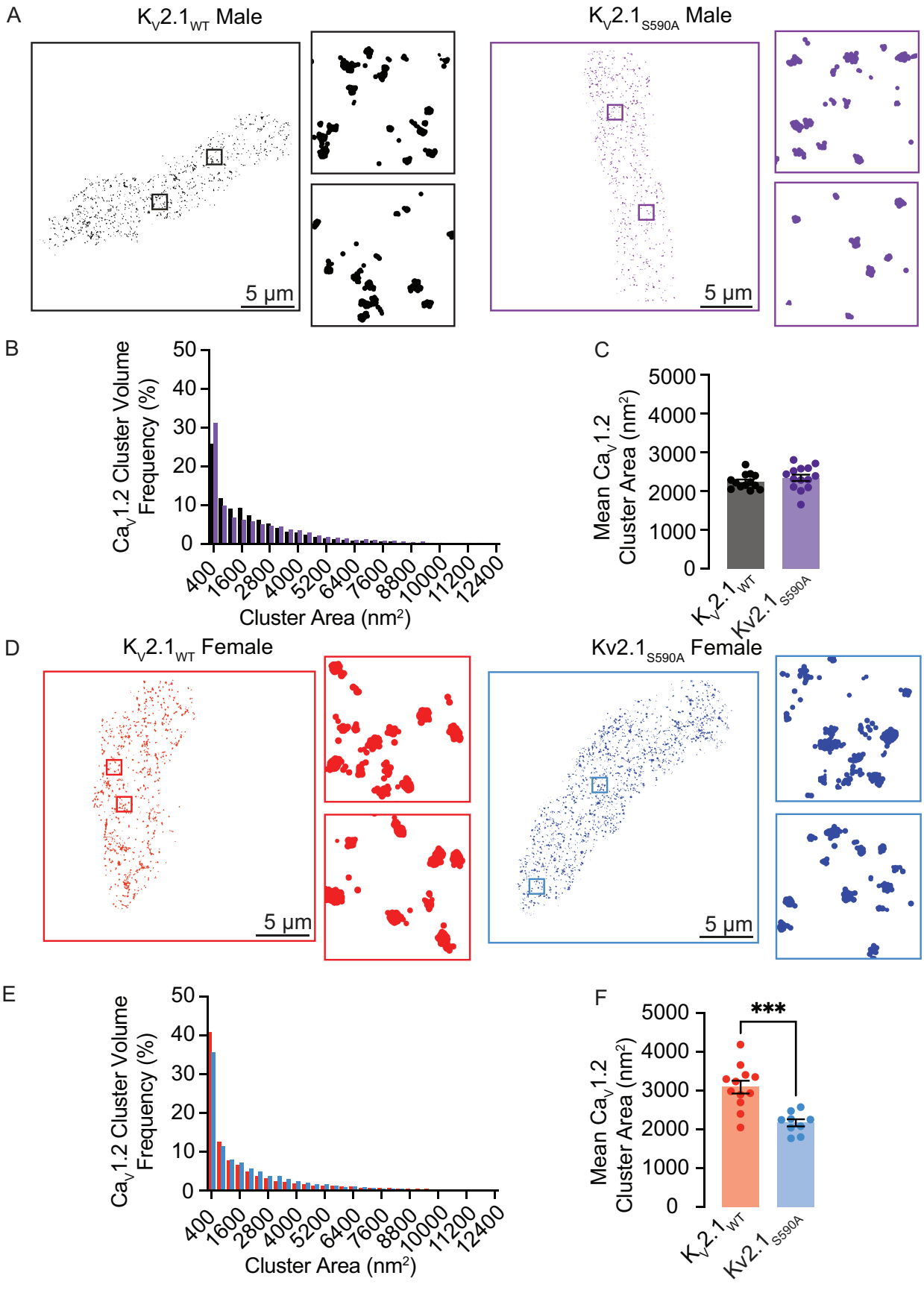
A
$K_V2.1_{WT}$ Male
$K_V2.1_{S590A}$ Male
5 µm
5 µm
B
$Ca_V1.2$ Cluster Volume Frequency (%)
Cluster Area (nm²)
C
Mean $Ca_V1.2$ Cluster Area (nm²)
$K_V2.1_{WT}$
$Kv2.1_{S590A}$
D
$K_V2.1_{WT}$ Female
$Kv2.1_{S590A}$ Female
5 µm
5 µm
E
$Ca_V1.2$ Cluster Volume Frequency (%)
Cluster Area (nm²)
F
***
Mean $Ca_V1.2$ Cluster Area (nm²)
$K_V2.1_{WT}$
$Kv2.1_{S590A}$

Figure 3.9 $Ca_V1.2$ cluster sizes are decreased in myocytes from female but not male $K_V2.1_{S590A}$ mice. (A) Representative super-resolution GSD images of immunolabeled $Ca_V1.2$ labeled channels in $K_V2.1_{WT}$ (left) and $K_V2.1_{S590A}$ (right) male myocytes. Insets show 4 μm^2 regions of interest. (B) Relative frequency as a percentage of $K_V2.1$ cluster areas of $K_V2.1_{WT}$ (black) and $K_V2.1_{S590A}$ (purple) in male myocytes. (C) Summary plot of mean $K_V2.1$ cluster areas in male myocytes (D) Representative super-resolution GSD microscopy images of immunolabeled $Ca_V1.2$ labeled channels in $K_V2.1_{WT}$ (left) and $K_V2.1_{S590A}$ (right) female myocytes. (E) Relative frequency as a percentage of $K_V2.1$ cluster areas of $K_V2.1_{WT}$ (red) and $K_V2.1_{S590A}$ (blue) female myocytes. (F) Summary plot of mean $K_V2.1$ cluster areas in female myocytes. *P < 0.05, **P < 0.01, ***P < 0.001. Error bars indicate mean ± SEM.

We show ground state-depletion run in TIRF mode super-resolution images from representative male (**Figure 3.9A**) and female (**Figure 3.9D**) myocytes from $K_V2.1_{WT}$ and $K_V2.1_{S590A}$ mice. The insets show expanded views of two regions of interest (1 μm^2) within each cell image. Our TIRF images show that $Ca_V1.2$ clusters of various sizes are expressed throughout these cells. The frequency distribution of $Ca_V1.2$ cluster areas of $K_V2.1_{WT}$ and $K_V2.1_{S586A}$ in male and females could both be fit with an exponential function (**Figure 3.9B, E)**.

The mean area of $Ca_V1.2$ clusters in male $K_V2.1_{WT}$ of 2259 ± 55 nm^2 (median = 2219 nm^2) was similar to the $K_V2.1_{S590A}$ male mean of 2345 ± 82 nm^2 (median = 2354 nm^2) (P = 0.173) (**Figure 3.9C**), suggesting that declustering $K_V2.1$ in male myocytes does not

affect $Ca_V1.2$ channel clustering. However, $Ca_V1.2$ cluster sizes were significantly smaller in $K_V2.1_{S590A}$ female myocytes with a mean area of 2381 ± 91 nm^2 (median = 2251 nm^2) compared to $K_V2.1_{WT}$ female myocytes whose mean area was 3098 ± 164 nm^2 (median = 3117 nm^2) (P = 0.0001). Taken together with our electrophysiological data, our findings suggest that the clustering and activity of $Ca_V1.2$ channels is modulated by the degree of $K_V2.1$ clustering.

As shown in **Figure 3.10A and B,** our stochastic self-assembly model effectively reproduced the steady-state size distributions that we measured for $Ca_V1.2$ clustering in $K_V2.1_{WT}$ and $K_V2.1_{S586A}$ arterial myocytes. The parameters used in the model are summarized in **Figure 3.10C**. These *in silico* data suggest that $Ca_V1.2$ clusters in $K_V2.1_{S590A}$ female myocytes have a higher probability of growth (i.e., P_g) than those in female $K_V2.1_{WT}$ arterial myocytes.

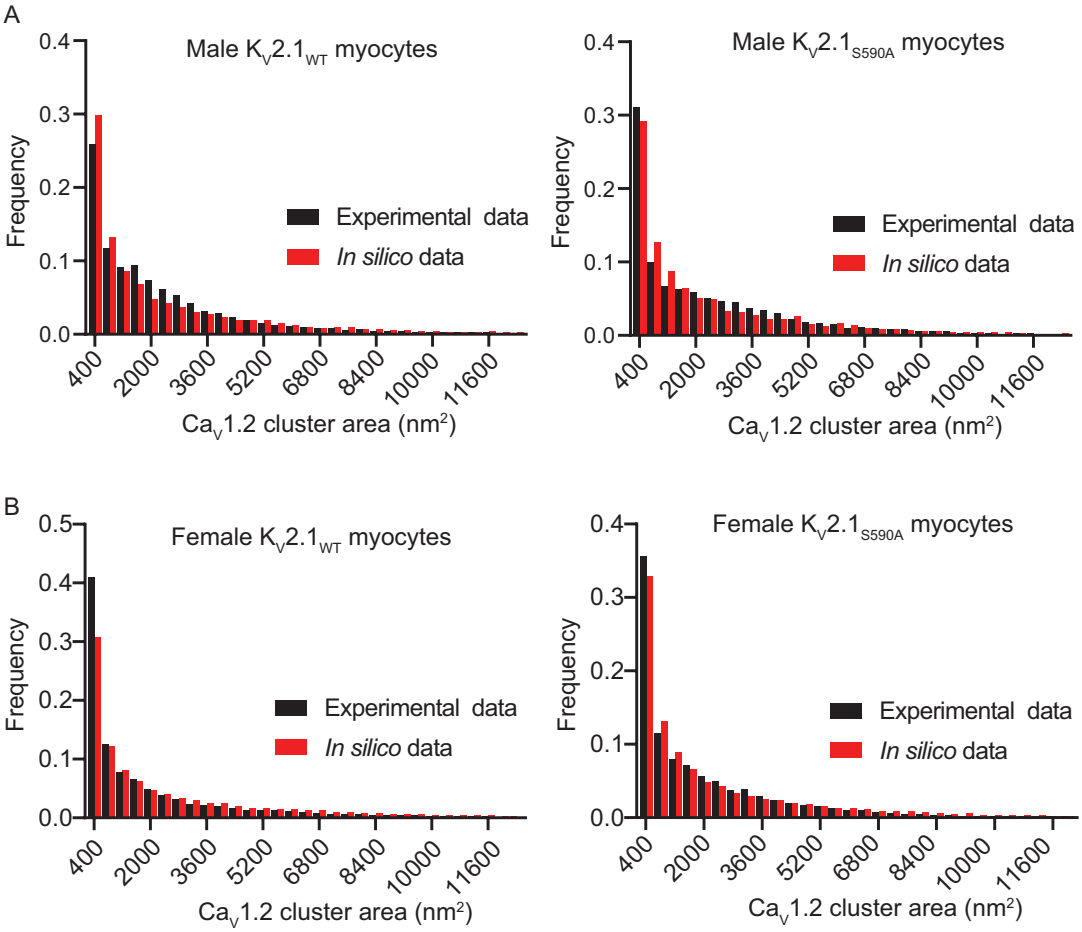

C

Arterial Myocyte CaV1.2	P_n	P_g	P_R	Mean experimental cluster size (nm^2)	Mean *in silico* cluster size (nm^2)	Mean experimental cluster density (clusters/μm^2)	Mean *in silico* cluster density (clusters/μm^2)
WT male	0.000056159	0.083203	0.001	2249 ± 54.53	2567.3	14 ± 1.2	14.062
$K_V2.1_{S590A}$ male	0.000047767	0.086086	0.001	2345 ± 81.84	2574.6	12 ± 2.2	12.176
WT female	0.000047826	0.10793	0.001	3098 ±163.8	2989.9	11 ± 1.1	10.881
$K_V2.1_{S590A}$ female	0.000043453	0.067511	0.001	2175 ± 91.72	2327.7	13 ± 1.8	13.32

Figure 3.10 The distributions of $Ca_V1.2$ in $K_V2.1$ and $K_V2.1_{S590A}$ arterial myocytes could be explained by a stochastic self-assembly mechanism. (A) Histograms of experimental (black bars) and simulated (red bars) $Ca_V1.2$ cluster area distributions as

a relative frequency of $K_V2.1_{WT}$ (left) and $K_V2.1_{S590A}$ (right) in male arterial myocytes. (B) Histograms of experimental (black bars) and simulated (red bars) $Ca_V1.2$ cluster area distributions as a relative frequency of $K_V2.1_{WT}$ (left) and $K_V2.1_{S590A}$ (right) in female arterial myocytes. (C) Summary of experimental and *in silico* data.

3.4.8 $K_V2.1_{S586A}$ reduces $Ca_V1.2$-$Ca_V1.2$ channel interactions

Having previously shown that $K_V2.1$ enhances $Ca_V1.2$-$Ca_V1.2$ channel interactions in arterial myocytes (*287*), we set out to determine if a decrease in $K_V2.1$ clustering would lead to a reduction in $Ca_V1.2$-$Ca_V1.2$ interactions. We utilized a split-Venus fluorescent protein system to visualize $Ca_V1.2$ channels. This system involves fusing $Ca_V1.2$ channels with either the N-terminal fragment ($Ca_V1.2$-VN) or the C-terminal fragment ($Ca_V1.2$-VC) of Venus protein. Individually, neither $Ca_V1.2$-VN nor $Ca_V1.2$-VC emits fluorescence. However, when brought into close enough proximity for interaction to occur, they can reconstitute a full fluorescence emitting Venus protein. Thus, the split-Venus fluorescence can be utilized to indicate spontaneous interactions between neighboring $Ca_V1.2$ channels. Accordingly, we compared the split-Venus fluorescence in HEK293T cells expressing $Ca_V1.2$-VN and $Ca_V1.2$-VC and co-expressing either $K_V2.1_{WT}$ or $K_V2.1_{S586A}$ (**Figure 3.11**). The voltage protocols used for these experiments are similar to those used in two recent studies (*240, 287*) and are described in detail in the Methods section of this paper.

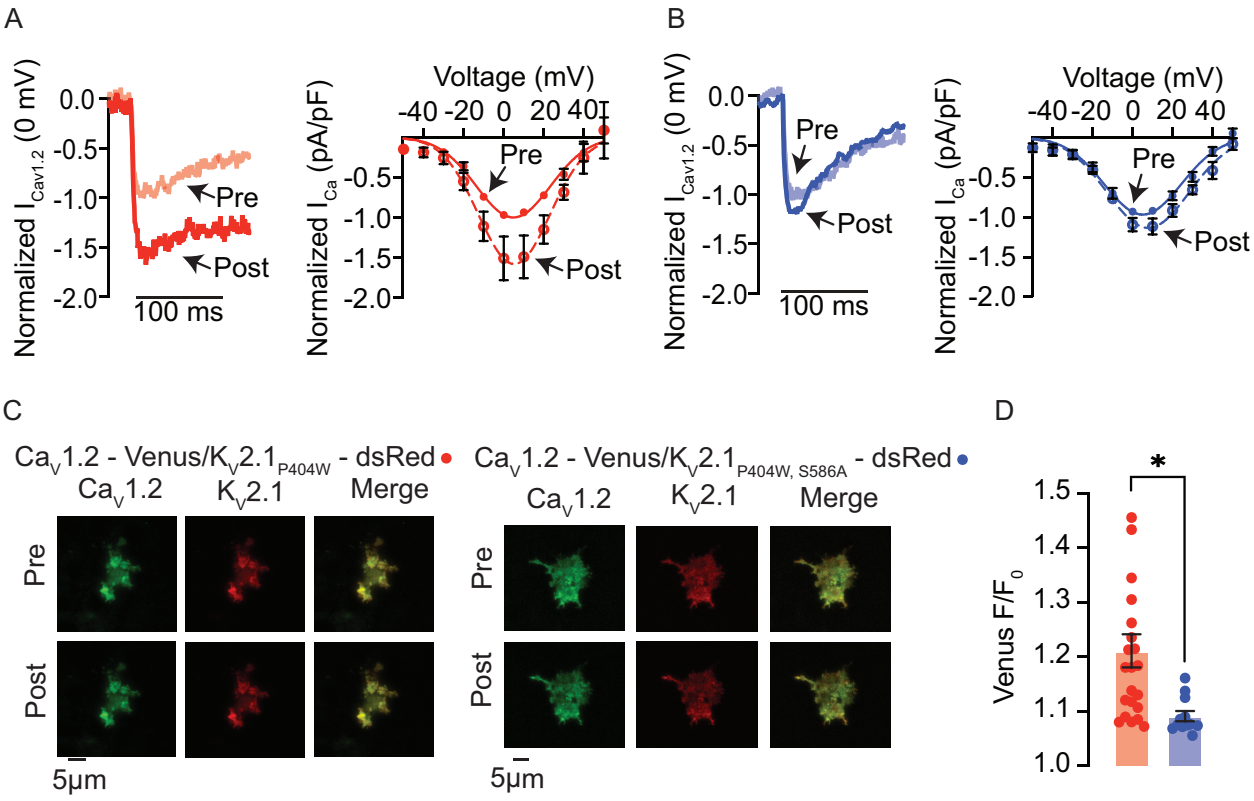

Figure 3.11 $Ca_V1.2$-$Ca_V1.2$ interactions are decreased in cells expressing $K_V2.1_{S586A}$ (A, left) Representative currents measured at 0 mV from pre- (opaque red) and post- (red) conditioning protocol from HEK293T cells expressing $Ca_V1.2$-VN, $Ca_V1.2$-VC, and DsRed-$K_V2.1_{P404W}$. (A, right) Normalized (to peak current in pre-conditioning protocol) pre- and post- IV relationships from HEK293T cells expressing $Ca_V1.2$-VN, $Ca_V1.2$-VC, and DsRed-$K_V2.1_{P404W}$. (B, left) Representative currents measured at 0 mV from pre- (opaque blue) and post- (blue) conditioning protocol from HEK293T cells expressing $Ca_V1.2$-VN, $Ca_V1.2$-VC, and DsRed-$K_V2.1_{P404W,S586A}$. (B, right) Normalized pre- and post- IV relationships from HEK293T cells expressing $Ca_V1.2$-VN, $Ca_V1.2$-VC, and DsRed-$K_V2.1_{P404W,S586A}$. (C) Representative TIRF images of Venus fluorescence reconstitution in HEK293T cells from cells transfected with $Ca_V1.2$-VC, $Ca_V1.2$-VC and DsRed-$K_V2.1_{P404W}$ (left) or $Ca_V1.2$-VC, $Ca_V1.2$-VC and

DsRed-$K_V2.1_{P404W,S586A}$ (right). Pre- and post-conditioning $Ca_V1.2$-Venus (green), $K_V2.1_{P404W}$ or $K_V2._{1P404W,S856A}$ (red), and the merge of the two channels are presented. (D) Summary of $Ca_V1.2$-Venus fluorescence (F/F_0). *P < 0.05. Error bars indicate mean ± SEM.

We first transfected HEK293T cells with $Ca_V1.2$-VC, $Ca_V1.2$-VN, and the non-conducting but clustering competent rat $K_V2.1_{P404W}$ channel(*306*) tagged with red-shifted fluorescent protein dsRed. The P404W mutation confers a non-conductive $K_V2.1$ phenotype, allowing us to study the structural clustering role of $K_V2.1$ without masking of the Ca^{2+} currents by K^+. We found that I_{Ca} was larger at most membrane potentials in our post-conditioning IV protocol with a peak I_{Ca} at 0 mV showing an increase by about 51% (**Figure 3.11A**). Representative TIRF images are provided before and after conditioning protocol (**Figure 3.11C**). Note the appearance of co-clusters of $Ca_V1.2$ (green) and $K_V2.1$ (red). Our data show that Venus fluorescence increased by approximately 21% with stimulation from basal to post-conditioning steps suggesting an increase in $K_V2.1$ dependent $Ca_V1.2$-$Ca_V1.2$ interactions (**Figure 3.11D**). This supports previously published results(*287, 289*). To test the role of declustering $K_V2.1$ with the S586A point mutation on $Ca_V1.2$ channel interactions, we co-expressed $Ca_V1.2$-VN, $Ca_V1.2$-VC and DsRed-$K_V2.1_{P404W,S586A}$ in HEK293T cells and repeated the above protocol. We found that I_{Ca} did exhibit a small increase of about 9.4% between pre- and post- conditional protocols (**Figure 3.11B**). In representative TIRF footprints, we show that $Ca_V1.2$-VN, $Ca_V1.2$-VC and $K_V2.1_{P404W,S586A}$ transfected cells expressed more diffusely clustered $Ca_V1.2$ and $K_V2.1$ channels, visually confirming that $K_V2.1$ is

declustered (**Figure 3.11C**). Furthermore, Venus fluorescence with $K_V2.1_{P404W,S586A}$ expression increased by about 9%, a level similar to what was previously published(*287, 289*) with $Ca_V1.2$-VN and $Ca_V1.2$ VC alone (**Figure 3.11D)**. We propose this small increase is due to the intrinsic ability of $Ca_V1.2$ channels to interact with one another. However, this increase in Venus fluorescence was significantly lower than that seen in $K_V2.1_{P404W}$ transfected cells (**Figure 3.11D)**. Together these data further support the structural role $K_V2.1$ channels play in modulating $Ca_V1.2$-$Ca_V1.2$ interactions and activity.

3.4.9 The activity of $Ca_V1.2$ channels is reduced in $K_V2.1_{S590A}$ female but not male arterial myocytes

We next examined whether variations in the activity of $Ca_V1.2$ channels could explain the differences in I_{Ca} observed in myocytes from $K_V2.1_{WT}$ and $K_V2.1_{S590A}$ male and female mice. $Ca_V1.2$ channel activity was determined by recording $Ca_V1.2$ sparklets using TIRF microscopy as previously described (*92-94, 144, 147, 289, 307*) (**Figure 3.12**).TIRF microscopy of near-plasma membrane intracellular Ca^{2+} levels provides a powerful tool for recording Ca^{2+} entry via individual or small clusters of $Ca_V1.2$ channels, as it enables the activity of individual channels to be recorded from a relatively large membrane area allowing for the identification of discrete sarcolemma signaling domains. In this analysis, $Ca_V1.2$ sparklet activity is expressed as nP_s, where n is the number of quantal levels reached by the sparklet site and P_s is the probability of sparklet occurrence.

As previously reported (*147*), detailed analysis of $Ca_V1.2$ sparklets sites revealed heterogeneity in activity at different sites. Therefore, $Ca_V1.2$ sparklets sites were separated into low and high activity sites, using an nP_s cutoff of 0.2.

Representative $Ca_V1.2$ sparklet traces are provided (**Figure 3.12A, B, F, G**) from low activity sparklet sites. Of note, the majority of the sparklet activity that occurs in male myocytes is produced by a signal that corresponds to a single channel opening (one quantal unit) (**Figure 3.12A, B**). The strength of the coupled gating is denoted by the κ value, and in these traces, the κ values are close to or equal to 0, indicating no or weak coupling between the channels. In contrast, the $K_V2.1_{WT}$ female trace (**Figure 3.12F)** from a low activity site exhibited coordinated multi-channel openings, of up to 3 channels with a κ value of 0.466. Interestingly, the activity of sparklet sites from $K_V2.1_{S590A}$ female myocytes (**Figure 3.12G)** were similar to those of $K_V2.1_{WT}$ and $K_V2.1_{S590A}$ male myocytes (**Figure 3.12A, B)**, exhibiting mostly single channel openings and few coupled gating events.

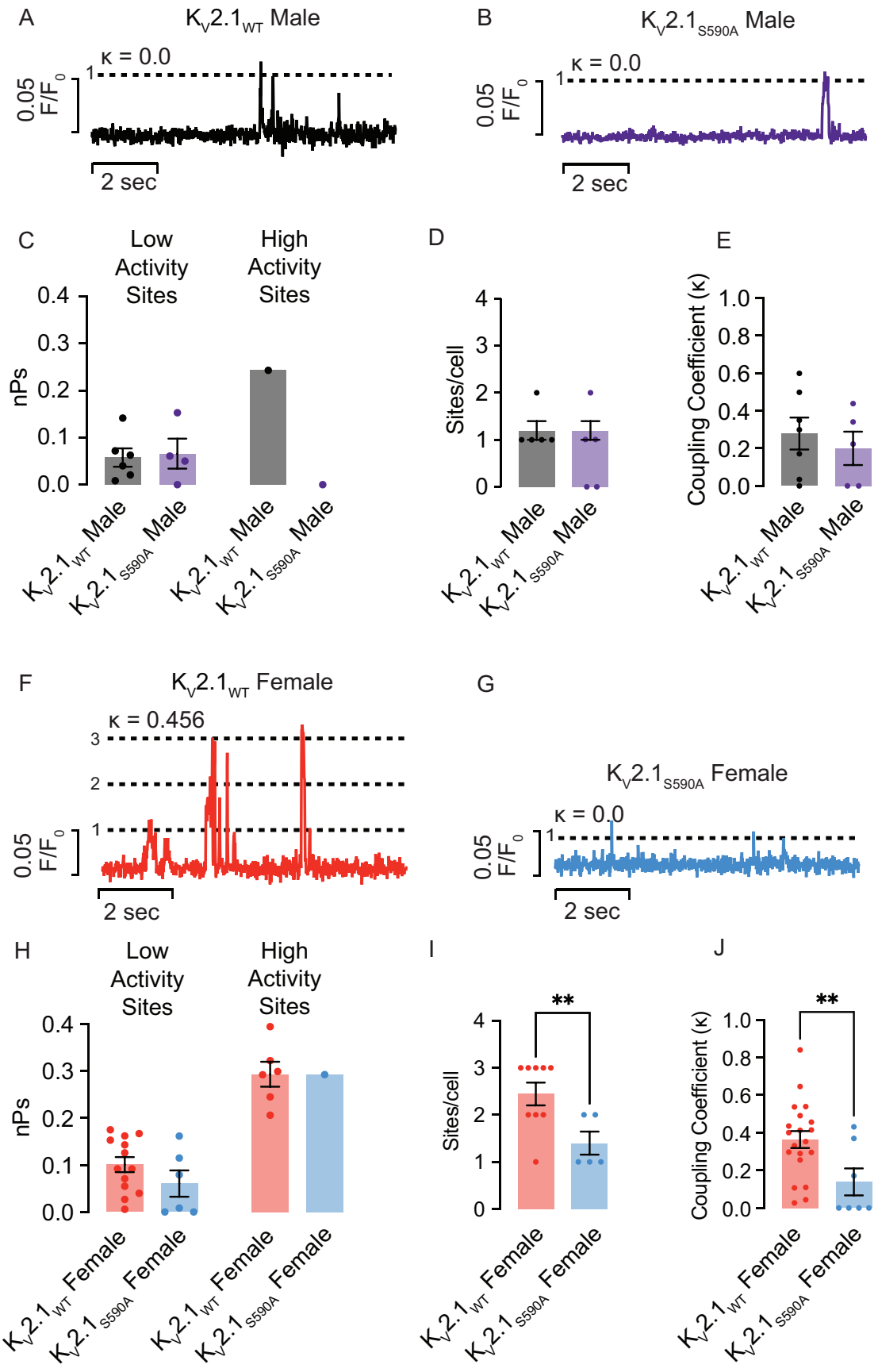
A
$K_V2.1_{WT}$ Male
κ = 0.0
1
0.05 F/F0
2 sec
B
$K_V2.1_{S590A}$ Male
κ = 0.0
1
0.05 F/F0
2 sec
C
Low Activity Sites
High Activity Sites
nPs
0.4
0.3
0.2
0.1
0.0
$K_V2.1_{WT}$ Male
$K_V2.1_{S590A}$ Male
$K_V2.1_{WT}$ Male
$K_V2.1_{S590A}$ Male
D
Sites/cell
4
3
2
1
0
$K_V2.1_{WT}$ Male
$K_V2.1_{S590A}$ Male
E
Coupling Coefficient (κ)
1.0
0.8
0.6
0.4
0.2
0.0
$K_V2.1_{WT}$ Male
$K_V2.1_{S590A}$ Male
F
$K_V2.1_{WT}$ Female
κ = 0.456
3
2
1
0.05 F/F0
2 sec
G
$K_V2.1_{S590A}$ Female
κ = 0.0
1
0.05 F/F0
2 sec
H
Low Activity Sites
High Activity Sites
nPs
0.4
0.3
0.2
0.1
0.0
$K_V2.1_{WT}$ Female
$K_V2.1_{S590A}$ Female
$K_V2.1_{WT}$ Female
$K_V2.1_{S590A}$ Female
I
**
Sites/cell
4
3
2
1
0
$K_V2.1_{WT}$ Female
$K_V2.1_{S590A}$ Female
J
**
Coupling Coefficient (κ)
1.0
0.8
0.6
0.4
0.2
0.0
$K_V2.1_{WT}$ Female
$K_V2.1_{S590A}$ Female

Figure 3.12 Activity of $Ca_V1.2$ channels is reduced in $K_V2.1_{S586A}$ female but not male arterial myocytes Representative sparklet traces from $K_V2.1_{WT}$ male (A), $K_V2.1_{S590A}$ male (B), $K_V2.1_{WT}$ female (F), and $K_V2.1_{S590A}$ female (G) myocytes. κ values are shown above each trace. nPs values from low activity sites (left) and high activity sites (right) in male (C) and female (H) myocytes. Coupling coefficient values (κ) from male (D) and female (I) myocytes. Sparklet sites per cell from male myocytes (E) and female (J) myocytes. *P < 0.05, **P < 0.01. Error bars indicate mean ± SEM.

We found that in low activity sparklet sites, the average nP_s was not significantly different between $K_V2.1_{WT}$ and $K_V2.1_{S590A}$ male myocytes (**Figure 3.12C**). $K_V2.1_{WT}$ sparklet sites had an average nP_s of 0.06 ± 0.02 (median = 0.05) compared to $K_V2.1_{S590A}$ where the nP_s average was 0.07 ± 0.03 (median = 0.06) (P = 0.41). In male myocytes of either genotype, we rarely observed cells exhibiting high activity sparklet sites, except for a single site in a $K_V2.1_{WT}$ male myocyte (**Figure 3.12C**). Furthermore, we did not observe a difference in the number of $Ca_V1.2$ sparklet sites between $K_V2.1_{WT}$ and $K_V2.1_{S590A}$ male myocytes, with most cells exhibiting just one site (**Figure 3.12D)**.

Similarly, when we compared nP_s in low activity sites in $K_V2.1_{WT}$ and $K_V2.1_{S590A}$ female myocytes, we could not discern a difference in their average nP_s values (**Figure 3.12H**). $K_V2.1_{WT}$ female mean nPs was 0.10 ± 0.02 (median = 0.09), which was similar to 0.06 ± 0.03 (median = 0.04) in $K_V2.1_{S590A}$ female myocytes (P = 0.10). High activity sites averaged an nP_s of 0.29 ± 0.03 (median = 0.30) in $K_V2.1_{WT}$ cells and a mean of 0.29 ± 0.01 (median = 0.29) in $K_V2.1_{S590A}$ female cells (P = 0.50) (**Figure 3.12H**). However,

$K_V2.1_{WT}$ female myocytes exhibited 2.44 ± 0.24 (median = 3.0) $Ca_V1.2$ sparklet sites per cell, significantly higher than 1.40 ± 0.25 (median = 1.0) $Ca_V1.2$ sparklet sites in $K_V2.1_{S590A}$ female myocytes (P = 0.008) suggesting decreased $Ca_V1.2$ channel activity with S590A mutation (**Figure 3.12I**).

Previous work (*144*) showed that $Ca_V1.2$ sparklet sites appeared to arise from the simultaneous opening and/or closing of multiple channels suggesting that small groups of channels may be functioning cooperatively. To examine such coupling, we employed a coupled Markov chain model to determine the coupling coefficient (κ) among $Ca_V1.2$ channels at Ca^{2+} sparklet sites. The κ value ranges from 0 for channels that gate independently to 1 for channels that are tightly coupled and open and close simultaneously. A detailed description of this model is provided in the expanded Methods section.

Using this analysis, we found that the average κ value of 0.28 ± 0.09 (median = 0.30) in $K_V2.1_{WT}$ male myocytes was not significantly different from 0.20 ± 0.09 (median = 0.22) in $K_V2.1_{S590A}$ male myocytes (P = 0.27) (**Figure 3.12E**). However, the average κ value of 0.36 ± 0.05 (median = 0.38) in female $K_V2.1_{WT}$ myocytes, was significantly higher than 0.14 ± 0.07 (median = 0) (P = 0.0082) in female $K_V2.1_{S590A}$ myocytes, suggesting more coupled events (**Figure 3.12J**). Taken together, these data indicate increased $Ca_V1.2$ channel activity and coupled gating in myocytes from $K_V2.1_{WT}$ females compared to those with the $K_V2.1_{S590A}$ mutation, suggesting that clustering of $K_V2.1$ modulates $Ca_V1.2$ channel activity.

3.5 Discussion

In this study, we show that arterial smooth muscle cells from mice expressing a gene-edited point mutation of the $K_V2.1$ channel that selectively eliminates its characteristic macro-clustered localization have properties remarkably like those from $K_V2.1$ knock-out mice. This leads us to formulate a new model in which $K_V2.1$ expression — *by itself* — is not sufficient for this channel to exert its structural functions on modulating $Ca_V1.2$ clustering and activity, but rather depends on $K_V2.1$ channel's capacity to form macro-clusters. Notably, the presence of $K_V2.1$ macro-clusters in female, but not male myocytes underlie sex-specific differences in Ca^{2+} influx via $Ca_V1.2$ channels in arterial smooth muscle. Our data suggest a new paradigm whereby the clustering of ion channels underlies their physiological functions, independent of their ability to conduct ions.

Analysis of super-resolution images indicates that clustering of $K_V2.1$ and $Ca_V1.2$ channels is random and hence does not involve an active process. This stochastic self-assembly mechanism leads to micro- and macro-clusters of varying sizes that represent the default organization of $K_V2.1$ and Ca_V1 channels expressed endogenously in neurons and smooth muscle cells or exogenously in heterologous cells (*285*). Furthermore, we found that $K_V2.1$ macro-clusters are composed of groups of micro-clusters. This is consistent with a recent study showing that in developing neurons $K_V2.1$ macro-clusters formed from the coalescence of numerous micro-clusters (*308*) and suggests that the organization of $K_V2.1$ clusters is hierarchical.

An important finding in this study is that $K_V2.1$ clustering is more prominent in female than in male arterial myocytes, with female myocytes expressing a larger proportion of macro-clusters. In this context, the development of the $K_V2.1_{S590A}$ mouse allowed us to investigate the separable structural and clustering and ion conducting roles of this channel. We found that expression $K_V2.1_{S590A}$ nearly eliminated macro-clustering in female myocytes but had no impact on $K_V2.1$ micro-clusters in cells from male or female myocytes. Because the S590A mutation eliminated a phosphorylation site in the PRC domain that causes macro-clustering, these findings suggested that the potential mechanism of these sex-specific differences in $K_V2.1$ clustering was differential phosphorylation of this specific serine in male and female myocytes.

Indeed, $K_V2.1$ phosphorylation and macro-clustering is regulated by a myriad of protein kinases such as CDK5 and protein phosphatases such as calcineurin (*309*). These kinases and phosphatases work as a rheostatic mechanism to regulate the phosphorylation status of $K_V2.1$ based on physiological demands (*294, 295, 309*). Accordingly, we found that that the phosphorylation state of $K_V2.1$ in arterial myocytes differs between the two sexes, specifically, that $K_V2.1$ in male myocytes is phosphorylated to a much lower degree.

It is intriguing to consider the potential clustering mechanisms that are impacted by inhibiting phosphorylation at the 590/586 specific site of the PRC domain by the serine to alanine point mutation. One hypothesis is that VAP proteins act to modulate the

probability of macro-cluster formation. Studies show that K_V2.1 clusters are expressed at sites where the endo/sarcoplasmic reticulum is brought into close juxtaposition to the plasma membrane (ER/SR-PM junctions) (*308*) and this interaction and accumulation of channels relies on the tethering of K_V2.1 to VAP proteins (*279, 310*). The transmembrane ER/SR VAP proteins (VAPA and VAPB) interact with the phosphorylated K_V2.1 PRC domain and have been proposed to function to increase the local concentration of K_V2.1 channels at ER/SR-PM junctions resulting in K_V2.1 macro-clustering.

Consistent with this, Kirmiz et al., (*279*) found that knock-out of VAPA in RAW664.7 macrophage cells resulted in a decrease in K_V2.1 channel clustering. Knockdown of endogenous VAP proteins similarly impaired clustering of K_V2.1 heterologously expressed in HEK293T cells (*310*). Interestingly, the model proposed in these prior papers (*279, 310*) suggested that the phosphorylated PRC domain is necessary and sufficient for macro-clustering of K_V2 channels. This is consistent with prior studies showing that mutations disrupting or eliminating the PRC domain (*161, 306, 310*) or treatments that impact K_V2.1 phosphorylation (*294, 295, 309*) impact K_V2.1 clustering. It is presumed that the phosphorylation of multiple serine residues, including S590, within the PRC domain provide the negative charges needed to generate a functional VAP-binding FFAT — two phenylalanines in an acidic tract — motif, as has been shown for numerous other proteins that exhibit phosphorylation-dependent binding to VAPs (*311*).Therefore, one possible mechanism for the decrease in macro-clustering in the S590A mutant is the inability of VAP proteins to recognize the PRC domain of mutated

channels preventing cluster growth. The similarity in the patterns of cluster sizes and densities between HEK293T cells and arterial myocytes of both WT and S590A channels is noteworthy, indicating the possibility of a shared set of mechanisms. Further research will be necessary to uncover the underlying factors that govern these clustering patterns.

Prior studies have suggested that the bulk of $K_V2.1$ channels heterologously expressed in Xenopus oocytes (*168*) or HEK293T cells (*170*) as well as endogenous $K_V2.1$ in hippocampal neurons (*169*) and arterial myocytes (*287*) are in a nonconducting state. The prevailing view is that aggregation of $K_V2.1$ channels into high density clusters is what renders most of these channels incapable of conducting K^+ (45). Although our study does not address this issue comprehensively, at a minimum, our data suggest that $K_V2.1$ conduction is not dependent on macro-clustering formation. Future studies should investigate whether the formation of $K_V2.1$ micro-clusters may be sufficient to electrically silence these channels.

This is the first study to definitively demonstrate the structural role of $K_V2.1$ clustering in regulating $Ca_V1.2$ channel clustering and activity that occurs in channels of native cells. This is significant because the generally accepted view is that the functional impact of ion channel clustering is to exclusively concentrate ion conducting roles at specific sites. For example, Na^+ channel clustering at nodes of Ranvier (*312*), neuronal Ca^{2+} channel clustering at active zones in presynaptic terminals (*313*), and skeletal muscle Ca^{2+} channels at SR Ca^{2+} release units (*314*). In the case of ventricular myocytes, it is

concentrating voltage sensors at specific sites in the junctional dyad (*315, 316*). We propose that $K_V2.1$ clustering is distinct in playing a role in modulating the localization and activity of an otherwise seemingly unrelated ion channel: $Ca_V1.2$ channels. This functional impact of $K_V2.1$ is due to the density-dependent cooperative gating that is an intrinsic property of $Ca_V1.2$ channels (*317*).

Remarkably, the overall impact of $K_V2.1_{S590A}$ expression is that the differences between the I_{Ca} amplitude of wild-type male and female myocytes were eliminated in myocytes, similar to as we observed in homozygous $K_V2.1$ knockout mice (*287*). Thus, declustering $K_V2.1$ channels appears to have the same impact as fully eliminating $K_V2.1$ expression on $Ca_V1.2$ clustering and activity in male and female myocytes. As our work also suggests that in arterial myocytes the conductive function of $K_V2.1$ channels is independent of the degree of its clustering, in our model it is the extent of $K_V2.1$ clustering that is the key determinant of the sex-specific differences in Ca^{2+} influx observed in these cells.

To conclude, we propose a model by which $K_V2.1$ serves a structural role in promoting $Ca_V1.2$ channel clustering and activity in a sex-dependent manner. Of note, $K_V2.1_{S590A}$ mutation reduced $Ca_V1.2$ clustering and function in female myocytes but had no effect on male myocytes. $K_V2.1$ clustering is not necessary for $K_V2.1$ channel function however, $K_V2.1$ macro-clusters alter $Ca_V1.2$ channel organization. Together, our data suggest that the interactions between $K_V2.1$ and $Ca_V1.2$ are crucial for sex-based differences in arterial smooth muscle physiology.

Chapter 4: Discussion

4.1 Overview

The objective of this dissertation is to explore the formation of $K_V2.1$ and $Ca_V1.2$ clusters in murine mesenteric cells, their potential role and mechanisms in smooth muscle physiology, and the implications of any observed differences between sexes. The interaction between $Ca_V1.2$ and $K_V2.1$ activity is critical for arterial physiology, and it is commonly observed that these ion channels cluster together. However, the mechanisms behind the formation of these clusters are currently unknown. This dissertation presents a stochastic self-assembly model for ion channel cluster formation based on three mechanistic probabilities: nucleation, growth, and removal. The findings help to understand the mechanisms involved in ion channel trafficking and cluster maintenance in the plasma membrane and provide a potential explanation for sex-based differences in smooth muscle physiology. The experimental and computational approach reveals a crucial interaction between $Ca_V1.2$ and $K_V2.1$ in arterial smooth muscle. The model suggests that the clustering state of $K_V2.1$ does not determine channel conduction in mesenteric smooth muscle. Additionally, $K_V2.1$ macro-clusters act as sex-specific sites for increased $Ca_V1.2$ clustering. De-clustering $K_V2.1$ macro-clustering reduces $Ca_V1.2$ channel clustering and activity, playing a crucial role in Ca^{2+} dynamics and smooth muscle physiology.

4.2 Fundamental findings and insights from the stochastic self-assembly of ion channel cluster formation model

Here we address the important, yet incompletely understood question of how ion channel clusters form and are trafficked to the plasma membrane using a combination of experimental and computational modeling approaches. Statistical analysis of ion channel clusters size distributions in neurons, ventricular myocytes, arterial smooth muscle myocytes and heterologous expression system cells could all be described by exponential functions, suggesting a Poisson process. This would indicate that a continuous, independent, and memory-less process is at play. We propose a stochastic model of ion channel cluster delivery to the membrane that can be described by three mechanistic probabilities: nucleation, growth, and removal. The model suggests that stochastic self-assembly is the default mode of protein organization for many ion channels in the membrane of excitable cells. From experiments of exogenous expression of $Ca_V1.2$ and TRPV4 in tsA-201 cells we observed that cluster formation began with rapid growth in cluster size and density eventually reaching a steady-state. Our model predicts that the maintenance of this steady state relies on a relatively fast turnover of $Ca_V1.2$ and TRPV4 channels, but also gives us the added ability to estimate cluster dwell times in the membrane. Our model of stochastic ion channel formation in the membrane of excitable cells provides a unique and limitless tool that can be used to further refine ion channel clustering mechanisms in the membrane. Additionally, this model aids in the generation of testable hypotheses that can be examined both computationally and experimentally for how specific proteins and signaling pathways could dynamically shape cluster formation.

Our model provides a rigorous theoretical framework to describe ion channel protein trafficking. Previous studies on $Ca_V1.2$ trafficking have focused on specific mechanisms such as vesicle forward trafficking to the membrane(*221, 318, 319*), internalization (*320*), or $Ca_V1.2$ dynamic transport(*321, 322*). Experimental findings suggest that $Ca_V1.2$ channel clusters and activity can be modulated by unique intracellular and perimembrane vesicular dynamics to fine-tune Ca^{2+} signals(*322*). Another study providing a mechanism for activity-dependent internalization and trafficking of $Ca_V1.2$ mediated by binding to the tumor suppressor eIF3e/Int6(*320*). Like our findings, a third study on $Ca_V1.2$ trafficking reported that the dwell times of channels at the membrane were on the order of minutes(*321*). Our model offers a significant advantage as it integrates multiple mechanisms of $Ca_V1.2$ trafficking, including vesicle forward trafficking to the membrane, internalization, and dynamic transport, enabling a comprehensive analysis of their interplay. Moreover, the model facilitates the determination of a number of testable readouts such as cluster areas, densities and membrane dwell times.

Our model corroborates experimental findings that $Ca_V1.2$ ion channel clusters are dynamic structures within the cardiovascular system(*322, 323*). One important finding was that a feedback mechanism controls the clustering of $Ca_V1.2$ channels, which is crucial for establishing a stable $Ca_V1.2$ expression pattern. This could act as a reference point for regulation in reaction to physiological changes, that would be critical to maintain a relatively constant tissue performance under a range of physiological conditions. The studies by Ito et al.(*323*) and Del Villar et al.(*324*) provided insights into

the regulation of $Ca_V1.2$ channel trafficking during βAR signaling in ventricular myocytes. The study revealed that $Ca_V1.2$ channels are rapidly incorporated as pre-existing clusters, presumably through the merging of endosomes and transportation by molecular motors along microtubules anchored to the sarcolemma with the assistance of the protein BIN1 (Pg in our model). The authors observed that microtubules are required for $Ca_V1.2$ insertion and that $Ca_V1.2$ channel trafficking and cluster formation depends on random events, such as fluctuations in microtubule and actin dynamics and transport. Although follow-up studies are needed to investigate which specific processes contribute to fluctuations in $Ca_V1.2$ channel clustering in ventricular myocytes, the potential of our model to replicate cluster expression in different tissue types provides us with a high level of confidence in its theoretical underpinnings.

In Chapter 3, we observe that both $Ca_V1.2$ and $K_V2.1$ clusters exhibit a stochastic self-assembly mechanism and gain insight about $Ca_V1.2$ clustering via perturbations of $K_V2.1$ mutation. We observed total $Ca_V1.2$ channel expression does not decrease in $K_V2.1_{S590A}$ mice but $Ca_V1.2$ clustering does decrease in $K_V2.1_{S590A}$ females. We postulate that $K_V2.1$ macro-clusters may be acting as an interacting partner for $Ca_V1.2$ channels that are already inserted into the membrane, increasing the clustering of these channels (i.e., increase P_g). A model that can simulate the two channels trafficking together could provide a clearer picture of how $K_V2.1$ macro-clusters can increase $Ca_V1.2$ channel cluster sizes and how these interactions may exist over time. In future versions of the model, we could consider exploring the interactions of multiple proteins not only at steady-state but also over time. This would allow us to investigate how these

protein interactions influence the sizes and densities of clusters, as well as whether these interactions affect the longevity of clusters in the membrane. Such an analysis would be particularly interesting in shedding light on the dynamics of protein clustering and how these cluster interactions shape arterial smooth muscle physiology.

An area of research unexplored by our model pertains to alterations in channel expression in disease models. For example, the general consensus is that in hypertensive rat models, the expression of $Ca_V1.2$ is upregulated(*325-330*), and channel activity is enhanced(*144*), thereby augmenting myogenic tone. In contrast, Tajada and colleagues(*331*) demonstrated that in mouse mesenteric arteries, $Ca_V1.2$ is downregulated but an increase $Ca_V1.2$ sparklet activity inducing increases in Ca^{2+} influx and ultimately affecting contractile state of the cell. One might initially attribute the differences in the findings to variations in species, hypertensive models, or vascular beds studied. However, our computational model has the potential to provide insight into the possible mechanisms that could underlie these observations.

Based on the cluster distributions of $Ca_V1.2$ channels in the membrane from cells of normotensive and hypertensive animals, we can begin to investigate what factors may be involved in enhanced $Ca_V1.2$ channel activity. In examples where $Ca_V1.2$ channel expression increases, we can make several hypotheses. If channel density stays the same but channel cluster size increases, we can predict that a growth factor (P_g) is at play. If cluster density increases with no effect on cluster size, we can expect the change in distribution is due to an enhancement of the pool of channels delivered to the

membrane (P_n). It is possible that both the cluster size and cluster density increase. This would predict that multiple nucleating or growth mechanisms could be at play. According to several studies, it is believed that upregulation of $Ca_V1.2$ auxiliary subunits $\alpha_2\delta$ or β_3(*332, 333*) may be responsible for this phenomenon. Given the known involvement of these subunits in membrane expression, it is reasonable to hypothesize that upregulation of these subunits would increase the amount of $Ca_V1.2$ transported to the membrane, leading to an increase in cluster densities (P_n).

In cases where hypertensive models elicit a decrease in $Ca_V1.2$ channels, it has been proposed that a change in $Ca_V1.2$ subunit composition may be responsible for the downregulation and altered activity of $Ca_V1.2$ channels in hypertensive models. Specifically, both β3 and β2 subunits are expressed(*334*), but β3 appears to be the predominant subunit expressed in normotensive animals(*331*). Interestingly. previous research has indicated that the expression of the β subunit subtype is crucial for the formation of $Ca_V1.2$ channel clusters and densities of different sizes in the plasma membrane(*335*). Based on these findings, our model predicts that both a decrease in nucleating and growth probabilities are involved in this process.

4.3 Fundamental findings of $Ca_V1.2$ and $K_V2.1$ channel interactions

The clustering and activity of $Ca_V1.2$ and $K_V2.1$ are important for arterial smooth muscle physiological function. $Ca_V1.2$ channels are the primary means of raising intracellular Ca^{2+} levels in arterial smooth muscle cells. Key to this physiological role is that these channels form clusters and functionally cooperate. In this model, clustered channels can

cooperatively gate, via a Ca^{2+}-calmodulin interaction, to amplify Ca^{2+} entry. On the contrary, $K_V2.1$ channels function as voltage-gated potassium channels which hyperpolarize the cell membrane upon activation, decreasing intracellular Ca^{2+} concentrations and myogenic tone. However, the work contained here and previously reported(*287*) propose that $K_V2.1$ channels have a more complex function in vascular smooth muscle, playing opposing roles in regulating the membrane potential and enhancing $Ca_V1.2$ activity. In its typical role, $K_V2.1$ opening induces relaxation by decreasing the P_O of $Ca_V1.2$ channels and subsequently lowering $[Ca^{2+}]_i$. However, our findings support a non-canonical role for $K_V2.1$ protein playing a structural role in arterial myocytes, where it enhances $Ca_V1.2$ clustering and activity in females, leading to an increase in $[Ca^{2+}]_i$ and inducing contraction.

We propose a model in which $K_V2.1$ channel clustering has a unique structural function for $Ca_V1.2$ interactions in female arterial smooth muscle. Our results indicate that the mutation of a critical phosphorylation site (S590A) in the PRC domain of $K_V2.1$, which is responsible for the clustering of $K_V2.1$ channels, leads to a reduction in the expression of macro-clusters of these channels. This decrease is accompanied by a sex-dependent decrease in the size of the clusters, especially macro-clusters. However, males, regardless of mutation, exhibit smaller $K_V2.1$ clusters compared to WT females and are largely similar to each other in all metrics measured. Furthermore, the cluster characteristics of $K_V2.1_{S590A}$ females are similar to those of males. Based on our modeling presenting in Chapter 2, we can speculate that WT females may possess a transcription factor or enhanced regulatory mechanism such as hyper-phosphorylation

that is absent in males. However, further studies are necessary to investigate this possibility.

In support of our findings in Chapter 3, Vierra et al. (*288*), reported that the co-expression of WT $K_V2.1$ and $Ca_V1.2$ channels induced $Ca_V1.2$ clustering in HEK-293 cells and hippocampal neurons. However, the expression of $K_V2.1_{S586A}$, which does not cluster, failed to promote $Ca_V1.2$ clustering. Additionally, they demonstrated that treatments that affect $K_V2.1$ clustering also rapidly and dynamically regulate $Ca_V1.2$ clustering in both cell types. These findings suggest that the expression and clustering state of $K_V2.1$ channels directly and actively regulate $Ca_V1.2$ clustering. It is of note that this $Ca_V1.2$-$K_V2.1$ interaction could be recapitulated in HEK-293 cells, which are female. Future studies would have to determine under what conditions this interaction occurs. It is intriguing that O'Dwyer et al.(*287*) found that $K_V2.1$ regulates both relaxation and contraction in arterial smooth muscle. Importantly, they found that the relative contribution of the electrical and structural roles of $K_V2.1$ in controlling membrane potential and $Ca_V1.2$ activity, respectively, differ between sexes. In male myocytes, the dominant role for $K_V2.1$ channels is as an ion channel that regulates membrane potential. In contrast, in female myocytes, $K_V2.1$ channels have dual electrical and structural roles that regulate both membrane potential and enhance $Ca_V1.2$ function. Our results from $K_V2.1_{S590A}$ mutation mice were similar to those previously published in $K_V2.1^{-/-}$ mice(*287*). Specifically, whole cell I_{Ca} was similar between WT, $K_V2.1_{S590A}$ and $K_V2.1^{-/-}$ male myocytes yet were significantly reduced in $K_V2.1_{S590A}$ and $K_V2.1^{-/-}$ compared to the WT female myocytes. Additionally, $Ca_V1.2$ clusters sizes measured

with super resolution microscopy followed this trend. This would suggest that $Ca_V1.2$ channels are not dependent on $K_V2.1$ to cluster, yet $K_V2.1$ macro-clusters could serve as a growth factor (P_g) for $Ca_V1.2$ clusters in females based on our model in Chapter 2.

4.4 Reflections and conclusions

Our study raises an important question regarding the phosphorylation of $K_V2.1$ and the formation of macro-clusters in females versus males. $K_V2.1$ clustering is regulated by a myriad of kinases such as CDK5 and phosphatases such calcineurin(*309*). These kinases and phosphatases work in a rheostatic mechanism to regulate the phosphorylation status of $K_V2.1$ based on physiological demands. The clustering phenotype of $K_V2.1$ depends on the phosphorylated status of the channel, whereas dephosphorylation decreases clustering. One possibility in our system is that basal kinase activity is higher in females than males. To address this question, western blot analysis or immunocytochemistry targeting phosphorylated $K_V2.1$ and total $K_V2.1$ expression could be used. We would expect to observe a smaller $K_V2.1$ phosphorylation to total $K_V2.1$ ratio in males compared to females.

Although our research has provided strong evidence for the impact of both $K_V2.1$ and $Ca_V1.2$ organization and function in male and female mesenteric arteries, we did not investigate other vascular beds or regions within a vascular tree. Our recent work has shown that the distance between two proteins can vary not only between sexes but also in different arterial beds within the same sex, highlighting the need to explore the consistency of our observations throughout various tissues(*336*). Potential experiments

could focus on $Ca_V1.2$-$K_V2.1$ interactions in this vascular tree at a cellular level, the myogenic response in isolated arteries, and even study of the blood flow within the brain under various genetic manipulations. It would be imperative to study whether there exist any sex-based differences in various beds and orders of the vascular branches. To our knowledge, no studies have compared $Ca_V1.2$ expression or cluster sizes between different arterial beds, and potential next steps could explore $Ca_V1.2$'s trafficking and organization within different arterial beds, as well as whether $K_V2.1$ continues to play its structural role as seen in Chapters 2 and 3.

One of $K_V2.1$ clusters non-canonical structural roles is to tether the endoplasmic reticulum to the plasma membrane (ER-PM junctions)(*171, 172, 337-339*). These are sites where the plasma membrane is brought into close juxtaposition with the ER and represent specialized signaling domains(*340*). In arterial smooth muscle, extensive work has shown that the existence of these junctions(*341, 342*), although we are not aware of any studies looking at the presence of $K_V2.1$ at these junctions. Future studies will investigate the composition of these microdomains and whether these are sites of enhanced $K_V2.1$ mediated clustering of $Ca_V1.2$ channels.

In neurons, ER-PM junctions are sites where $K_V2.1$ has been shown to colocalize with ryanodine receptors (RyR) forming signaling units with L-type Ca^{2+} channels to enhance Ca^{2+} influx. However, in smooth muscle, sparks via RyR are critical for the negative feedback of membrane depolarization. These localized RyR Ca^{2+} signals activate nearby large, Ca^{2+} sensitive K^+ channels (BK_{Ca}) resulting in an outward current. These

can be visualized as spontaneous transient outward currents (STOCs) that ultimately result in vasodilation(*196*). Our study raises questions about whether macro-clusters of $K_V2.1$ in females could also be a site for RyR-BK_{Ca} interactions. Future studies will aim to determine whether $K_V2.1$ has a structural role in this interaction, investigate whether de-clustering $K_V2.1$ affects ER-PM junctions and/or alters BK_{Ca}-RyR coupling, and assess the physiological significance of these findings in arterial smooth muscle relaxation in a sex-dependent manner. We can speculate that the disruption of BK_{Ca}-RYR interactions and the inhibition of smooth muscle relaxation can be achieved by de-clustering $K_V2.1$. We envision experiments in our laboratory that utilize simultaneous recording of membrane potential and Ca^{2+} imaging to determine BK_{Ca}-RyR coupling. In depth analysis of spark amplitudes, spread and frequency coupled to BK_{Ca} current amplitude and frequency could provide novel insight into this interaction. Additionally, future studies would look at this interaction and whether the sex-based differences in this interaction would also have physiological consequences for the development of myogenic tone.

The sex-specific component hints at an interesting avenue of study. What exactly is the role of various sex hormones on the formation of $K_V2.1$ clustering and $Ca_V1.2$ dynamics? An intriguing approach would be to investigate the impact of ovariectomy and castration in mice on the organization of $Ca_V1.2$ and $K_V2.1$, and their respective roles in the regulation of smooth muscle function. Additionally, it would be interesting to see if there are alterations to blood pressure, myogenic tone, $Ca_V1.2$ and $K_V2.1$ channel activity or clustering in response to these changes. Finally, it would be interesting to

study whether re-addition of sex-hormones to the ovariectomized or castrated mice rescues the phenotype.

Additional questions raised in the study regard the physiological consequences of the $K_V2.1_{S590A}$ mutation. Previous work from our lab has provided evidence that female mesenteric arteries express more $K_V2.1$, larger $Ca_V1.2$ channel clusters and exhibit higher levels of $[Ca^{2+}]_i$ compared to males. Collectively this result in enhanced myogenic tone in females compared to males. We would hypothesize that $K_V2.1_{S590A}$ females would have decreased myogenic due to decreased $Ca_V1.2$ clusters activity. Future studies will aim to further elucidate the functional consequences of this mutation and whether targeting this interaction could provide a therapeutic option for blood pressure regulation.

In conclusion, this dissertation investigates the mechanisms of ion channel formation in murine mesenteric smooth muscle cells, focusing on the clustering and interactions of $K_V2.1$ and $Ca_V1.2$ ion channels. The study proposes a model by which ion channel clusters form stochastically via a self-assembly process in the membrane based on three mechanistic probabilities. The findings suggest that $K_V2.1$ clustering state is not a determinant of channel conduction in mesenteric smooth muscle and $K_V2.1$ macro-clusters serve as a sex-specific site for increased $Ca_V1.2$ clustering, which plays a key role in Ca^{2+} dynamics and smooth muscle physiology. Overall, the study sheds light on the mechanisms involved in the trafficking of ion channels and maintenance of clusters

in the plasma membrane, providing potential reasoning for sex-based differences in smooth muscle physiology.

References

1. M. R. Boyett, H. Honjo, I. Kodama, The sinoatrial node, a heterogeneous pacemaker structure. *Cardiovasc Res* **47**, 658-687 (2000).
2. I. Kodama *et al.*, Regional differences in the role of the Ca2+ and Na+ currents in pacemaker activity in the sinoatrial node. *Am J Physiol* **272**, H2793-2806 (1997).
3. M. Yamamoto, H. Honjo, R. Niwa, I. Kodama, Low-frequency extracellular potentials recorded from the sinoatrial node. *Cardiovasc Res* **39**, 360-372 (1998).
4. W. K. Bleeker, A. J. Mackaay, M. Masson-Pévet, L. N. Bouman, A. E. Becker, Functional and morphological organization of the rabbit sinus node. *Circ Res* **46**, 11-22 (1980).
5. N. Grainger, L. Guarina, R. H. Cudmore, L. F. Santana, The Organization of the Sinoatrial Node Microvasculature Varies Regionally to Match Local Myocyte Excitability. *Function (Oxf)* **2**, zqab031 (2021).
6. J. K. Douglass, L. Wilkens, E. Pantazelou, F. Moss, Noise enhancement of information transfer in crayfish mechanoreceptors by stochastic resonance. *Nature* **365**, 337-340 (1993).
7. A. A. Faisal, L. P. Selen, D. M. Wolpert, Noise in the nervous system. *Nature reviews neuroscience* **9**, 292-303 (2008).
8. C. E. Clancy, L. F. Santana, Evolving Discovery of the Origin of the Heartbeat: A New Perspective on Sinus Rhythm. *JACC Clin Electrophysiol* **6**, 932-934 (2020).
9. A. Peña-Romo, A. M. Gámez-Méndez, A. Ríos, B. A. Escalante, J. Rodríguez-González, Noise enhanced the electrical stimulation-contractile response coupling in isolated mouse heart. *International Journal of Cardiology* **221**, 155-160 (2016).
10. C. Franzini-Armstrong, F. Protasi, V. Ramesh, Shape, Size, and Distribution of Ca2+ Release Units and Couplons in Skeletal and Cardiac Muscles. *Biophysical Journal* **77**, 1528-1539 (1999).
11. M. D. Stern, G. Pizarro, E. Ríos, Local Control Model of Excitation–Contraction Coupling in Skeletal Muscle. *Journal of General Physiology* **110**, 415-440 (1997).
12. H. Cheng, W. J. Lederer, M. B. Cannell, Calcium sparks: elementary events underlying excitation-contraction coupling in heart muscle. *Science* **262**, 740-744 (1993).
13. J. H. Bridge, J. R. Smolley, K. W. Spitzer, The relationship between charge movements associated with ICa and INa-Ca in cardiac myocytes. *Science* **248**, 376-378 (1990).
14. D. Eisner, Calcium in the heart: from physiology to disease. *Experimental Physiology* **99**, 1273-1282 (2014).
15. Y. Kimura, K. Kurzydlowski, M. Tada, D. H. MacLennan, Phospholamban inhibitory function is activated by depolymerization. *J Biol Chem* **272**, 15061-15064 (1997).
16. a. M Tada, A. M. Katz, Phosphorylation of the Sarcoplasmic Reticulum and Sarcolemma. *Annual Review of Physiology* **44**, 401-423 (1982).
17. N. Stafford, C. Wilson, D. Oceandy, L. Neyses, E. J. Cartwright, The Plasma Membrane Calcium ATPases and Their Role as Major New Players in Human Disease. *Physiological Reviews* **97**, 1089-1125 (2017).
18. A. F. Huxley, R. Niedergerke, Structural changes in muscle during contraction; interference microscopy of living muscle fibres. *Nature* **173**, 971-973 (1954).
19. H. Huxley, J. Hanson, Changes in the cross-striations of muscle during contraction and stretch and their structural interpretation. *Nature* **173**, 973-976 (1954).
20. A. M. Gordon, A. F. Huxley, F. J. Julian, The variation in isometric tension with sarcomere length in vertebrate muscle fibres. *J Physiol* **184**, 170-192 (1966).
21. M. K. Pugsley, R. Tabrizchi, The vascular system. An overview of structure and function. *J Pharmacol Toxicol Methods* **44**, 333-340 (2000).

22. J. A. G. Rhodin, The ultrastructure of mammalian arterioles and precapillary sphincters. *Journal of Ultrastructure Research* **18**, 181-223 (1967).
23. H. F. Galley, N. R. Webster, Physiology of the endothelium. *Br J Anaesth* **93**, 105-113 (2004).
24. K. A. Dora, Cell-cell communication in the vessel wall. *Vasc Med* **6**, 43-50 (2001).
25. W. C. Aird, Phenotypic heterogeneity of the endothelium: I. Structure, function, and mechanisms. *Circ Res* **100**, 158-173 (2007).
26. M. J. Lew, R. J. Rivers, B. R. Duling, Arteriolar smooth muscle responses are modulated by an intramural diffusion barrier. *Am J Physiol* **257**, H10-16 (1989).
27. R. Daneman, A. Prat, The blood-brain barrier. *Cold Spring Harb Perspect Biol* **7**, a020412 (2015).
28. L. Ghitescu, M. Robert, Diversity in unity: the biochemical composition of the endothelial cell surface varies between the vascular beds. *Microsc Res Tech* **57**, 381-389 (2002).
29. G. G. Emerson, S. S. Segal, Endothelial cell pathway for conduction of hyperpolarization and vasodilation along hamster feed artery. *Circ Res* **86**, 94-100 (2000).
30. T. L. Haas, B. R. Duling, Morphology favors an endothelial cell pathway for longitudinal conduction within arterioles. *Microvasc Res* **53**, 113-120 (1997).
31. B. O. Hald, D. G. Welsh, Conceptualizing conduction as a pliant electrical response: impact of gap junctions and ion channels. *Am J Physiol Heart Circ Physiol* **319**, H1276-h1289 (2020).
32. B. E. Isakson, B. R. Duling, Heterocellular contact at the myoendothelial junction influences gap junction organization. *Circ Res* **97**, 44-51 (2005).
33. S. Mather, K. A. Dora, S. L. Sandow, P. Winter, C. J. Garland, Rapid endothelial cell-selective loading of connexin 40 antibody blocks endothelium-derived hyperpolarizing factor dilation in rat small mesenteric arteries. *Circ Res* **97**, 399-407 (2005).
34. S. L. Sandow, S. Senadheera, P. P. Bertrand, T. V. Murphy, M. Tare, Myoendothelial contacts, gap junctions, and microdomains: anatomical links to function? *Microcirculation* **19**, 403-415 (2012).
35. S. L. Sandow, M. Tare, H. A. Coleman, C. E. Hill, H. C. Parkington, Involvement of myoendothelial gap junctions in the actions of endothelium-derived hyperpolarizing factor. *Circ Res* **90**, 1108-1113 (2002).
36. E. Svendsen, A. M. Austarheim, B. Haugen, H. Dalen, E. Dregelid, Myoendothelial junctions in human saphenous veins. *Acta Anat (Basel)* **138**, 150-153 (1990).
37. A. C. Straub, A. C. Zeigler, B. E. Isakson, The myoendothelial junction: connections that deliver the message. *Physiology (Bethesda)* **29**, 242-249 (2014).
38. C. J. Garland, K. A. Dora, Endothelium-Dependent Hyperpolarization: The Evolution of Myoendothelial Microdomains. *J Cardiovasc Pharmacol* **78**, S3-s12 (2021).
39. G. C. Wellman, A. D. Bonev, M. T. Nelson, J. E. Brayden, Gender Differences in Coronary Artery Diameter Involve Estrogen, Nitric Oxide, and Ca²⁺-Dependent K⁺ Channels. *Circulation Research* **79**, 1024-1030 (1996).
40. T. Ishikawa, J. R. Hume, K. D. Keef, Regulation of Ca2+ channels by cAMP and cGMP in vascular smooth muscle cells. *Circulation Research* **73**, 1128-1137 (1993).
41. B. E. Robertson, R. Schubert, J. Hescheler, M. T. Nelson, cGMP-dependent protein kinase activates Ca-activated K channels in cerebral artery smooth muscle cells. *American Journal of Physiology-Cell Physiology* **265**, C299-C303 (1993).
42. V. M. Bolotina, S. Najibi, J. J. Palacino, P. J. Pagano, R. A. Cohen, Nitric oxide directly activates calcium-dependent potassium channels in vascular smooth muscle. *Nature* **368**, 850-853 (1994).
43. M. La, J. J. Reid, ENDOTHELIN-1 AND THE REGULATION OF VASCULAR TONE. *Clinical and Experimental Pharmacology and Physiology* **22**, 315-323 (1995).

44. M. S. Taylor *et al.*, Altered expression of small-conductance Ca2+-activated K+ (SK3) channels modulates arterial tone and blood pressure. *Circ Res* **93**, 124-131 (2003).
45. J. Ledoux *et al.*, Functional architecture of inositol 1,4,5-trisphosphate signaling in restricted spaces of myoendothelial projections. *Proc Natl Acad Sci U S A* **105**, 9627-9632 (2008).
46. R. Köhler *et al.*, Evidence for a functional role of endothelial transient receptor potential V4 in shear stress-induced vasodilatation. *Arterioscler Thromb Vasc Biol* **26**, 1495-1502 (2006).
47. S. P. Marrelli, G. O'Neil R, R. C. Brown, R. M. Bryan, Jr., PLA2 and TRPV4 channels regulate endothelial calcium in cerebral arteries. *Am J Physiol Heart Circ Physiol* **292**, H1390-1397 (2007).
48. D. X. Zhang *et al.*, Transient receptor potential vanilloid type 4-deficient mice exhibit impaired endothelium-dependent relaxation induced by acetylcholine in vitro and in vivo. *Hypertension* **53**, 532-538 (2009).
49. S. K. Sonkusare *et al.*, Elementary Ca2+ signals through endothelial TRPV4 channels regulate vascular function. *Science* **336**, 597-601 (2012).
50. M. J. Berridge, Inositol trisphosphate and calcium signalling. *Nature* **361**, 315-325 (1993).
51. J. K. Foskett, C. White, K. H. Cheung, D. O. Mak, Inositol trisphosphate receptor Ca2+ release channels. *Physiol Rev* **87**, 593-658 (2007).
52. D. O. Mak, J. K. Foskett, Inositol 1,4,5-trisphosphate receptors in the endoplasmic reticulum: A single-channel point of view. *Cell Calcium* **58**, 67-78 (2015).
53. O. F. Harraz, T. A. Longden, D. Hill-Eubanks, M. T. Nelson, PIP(2) depletion promotes TRPV4 channel activity in mouse brain capillary endothelial cells. *Elife* **7**, (2018).
54. S. Earley, Endothelium-dependent cerebral artery dilation mediated by transient receptor potential and Ca2+-activated K+ channels. *J Cardiovasc Pharmacol* **57**, 148-153 (2011).
55. S. K. Sonkusare *et al.*, AKAP150-dependent cooperative TRPV4 channel gating is central to endothelium-dependent vasodilation and is disrupted in hypertension. *Sci Signal* **7**, ra66 (2014).
56. S. Earley, A. L. Gonzales, R. Crnich, Endothelium-dependent cerebral artery dilation mediated by TRPA1 and Ca2+-Activated K+ channels. *Circ Res* **104**, 987-994 (2009).
57. X. Qian, M. Francis, V. Solodushko, S. Earley, M. S. Taylor, Recruitment of dynamic endothelial Ca2+ signals by the TRPA1 channel activator AITC in rat cerebral arteries. *Microcirculation* **20**, 138-148 (2013).
58. M. N. Sullivan *et al.*, Localized TRPA1 channel Ca2+ signals stimulated by reactive oxygen species promote cerebral artery dilation. *Sci Signal* **8**, ra2 (2015).
59. W. F. Jackson, Endothelial cell ion channel expression and function in arterioles and resistance arteries. *Vascular ion channels in physiology and disease*, 3-36 (2016).
60. T. A. Longden *et al.*, Capillary K(+)-sensing initiates retrograde hyperpolarization to increase local cerebral blood flow. *Nat Neurosci* **20**, 717-726 (2017).
61. M. Sancho *et al.*, Adenosine signaling activates ATP-sensitive K(+) channels in endothelial cells and pericytes in CNS capillaries. *Sci Signal* **15**, eabl5405 (2022).
62. C. M. Anderson, J. P. Bergher, R. A. Swanson, ATP-induced ATP release from astrocytes. *J Neurochem* **88**, 246-256 (2004).
63. J. A. Filosa, A. D. Bonev, M. T. Nelson, Calcium dynamics in cortical astrocytes and arterioles during neurovascular coupling. *Circ Res* **95**, e73-81 (2004).
64. J. A. Filosa *et al.*, Local potassium signaling couples neuronal activity to vasodilation in the brain. *Nat Neurosci* **9**, 1397-1403 (2006).
65. H. Girouard *et al.*, Astrocytic endfoot Ca2+ and BK channels determine both arteriolar dilation and constriction. *Proc Natl Acad Sci U S A* **107**, 3811-3816 (2010).

66. S. J. Mulligan, B. A. MacVicar, Calcium transients in astrocyte endfeet cause cerebrovascular constrictions. *Nature* **431**, 195-199 (2004).
67. M. F. Muñoz, M. Puebla, X. F. Figueroa, Control of the neurovascular coupling by nitric oxide-dependent regulation of astrocytic Ca(2+) signaling. *Front Cell Neurosci* **9**, 59 (2015).
68. A. Mughal, M. T. Nelson, D. Hill-Eubanks, The post-arteriole transitional zone: a specialized capillary region that regulates blood flow within the CNS microvasculature. *The Journal of Physiology* **601**, 889-901 (2023).
69. D. Attwell, A. Mishra, C. N. Hall, F. M. O'Farrell, T. Dalkara, What is a pericyte? *J Cereb Blood Flow Metab* **36**, 451-455 (2016).
70. C. Rouget, Memoire sur le develloppment, la structure et les propietes physiologiques des capillaries senguins et lymphatiques. *Arch. Physiol. Norm. Pathol.* **5**, 603-663 (1873).
71. K. W. Zimmermann, Der feinere bau der blutcapillaren. (1923).
72. T. M. Mathiisen, K. P. Lehre, N. C. Danbolt, O. P. Ottersen, The perivascular astroglial sheath provides a complete covering of the brain microvessels: an electron microscopic 3D reconstruction. *Glia* **58**, 1094-1103 (2010).
73. E. A. Winkler, R. D. Bell, B. V. Zlokovic, Central nervous system pericytes in health and disease. *Nature Neuroscience* **14**, 1398-1405 (2011).
74. T. Dalkara, Y. Gursoy-Ozdemir, M. Yemisci, Brain microvascular pericytes in health and disease. *Acta Neuropathol* **122**, 1-9 (2011).
75. C. N. Hall *et al.*, Capillary pericytes regulate cerebral blood flow in health and disease. *Nature* **508**, 55-60 (2014).
76. N. B. Hamilton, D. Attwell, C. N. Hall, Pericyte-mediated regulation of capillary diameter: a component of neurovascular coupling in health and disease. *Front Neuroenergetics* **2**, (2010).
77. Y. Itoh, N. Suzuki, Control of brain capillary blood flow. *J Cereb Blood Flow Metab* **32**, 1167-1176 (2012).
78. C. M. Peppiatt, C. Howarth, P. Mobbs, D. Attwell, Bidirectional control of CNS capillary diameter by pericytes. *Nature* **443**, 700-704 (2006).
79. D. G. Puro, Physiology and pathobiology of the pericyte-containing retinal microvasculature: new developments. *Microcirculation* **14**, 1-10 (2007).
80. G. Zhao, H. C. Joca, M. T. Nelson, W. J. Lederer, ATP- and voltage-dependent electro-metabolic signaling regulates blood flow in heart. *Proc Natl Acad Sci U S A* **117**, 7461-7470 (2020).
81. I. A. Greenwood, S. A. Prestwich, Characteristics of hyperpolarization-activated cation currents in portal vein smooth muscle cells. *American Journal of Physiology-Cell Physiology* **282**, C744-C753 (2002).
82. H. Hashitani, A. F. Brading, Electrical properties of detrusor smooth muscles from the pig and human urinary bladder. *British Journal of Pharmacology* **140**, 146-158 (2003).
83. D. R. Harder, Pressure-dependent membrane depolarization in cat middle cerebral artery. *Circ Res* **55**, 197-202 (1984).
84. H. J. Knot, M. T. Nelson, Regulation of arterial diameter and wall [Ca2+] in cerebral arteries of rat by membrane potential and intravascular pressure. *J Physiol* **508 (Pt 1)**, 199-209 (1998).
85. J. C. Coffey, Surgical anatomy and anatomic surgery - Clinical and scientific mutualism. *Surgeon* **11**, 177-182 (2013).
86. J. C. Coffey *et al.*, Terminology and nomenclature in colonic surgery: universal application of a rule-based approach derived from updates on mesenteric anatomy. *Tech Coloproctol* **18**, 789-794 (2014).

87. K. L. Christensen, M. J. Mulvany, Mesenteric arcade arteries contribute substantially to vascular resistance in conscious rats. *J Vasc Res* **30**, 73-79 (1993).
88. W. M. Bayliss, On the local reactions of the arterial wall to changes of internal pressure. *The Journal of physiology* **28**, 220-231 (1902).
89. A. L. Gonzales *et al.*, A PLCγ1-dependent, force-sensitive signaling network in the myogenic constriction of cerebral arteries. *Sci Signal* **7**, ra49 (2014).
90. M. A. Spassova, T. Hewavitharana, W. Xu, J. Soboloff, D. L. Gill, A common mechanism underlies stretch activation and receptor activation of TRPC6 channels. *Proc Natl Acad Sci U S A* **103**, 16586-16591 (2006).
91. S. Bulley *et al.*, Arterial smooth muscle cell PKD2 (TRPP1) channels regulate systemic blood pressure. *Elife* **7**, (2018).
92. M. F. Navedo, L. F. Santana, CaV1.2 sparklets in heart and vascular smooth muscle. *J Mol Cell Cardiol* **58**, 67-76 (2013).
93. M. F. Navedo, G. C. Amberg, V. S. Votaw, L. F. Santana, Constitutively active L-type Ca2+ channels. *Proc Natl Acad Sci U S A* **102**, 11112-11117 (2005).
94. G. C. Amberg, M. F. Navedo, M. Nieves-Cintrón, J. D. Molkentin, L. F. Santana, Calcium sparklets regulate local and global calcium in murine arterial smooth muscle. *J Physiol* **579**, 187-201 (2007).
95. J. T. Herlihy, R. A. Murphy, Length-tension relationship of smooth muscle of the hog carotid artery. *Circ Res* **33**, 275-283 (1973).
96. D. A. Eisner, J. L. Caldwell, K. Kistamás, A. W. Trafford, Calcium and Excitation-Contraction Coupling in the Heart. *Circ Res* **121**, 181-195 (2017).
97. M. Davis, M. Hill, L. Kuo, R. Terjung, Compr Physiol. (2011).
98. R. Casteels, Electro- and pharmacomechanical coupling in vascular smooth muscle. *Chest* **78**, 150-156 (1980).
99. T. Itoh, Pharmacomechanical coupling in vascular smooth muscle cells--an overview. *Jpn J Pharmacol* **55**, 1-9 (1991).
100. L. Te Riet, J. H. van Esch, A. J. Roks, A. H. van den Meiracker, A. H. Danser, Hypertension: renin-angiotensin-aldosterone system alterations. *Circ Res* **116**, 960-975 (2015).
101. S. Eguchi, T. Kawai, R. Scalia, V. Rizzo, Understanding Angiotensin II Type 1 Receptor Signaling in Vascular Pathophysiology. *Hypertension* **71**, 804-810 (2018).
102. J. Schleifenbaum *et al.*, Stretch–activation of angiotensin II type 1a receptors contributes to the myogenic response of mouse mesenteric and renal arteries. *Circulation research* **115**, 263-272 (2014).
103. Y. Cui *et al.*, Myogenic Vasoconstriction Requires Canonical G(q/11) Signaling of the Angiotensin II Type 1 Receptor. *J Am Heart Assoc* **11**, e022070 (2022).
104. M. T. Nelson *et al.*, Relaxation of Arterial Smooth Muscle by Calcium Sparks. *Science* **270**, 633 (1995).
105. G. C. Amberg, L. F. Santana, Kv2 channels oppose myogenic constriction of rat cerebral arteries. *Am J Physiol Cell Physiol* **291**, C348-356 (2006).
106. F. Plane *et al.*, Heteromultimeric Kv1 channels contribute to myogenic control of arterial diameter. *Circ Res* **96**, 216-224 (2005).
107. M. J. Davis, Myogenic response gradient in an arteriolar network. *Am J Physiol* **264**, H2168-2179 (1993).
108. P. C. Johnson, The myogenic response in the microcirculation and its interaction with other control systems. *J Hypertens Suppl* **7**, S33-39; discussion S40 (1989).
109. W. A. Catterall, Voltage-gated calcium channels. *Cold Spring Harb Perspect Biol* **3**, a003947 (2011).

110. H. Ma, R. D. Groth, D. G. Wheeler, C. F. Barrett, R. W. Tsien, Excitation-transcription coupling in sympathetic neurons and the molecular mechanism of its initiation. *Neurosci Res* **70**, 2-8 (2011).
111. S. Moosmang, T. Kleppisch, J. Wegener, A. Welling, F. Hofmann, Analysis of calcium channels by conditional mutagenesis. *Handb Exp Pharmacol*, 469-490 (2007).
112. W. A. Catterall, E. Perez-Reyes, T. P. Snutch, J. Striessnig, International Union of Pharmacology. XLVIII. Nomenclature and structure-function relationships of voltage-gated calcium channels. *Pharmacol Rev* **57**, 411-425 (2005).
113. G. C. Amberg, M. F. Navedo, Calcium dynamics in vascular smooth muscle. *Microcirculation* **20**, 281-289 (2013).
114. M. T. Nelson, J. B. Patlak, J. F. Worley, N. B. Standen, Calcium channels, potassium channels, and voltage dependence of arterial smooth muscle tone. *American Journal of Physiology* **259**, C3-C18 (1990).
115. J. Wu *et al.*, Structure of the voltage-gated calcium channel Cav1.1 complex. *Science* **350**, aad2395 (2015).
116. J. Wu *et al.*, Structure of the voltage-gated calcium channel Cav1.1 at 3.6 Å resolution. *Nature* **537**, 191-196 (2016).
117. J. Wu, N. Yan, Z. Yan, Structure-Function Relationship of the Voltage-Gated Calcium Channel Ca(v)1.1 Complex. *Adv Exp Med Biol* **981**, 23-39 (2017).
118. W. A. Catterall, Structure and Regulation of Voltage-Gated Ca2+ Channels. *Annu. Rev. Cell Dev. Biol.* **16**, 521-555 (2000).
119. L. Birnbaumer *et al.*, Structures and functions of calcium channel beta subunits. *J Bioenerg Biomembr* **30**, 357-375 (1998).
120. J. P. Bannister *et al.*, Smooth muscle cell alpha2delta-1 subunits are essential for vasoregulation by CaV1.2 channels. *Circ Res* **105**, 948-955 (2009).
121. L. Yang, A. Katchman, J. P. Morrow, D. Doshi, S. O. Marx, Cardiac L-type calcium channel (Cav1.2) associates with gamma subunits. *Faseb j* **25**, 928-936 (2011).
122. A. Neely, P. Hidalgo, Structure-function of proteins interacting with the α1 pore-forming subunit of high-voltage-activated calcium channels. *Frontiers in Physiology* **5**, (2014).
123. R. R. Abd El-Rahman *et al.*, Identification of L- and T-type Ca2+ channels in rat cerebral arteries: role in myogenic tone development. *Am J Physiol Heart Circ Physiol* **304**, H58-71 (2013).
124. O. F. Harraz *et al.*, Ca(V)3.2 channels and the induction of negative feedback in cerebral arteries. *Circ Res* **115**, 650-661 (2014).
125. O. F. Harraz *et al.*, Genetic ablation of CaV3.2 channels enhances the arterial myogenic response by modulating the RyR-BKCa axis. *Arterioscler Thromb Vasc Biol* **35**, 1843-1851 (2015).
126. O. F. Harraz *et al.*, CaV1.2/CaV3.x channels mediate divergent vasomotor responses in human cerebral arteries. *J Gen Physiol* **145**, 405-418 (2015).
127. L. L. Cribbs, T-type Ca2+ channels in vascular smooth muscle: multiple functions. *Cell Calcium* **40**, 221-230 (2006).
128. A. C. Dolphin, Voltage-gated calcium channels and their auxiliary subunits: physiology and pathophysiology and pharmacology. *J Physiol* **594**, 5369-5390 (2016).
129. E. Perez-Reyes, Molecular characterization of T-type calcium channels. *Cell Calcium* **40**, 89-96 (2006).
130. F. Gustafsson, D. Andreasen, M. Salomonsson, B. L. Jensen, N. Holstein-Rathlou, Conducted vasoconstriction in rat mesenteric arterioles: role for dihydropyridine-insensitive Ca(2+) channels. *Am J Physiol Heart Circ Physiol* **280**, H582-590 (2001).
131. T. Cens, M. Rousset, J. P. Leyris, P. Fesquet, P. Charnet, Voltage- and calcium-dependent inactivation in high voltage-gated Ca(2+) channels. *Prog Biophys Mol Biol* **90**, 104-117 (2006).

132. R. S. Kass, M. C. Sanguinetti, Inactivation of calcium channel current in the calf cardiac Purkinje fiber. Evidence for voltage- and calcium-mediated mechanisms. *J Gen Physiol* **84**, 705-726 (1984).
133. K. S. Lee, E. Marban, R. W. Tsien, Inactivation of calcium channels in mammalian heart cells: joint dependence on membrane potential and intracellular calcium. *J Physiol* **364**, 395-411 (1985).
134. D. T. Yue, P. H. Backx, J. P. Imredy, Calcium-sensitive inactivation in the gating of single calcium channels. *Science* **250**, 1735-1738 (1990).
135. S. Weiss, N. Dascal, Molecular Aspects of Modulation of L-type Calcium Channels by Protein Kinase C. *Curr Mol Pharmacol* **8**, 43-53 (2015).
136. K. D. Keef, J. R. Hume, J. Zhong, Regulation of cardiac and smooth muscle Ca2+channels (CaV1.2a,b) by protein kinases. *American Journal of Physiology-Cell Physiology* **281**, C1743-C1756 (2001).
137. J. Zhang *et al.*, Role of Cav1.2 L-type Ca2+ channels in vascular tone: effects of nifedipine and Mg2+. *Am J Physiol Heart Circ Physiol* **292**, H415-425 (2007).
138. B. K. Fleischmann, R. K. Murray, M. I. Kotlikoff, Voltage window for sustained elevation of cytosolic calcium in smooth muscle cells. *Proc Natl Acad Sci U S A* **91**, 11914-11918 (1994).
139. C. Seisenberger *et al.*, Functional embryonic cardiomyocytes after disruption of the L-type alpha1C (Cav1.2) calcium channel gene in the mouse. *J Biol Chem* **275**, 39193-39199 (2000).
140. S. Moosmang *et al.*, Dominant role of smooth muscle L-type calcium channel Cav1 2 for blood pressure. *EMBO J* **22**, 6027-6034 (2003).
141. M. Rubart, J. B. Patlak, M. T. Nelson, Ca2+ currents in cerebral artery smooth muscle cells of rat at physiological Ca2+ concentrations. *J Gen Physiol* **107**, 459-472 (1996).
142. D. Sato *et al.*, A stochastic model of ion channel cluster formation in the plasma membrane. *Journal of General Physiology* **151**, 1116-1134 (2019).
143. R. E. Dixon, C. Yuan, E. P. Cheng, M. F. Navedo, L. F. Santana, Ca2+ signaling amplification by oligomerization of L-type Cav1.2 channels. *Proc Natl Acad Sci U S A* **109**, 1749-1754 (2012).
144. M. F. Navedo *et al.*, Increased coupled gating of L-type Ca2+ channels during hypertension and Timothy syndrome. *Circ Res* **106**, 748-756 (2010).
145. E. P. Cheng *et al.*, Restoration of normal L-type Ca2+ channel function during Timothy syndrome by ablation of an anchoring protein. *Circ Res* **109**, 255-261 (2011).
146. R. E. Dixon *et al.*, Graded Ca2+/calmodulin-dependent coupling of voltage-gated CaV1.2 channels. *eLife* **4**, e05608 (2015).
147. M. F. Navedo, G. C. Amberg, M. Nieves, J. D. Molkentin, L. F. Santana, Mechanisms underlying heterogeneous Ca2+ sparklet activity in arterial smooth muscle. *J Gen Physiol* **127**, 611-622 (2006).
148. M. F. Navedo *et al.*, AKAP150 is required for stuttering persistent Ca2+ sparklets and angiotensin II-induced hypertension. *Circ Res* **102**, e1-e11 (2008).
149. G. A. Gutman *et al.*, International Union of Pharmacology. LIII. Nomenclature and molecular relationships of voltage-gated potassium channels. *Pharmacol Rev* **57**, 473-508 (2005).
150. M. Nieves-Cintrón, A. U. Syed, M. A. Nystoriak, M. F. Navedo, Regulation of voltage-gated potassium channels in vascular smooth muscle during hypertension and metabolic disorders. *Microcirculation* **25**, (2018).
151. J. S. Trimmer, K. J. Rhodes, Localization of voltage-gated ion channels in mammalian brain. *Annu Rev Physiol* **66**, 477-519 (2004).
152. S. B. Long, E. B. Campbell, R. Mackinnon, Crystal structure of a mammalian voltage-dependent Shaker family K+ channel. *Science* **309**, 897-903 (2005).

153. Y. Lu, S. T. Hanna, G. Tang, R. Wang, Contributions of Kv1.2, Kv1.5 and Kv2.1 subunits to the native delayed rectifier K+ current in rat mesenteric artery smooth muscle cells. *Life Sciences* **71**, 1465-1473 (2002).
154. A. Cheong, A. M. Dedman, S. Z. Xu, D. J. Beech, K(V)alpha1 channels in murine arterioles: differential cellular expression and regulation of diameter. *Am J Physiol Heart Circ Physiol* **281**, H1057-1065 (2001).
155. N. R. Tykocki, E. M. Boerman, W. F. Jackson, Smooth Muscle Ion Channels and Regulation of Vascular Tone in Resistance Arteries and Arterioles. *Compr Physiol* **7**, 485-581 (2017).
156. Y. Lu, S. T. Hanna, G. Tang, R. Wang, Contributions of Kv1.2, Kv1.5 and Kv2.1 subunits to the native delayed rectifier K(+) current in rat mesenteric artery smooth muscle cells. *Life Sci* **71**, 1465-1473 (2002).
157. X. Z. Zhong *et al.*, Stromatoxin-sensitive, heteromultimeric Kv2.1/Kv9.3 channels contribute to myogenic control of cerebral arterial diameter. *J Physiol* **588**, 4519-4537 (2010).
158. S. J. Fountain *et al.*, Functional up-regulation of KCNA gene family expression in murine mesenteric resistance artery smooth muscle. *The Journal of Physiology* **556**, 29-42 (2004).
159. E. Bocksteins, D. J. Snyders, Electrically silent Kv subunits: their molecular and functional characteristics. *Physiology (Bethesda)* **27**, 73-84 (2012).
160. K. J. Rhodes, S. A. Keilbaugh, N. X. Barrezueta, K. L. Lopez, J. S. Trimmer, Association and colocalization of K+ channel alpha- and beta-subunit polypeptides in rat brain. *J Neurosci* **15**, 5360-5371 (1995).
161. R. H. Scannevin, H. Murakoshi, K. J. Rhodes, J. S. Trimmer, Identification of a cytoplasmic domain important in the polarized expression and clustering of the Kv2.1 K+ channel. *J Cell Biol* **135**, 1619-1632 (1996).
162. Z. Bekele-Arcuri *et al.*, Generation and characterization of subtype-specific monoclonal antibodies to K+ channel alpha- and beta-subunit polypeptides. *Neuropharmacology* **35**, 851-865 (1996).
163. G. Shi, A. K. Kleinklaus, N. V. Marrion, J. S. Trimmer, Properties of Kv2.1 K+ channels expressed in transfected mammalian cells. *J Biol Chem* **269**, 23204-23211 (1994).
164. S. T. Lim, D. E. Antonucci, R. H. Scannevin, J. S. Trimmer, A novel targeting signal for proximal clustering of the Kv2.1 K+ channel in hippocampal neurons. *Neuron* **25**, 385-397 (2000).
165. H. Misonou *et al.*, Regulation of ion channel localization and phosphorylation by neuronal activity. *Nature Neuroscience* **7**, 711-718 (2004).
166. H. Misonou, D. P. Mohapatra, M. Menegola, J. S. Trimmer, Calcium- and metabolic state-dependent modulation of the voltage-dependent Kv2.1 channel regulates neuronal excitability in response to ischemia. *J Neurosci* **25**, 11184-11193 (2005).
167. H. Murakoshi, G. Shi, R. H. Scannevin, J. S. Trimmer, Phosphorylation of the Kv2.1 K+ channel alters voltage-dependent activation. *Mol Pharmacol* **52**, 821-828 (1997).
168. K. Benndorf, R. Koopmann, C. Lorra, O. Pongs, Gating and conductance properties of a human delayed rectifier K+ channel expressed in frog oocytes. *J Physiol* **477**, 1-14 (1994).
169. P. D. Fox, R. J. Loftus, M. M. Tamkun, Regulation of Kv2.1 K(+) conductance by cell surface channel density. *J Neurosci* **33**, 1259-1270 (2013).
170. K. M. O'Connell, R. Loftus, M. M. Tamkun, Localization-dependent activity of the Kv2.1 delayed-rectifier K+ channel. *Proc Natl Acad Sci U S A* **107**, 12351-12356 (2010).
171. M. Kirmiz, N. C. Vierra, S. Palacio, J. S. Trimmer, Identification of VAPA and VAPB as Kv2 Channel-Interacting Proteins Defining Endoplasmic Reticulum–Plasma Membrane

Junctions in Mammalian Brain Neurons. *The Journal of Neuroscience* **38**, 7562-7584 (2018).
172. M. Kirmiz *et al.*, Remodeling neuronal ER–PM junctions is a conserved nonconducting function of Kv2 plasma membrane ion channels. *Molecular Biology of the Cell* **29**, 2410-2432 (2018).
173. J. T. Lanner, D. K. Georgiou, A. D. Joshi, S. L. Hamilton, Ryanodine receptors: structure, expression, molecular details, and function in calcium release. *Cold Spring Harb Perspect Biol* **2**, a003996 (2010).
174. Y. M. Zheng *et al.*, Heterogeneous gene expression and functional activity of ryanodine receptors in resistance and conduit pulmonary as well as mesenteric artery smooth muscle cells. *J Vasc Res* **45**, 469-479 (2008).
175. R. Zalk *et al.*, Structure of a mammalian ryanodine receptor. *Nature* **517**, 44-49 (2015).
176. F. O'Brien, E. Venturi, R. Sitsapesan, The ryanodine receptor provides high throughput Ca2+-release but is precisely regulated by networks of associated proteins: a focus on proteins relevant to phosphorylation. *Biochem Soc Trans* **43**, 426-433 (2015).
177. J. A. Copello, S. Barg, H. Onoue, S. Fleischer, Heterogeneity of Ca2+ gating of skeletal muscle and cardiac ryanodine receptors. *Biophys J* **73**, 141-156 (1997).
178. I. Györke, S. Györke, Regulation of the cardiac ryanodine receptor channel by luminal Ca2+ involves luminal Ca2+ sensing sites. *Biophysical journal* **75**, 2801-2810 (1998).
179. M. L. Collier, G. Ji, Y.-X. Wang, M. I. Kotlikoff, Calcium-Induced Calcium Release in Smooth Muscle: Loose Coupling between the Action Potential and Calcium Release. *Journal of General Physiology* **115**, 653-662 (2000).
180. G. W. Hennig, C. B. Smith, D. M. O'Shea, T. K. Smith, Patterns of intracellular and intercellular Ca2+ waves in the longitudinal muscle layer of the murine large intestine In vitro. *The Journal of Physiology* **543**, 233-253 (2002).
181. K. Essin, M. Gollasch, Role of ryanodine receptor subtypes in initiation and formation of calcium sparks in arterial smooth muscle: comparison with striated muscle. *J Biomed Biotechnol* **2009**, 135249 (2009).
182. J. H. Jaggar, V. A. Porter, W. J. Lederer, M. T. Nelson, Calcium sparks in smooth muscle. *Am J Physiol Cell Physiol* **278**, C235-256 (2000).
183. A. M. Dopico, M. T. Kirber, J. J. Singer, J. V. Walsh, Jr., Membrane stretch directly activates large conductance Ca(2+)-activated K+ channels in mesenteric artery smooth muscle cells. *Am J Hypertens* **7**, 82-89 (1994).
184. K. Z. Shen *et al.*, Tetraethylammonium block of Slowpoke calcium-activated potassium channels expressed in Xenopus oocytes: Evidence for tetrameric channel formation. *Pflügers Archiv* **426**, 440-445 (1994).
185. P. Meera, M. Wallner, M. Song, L. Toro, Large conductance voltage- and calcium-dependent K+ channel, a distinct member of voltage-dependent ion channels with seven N-terminal transmembrane segments (S0-S6), an extracellular N terminus, and an intracellular (S9-S10) C terminus. *Proc Natl Acad Sci U S A* **94**, 14066-14071 (1997).
186. X.-M. Xia, X. Zeng, C. J. Lingle, Multiple regulatory sites in large-conductance calcium-activated potassium channels. *Nature* **418**, 880-884 (2002).
187. R. S. Wu, S. O. Marx, The BK potassium channel in the vascular smooth muscle and kidney: α- and β-subunits. *Kidney International* **78**, 963-974 (2010).
188. A. R. Cox D., Roleofthe1 subunit in large-conductance Ca2-activated K channel gating energetics: mechanisms of enhanced Ca2 sensitivity. *J Gen Physiol* **116**, 411-432 (2000).
189. L. Bao, D. H. Cox, Gating and ionic currents reveal how the BKCa channel's Ca2+ sensitivity is enhanced by its β1 subunit. *The Journal of general physiology* **126**, 393-412 (2005).

190. X. Tao, R. K. Hite, R. MacKinnon, Cryo-EM structure of the open high-conductance Ca2+-activated K+ channel. *Nature* **541**, 46-51 (2017).
191. R. K. Hite, X. Tao, R. MacKinnon, Structural basis for gating the high-conductance Ca2+-activated K+ channel. *Nature* **541**, 52-57 (2017).
192. W. F. Jackson, Potassium Channels in Regulation of Vascular Smooth Muscle Contraction and Growth. *Adv Pharmacol* **78**, 89-144 (2017).
193. O. Jackson-Weaver, D. A. Paredes, L. V. Gonzalez Bosc, B. R. Walker, N. L. Kanagy, Intermittent hypoxia in rats increases myogenic tone through loss of hydrogen sulfide activation of large-conductance Ca(2+)-activated potassium channels. *Circ Res* **108**, 1439-1447 (2011).
194. P. A. Lucchesi, S. Belmadani, K. Matrougui, Hydrogen peroxide acts as both vasodilator and vasoconstrictor in the control of perfused mouse mesenteric resistance arteries. *J Hypertens* **23**, 571-579 (2005).
195. G. J. Pérez, A. D. Bonev, M. T. Nelson, Micromolar Ca(2+) from sparks activates Ca(2+)-sensitive K(+) channels in rat cerebral artery smooth muscle. *Am J Physiol Cell Physiol* **281**, C1769-1775 (2001).
196. C. D. Benham, T. B. Bolton, Spontaneous transient outward currents in single visceral and vascular smooth muscle cells of the rabbit. *J Physiol* **381**, 385-406 (1986).
197. D. P. McCobb *et al.*, A human calcium-activated potassium channel gene expressed in vascular smooth muscle. *American Journal of Physiology-Heart and Circulatory Physiology* **269**, H767-H777 (1995).
198. O. B. McManus *et al.*, Functional role of the β subunit of high conductance calcium-activated potassium channels. *Neuron* **14**, 645-650 (1995).
199. P. Meera, M. Wallner, Z. Jiang, L. Toro, A calcium switch for the functional coupling between α (hslo) and β subunits (KV, Caβ) of maxi K channels. *FEBS Letters* **382**, 84-88 (1996).
200. Y. Tanaka, P. Meera, M. Song, H. G. Knaus, L. Toro, Molecular constituents of maxi KCa channels in human coronary smooth muscle: predominant alpha + beta subunit complexes. *J Physiol* **502 (Pt 3)**, 545-557 (1997).
201. M. D. Leo *et al.*, Dynamic regulation of β1 subunit trafficking controls vascular contractility. *Proc Natl Acad Sci U S A* **111**, 2361-2366 (2014).
202. G. C. Amberg, A. D. Bonev, C. F. Rossow, M. T. Nelson, L. F. Santana, Modulation of the molecular composition of large conductance, Ca(2+) activated K(+) channels in vascular smooth muscle during hypertension. *J Clin Invest* **112**, 717-724 (2003).
203. M. Nieves-Cintrón, G. C. Amberg, C. B. Nichols, J. D. Molkentin, L. F. Santana, Activation of NFATc3 Down-regulates the β1 Subunit of Large Conductance, Calcium-activated K+ Channels in Arterial Smooth Muscle and Contributes to Hypertension*. *Journal of Biological Chemistry* **282**, 3231-3240 (2007).
204. C. W. Taylor, A. A. Genazzani, S. A. Morris, Expression of inositol trisphosphate receptors. *Cell Calcium* **26**, 237-251 (1999).
205. R. Chandrasekhar, K. J. Alzayady, L. E. Wagner, 2nd, D. I. Yule, Unique Regulatory Properties of Heterotetrameric Inositol 1,4,5-Trisphosphate Receptors Revealed by Studying Concatenated Receptor Constructs. *J Biol Chem* **291**, 4846-4860 (2016).
206. D. F. Boehning, in *Current Topics in Membranes,* I. I. Serysheva, Ed. (Academic Press, 2010), vol. 66, pp. 191-207.
207. S. J. Ludtke *et al.*, Flexible architecture of IP3R1 by Cryo-EM. *Structure* **19**, 1192-1199 (2011).
208. D. Narayanan, A. Adebiyi, J. H. Jaggar, Inositol trisphosphate receptors in smooth muscle cells. *Am J Physiol Heart Circ Physiol* **302**, H2190-2210 (2012).

209. J. R. Mauban, J. Zacharia, S. Fairfax, W. G. Wier, PC-PLC/sphingomyelin synthase activity plays a central role in the development of myogenic tone in murine resistance arteries. *Am J Physiol Heart Circ Physiol* **308**, H1517-1524 (2015).
210. H. Abou-Saleh *et al.*, Inositol 1,4,5-trisphosphate (IP3) receptor up-regulation in hypertension is associated with sensitization of Ca2+ release and vascular smooth muscle contractility. *J Biol Chem* **288**, 32941-32951 (2013).
211. D. Mozaffarian *et al.*, Heart Disease and Stroke Statistics-2016 Update: A Report From the American Heart Association. *Circulation* **133**, e38-360 (2016).
212. L. Mosca, E. Barrett-Connor, N. K. Wenger, Sex/gender differences in cardiovascular disease prevention: what a difference a decade makes. *Circulation* **124**, 2145-2154 (2011).
213. S. S. Virani *et al.*, Heart Disease and Stroke Statistics-2020 Update: A Report From the American Heart Association. *Circulation* **141**, e139-e596 (2020).
214. J. C. McSweeney *et al.*, Women's early warning symptoms of acute myocardial infarction. *Circulation* **108**, 2619-2623 (2003).
215. L. S. Mehta *et al.*, Acute Myocardial Infarction in Women: A Scientific Statement From the American Heart Association. *Circulation* **133**, 916-947 (2016).
216. C. Ljungman *et al.*, Gender differences in antihypertensive drug treatment: results from the Swedish Primary Care Cardiovascular Database (SPCCD). *J Am Soc Hypertens* **8**, 882-890 (2014).
217. L. M. Wing *et al.*, A comparison of outcomes with angiotensin-converting--enzyme inhibitors and diuretics for hypertension in the elderly. *N Engl J Med* **348**, 583-592 (2003).
218. E. Lonn *et al.*, Effect of long-term therapy with ramipril in high-risk women. *J Am Coll Cardiol* **40**, 693-702 (2002).
219. I. Os *et al.*, Female preponderance for lisinopril-induced cough in hypertension. *Am J Hypertens* **7**, 1012-1015 (1994).
220. A. Huang, D. Sun, A. Koller, G. Kaley, Gender difference in myogenic tone of rat arterioles is due to estrogen-induced, enhanced release of NO. *Am J Physiol* **272**, H1804-1809 (1997).
221. R. M. Shaw, H. M. Colecraft, L-type calcium channel targeting and local signalling in cardiac myocytes. *Cardiovasc Res* **98**, 177-186 (2013).
222. R. E. White *et al.*, Endothelium-independent effect of estrogen on Ca(2+)-activated K(+) channels in human coronary artery smooth muscle cells. *Cardiovasc Res* **53**, 650-661 (2002).
223. M. Q. Mazzuca, K. M. Mata, W. Li, S. S. Rangan, R. A. Khalil, Estrogen receptor subtypes mediate distinct microvascular dilation and reduction in [Ca2+]I in mesenteric microvessels of female rat. *J Pharmacol Exp Ther* **352**, 291-304 (2015).
224. G. C. Wellman, A. D. Bonev, M. T. Nelson, J. E. Brayden, Gender differences in coronary artery diameter involve estrogen, nitric oxide, and Ca(2+)-dependent K+ channels. *Circ Res* **79**, 1024-1030 (1996).
225. J. Goyette, K. Gaus, Mechanisms of protein nanoscale clustering. *Curr Opin Cell Biol* **44**, 86-92 (2017).
226. A. Honigmann, A. Pralle, Compartmentalization of the Cell Membrane. *J Mol Biol* **428**, 4739-4748 (2016).
227. D. Krapf, Compartmentalization of the plasma membrane. *Curr Opin Cell Biol* **53**, 15-21 (2018).
228. R. D. Taylor, M. Heine, N. J. Emptage, L. C. Andreae, Neuronal Receptors Display Cytoskeleton-Independent Directed Motion on the Plasma Membrane. *iScience* **10**, 234-244 (2018).

229. D. Ghosh *et al.*, Dynamic L-type CaV1.2 channel trafficking facilitates CaV1.2 clustering and cooperative gating. *Biochim Biophys Acta*, (2018).
230. W. I. Newman, D. L. Turcotte, B. D. Malamud, Emergence of patterns in random processes. *Phys Rev E Stat Nonlin Soft Matter Phys* **86**, 026103 (2012).
231. K. G. Beam, J. H. Caldwell, D. T. Campbell, Na channels in skeletal muscle concentrated near the neuromuscular junction. *Nature* **313**, 588-590 (1985).
232. W. A. Catterall, Localization of sodium channels in cultured neural cells. *J Neurosci* **1**, 777-783 (1981).
233. S. G. Waxman, J. M. Ritchie, Organization of ion channels in the myelinated nerve fiber. *Science* **228**, 1502-1507 (1985).
234. B. A. Block, T. Imagawa, K. P. Campbell, C. Franzini-Armstrong, Structural evidence for direct interaction between the molecular components of the transverse tubule/sarcoplasmic reticulum junction in skeletal muscle. *J Cell Biol* **107**, 2587-2600 (1988).
235. R. Duffin *et al.*, The CDK inhibitor, R-roscovitine, promotes eosinophil apoptosis by down-regulation of Mcl-1. *FEBS Lett* **583**, 2540-2546 (2009).
236. D. V. Gathercole *et al.*, Immunogold-labeled L-type calcium channels are clustered in the surface plasma membrane overlying junctional sarcoplasmic reticulum in guinea-pig myocytes-implications for excitation-contraction coupling in cardiac muscle. *J Mol Cell Cardiol* **32**, 1981-1994 (2000).
237. Y. Takagishi, S. Rothery, J. Issberner, A. Levi, N. J. Severs, Spatial distribution of dihydropyridine receptors in the plasma membrane of guinea pig cardiac myocytes investigated by correlative confocal microscopy and label-fracture electron microscopy. *J Electron Microsc (Tokyo)* **46**, 165-170 (1997).
238. A. O. Jorgensen *et al.*, Identification of novel proteins unique to either transverse tubules (TS28) or the sarcolemma (SL50) in rabbit skeletal muscle. *J Cell Biol* **110**, 1173-1185 (1990).
239. O. Vivas, C. M. Moreno, L. F. Santana, B. Hille, Proximal clustering between BK and CaV1.3 channels promotes functional coupling and BK channel activation at low voltage. *Elife* **6**, (2017).
240. R. E. Dixon *et al.*, Graded Ca(2)(+)/calmodulin-dependent coupling of voltage-gated CaV1.2 channels. *eLife* **4**, (2015).
241. C. M. Moreno *et al.*, Ca(2+) entry into neurons is facilitated by cooperative gating of clustered CaV1.3 channels. *Elife* **5**, (2016).
242. S. Tajada *et al.*, Distance constraints on activation of TRPV4 channels by AKAP150-bound PKCalpha in arterial myocytes. *J Gen Physiol* **149**, 639-659 (2017).
243. J. Mercado *et al.*, Local control of TRPV4 channels by AKAP150-targeted PKC in arterial smooth muscle. *J Gen Physiol* **143**, 559-575 (2014).
244. D. Baddeley *et al.*, Optical single-channel resolution imaging of the ryanodine receptor distribution in rat cardiac myocytes. *Proc Natl Acad Sci U S A* **106**, 22275-22280 (2009).
245. E. Kim, K. O. Cho, A. Rothschild, M. Sheng, Heteromultimerization and NMDA receptor-clustering activity of Chapsyn-110, a member of the PSD-95 family of proteins. *Neuron* **17**, 103-113 (1996).
246. E. Kim, M. Niethammer, A. Rothschild, Y. N. Jan, M. Sheng, Clustering of Shaker-type K+ channels by interaction with a family of membrane-associated guanylate kinases. *Nature* **378**, 85-88 (1995).
247. D. H. Cox, Modeling a Ca^{2+} channel/BK_{Ca} channel complex at the single-complex level. *Biophys J* **107**, 2797-2814 (2014).
248. D. Shiomi, M. Yoshimoto, M. Homma, I. Kawagishi, Helical distribution of the bacterial chemoreceptor via colocalization with the Sec protein translocation machinery. *Mol Microbiol* **60**, 894-906 (2006).

249. S. Thiem, D. Kentner, V. Sourjik, Positioning of chemosensory clusters in E. coli and its relation to cell division. *Embo j* **26**, 1615-1623 (2007).
250. H. Wang, N. S. Wingreen, R. Mukhopadhyay, Self-organized periodicity of protein clusters in growing bacteria. *Phys Rev Lett* **101**, 218101 (2008).
251. G. T. Dempsey, J. C. Vaughan, K. H. Chen, M. Bates, X. Zhuang, Evaluation of fluorophores for optimal performance in localization-based super-resolution imaging. *Nature methods* **8**, 1027-1036 (2011).
252. J. Folling *et al.*, Fluorescence nanoscopy by ground-state depletion and single-molecule return. *Nature methods* **5**, 943-945 (2008).
253. D. Greenfield *et al.*, Self-organization of the Escherichia coli chemotaxis network imaged with super-resolution light microscopy. *PLoS Biol* **7**, e1000137 (2009).
254. W. Stuhmer, W. Almers, Photobleaching through glass micropipettes: sodium channels without lateral mobility in the sarcolemma of frog skeletal muscle. *Proc Natl Acad Sci U S A* **79**, 946-950 (1982).
255. E. M. Green, C. F. Barrett, G. Bultynck, S. M. Shamah, R. E. Dolmetsch, The tumor suppressor eIF3e mediates calcium-dependent internalization of the L-type calcium channel Ca(v)1.2. *Neuron* **55**, 615-632 (2007).
256. H. Shigematsu, T. Sokabe, R. Danev, M. Tominaga, K. Nagayama, A 3.5-nm structure of rat TRPV4 cation channel revealed by Zernike phase-contrast cryoelectron microscopy. *J Biol Chem* **285**, 11210-11218 (2010).
257. Z. Deng *et al.*, Cryo-EM and X-ray structures of TRPV4 reveal insight into ion permeation and gating mechanisms. *Nat Struct Mol Biol* **25**, 252-260 (2018).
258. V. Di Biase *et al.*, Surface traffic of dendritic CaV1.2 calcium channels in hippocampal neurons. *J Neurosci* **31**, 13682-13694 (2011).
259. R. Conrad *et al.*, Rapid Turnover of the Cardiac L-Type CaV1.2 Channel by Endocytic Recycling Regulates Its Cell Surface Availability. *iScience* **7**, 1-15 (2018).
260. B. Schwanhausser *et al.*, Global quantification of mammalian gene expression control. *Nature* **473**, 337-342 (2011).
261. G. C. Amberg, C. F. Rossow, M. F. Navedo, L. F. Santana, NFATc3 regulates Kv2.1 expression in arterial smooth muscle. *J Biol Chem* **279**, 47326-47334 (2004).
262. C. F. Rossow, K. W. Dilly, L. F. Santana, Differential Calcineurin/NFATc3 Activity Contributes to the I_{to} Transmural Gradient in the Mouse Heart. *Circ Res* **98**, 1306-1313 (2006).
263. C. F. Rossow, E. Minami, E. G. Chase, C. E. Murry, L. F. Santana, NFATc3-Induced Reductions in Voltage-Gated K^+ Currents After Myocardial Infarction. *Circ Res* **94**, 1340-1350 (2004).
264. C. F. Rossow *et al.*, NFATc3-dependent loss of I_{to} gradient across the left ventricular wall during chronic beta adrenergic stimulation. *J Mol Cell Cardiol* **46**, 249-256 (2009).
265. M. Nieves-Cintrón, G. C. Amberg, M. F. Navedo, J. D. Molkentin, L. F. Santana, The control of Ca^{2+} influx and NFATc3 signaling in arterial smooth muscle during hypertension. *Proc Natl Acad Sci U S A* **105**, 15623-15628 (2008).
266. M. Nieves-Cintrón, G. C. Amberg, C. B. Nichols, J. D. Molkentin, L. F. Santana, Activation of NFATc3 down-regulates the β1 subunit of large conductance, calcium-activated K^+ channels in arterial smooth muscle and contributes to hypertension. *J Biol Chem* **282**, 3231-3240 (2007).
267. J. Adam, N. Basnet, N. Mizuno, Structural insights into the cooperative remodeling of membranes by amphiphysin/BIN1. *Sci Rep* **5**, 15452 (2015).
268. E. Lee *et al.*, Amphiphysin 2 (Bin1) and T-tubule biogenesis in muscle. *Science* **297**, 1193-1196 (2002).
269. T. Hong *et al.*, Cardiac BIN1 folds T-tubule membrane, controlling ion flux and limiting arrhythmia. *Nat Med* **20**, 624-632 (2014).

270. T. T. Hong *et al.*, BIN1 localizes the L-type calcium channel to cardiac T-tubules. *PLoS Biol* **8**, e1000312 (2010).
271. A. De La Mata *et al.*, BIN1 Induces the Formation of T-Tubules and Adult-Like Ca^{2+} Release Units in Developing Cardiomyocytes. *Stem Cells*, (2018).
272. T. Wegierski, K. Hill, M. Schaefer, G. Walz, The HECT ubiquitin ligase AIP4 regulates the cell surface expression of select TRP channels. *Embo j* **25**, 5659-5669 (2006).
273. B. Rosati *et al.*, Robust L-type calcium current expression following heterozygous knockout of the Cav1.2 gene in adult mouse heart. *J Physiol* **589**, 3275-3288 (2011).
274. B. Hille, *Ionic Channels of Excitable Membranes*. (Sinauer Associates Inc., Suderland, Massachusetts, ed. 3rd Edition, 2001), pp. 814.
275. C. D. Garciarena, Y. L. Ma, P. Swietach, L. Huc, R. D. Vaughan-Jones, Sarcolemmal localisation of Na+/H+ exchange and Na+-HCO3- co-transport influences the spatial regulation of intracellular pH in rat ventricular myocytes. *J Physiol* **591**, 2287-2306 (2013).
276. G. K. Yuen, S. Galice, D. M. Bers, Subcellular localization of Na/K-ATPase isoforms in ventricular myocytes. *J Mol Cell Cardiol* **108**, 158-169 (2017).
277. J. R. Sanes, J. W. Lichtman, Induction, assembly, maturation and maintenance of a postsynaptic apparatus. *Nat Rev Neurosci* **2**, 791-805 (2001).
278. A. D. Nelson, P. M. Jenkins, Axonal Membranes and Their Domains: Assembly and Function of the Axon Initial Segment and Node of Ranvier. *Front Cell Neurosci* **11**, 136 (2017).
279. M. Kirmiz, N. C. Vierra, S. Palacio, J. S. Trimmer, Identification of VAPA and VAPB as Kv2 Channel-Interacting Proteins Defining Endoplasmic Reticulum-Plasma Membrane Junctions in Mammalian Brain Neurons. *J Neurosci* **38**, 7562-7584 (2018).
280. B. Johnson *et al.*, Kv2 potassium channels form endoplasmic reticulum/plasma membrane junctions via interaction with VAPA and VAPB. *Proc Natl Acad Sci U S A* **115**, E7331-E7340 (2018).
281. H. J. Knot, M. T. Nelson, Regulation of arterial diameter and wall [Ca2+] in cerebral arteries of rat by membrane potential and intravascular pressure. *J Physiol* **508 (Pt 1)**, 199-209 (1998).
282. W. M. Bayliss, On the local reactions of the arterial wall to changes of internal pressure. *J Physiol* **28**, 220-231 (1902).
283. A. L. Gonzales *et al.*, A PLCgamma1-dependent, force-sensitive signaling network in the myogenic constriction of cerebral arteries. *Sci Signal* **7**, ra49 (2014).
284. S. Q. Wang, L. S. Song, E. G. Lakatta, H. Cheng, Ca2+ signalling between single L-type Ca2+ channels and ryanodine receptors in heart cells. *Nature* **410**, 592-596 (2001).
285. D. Sato *et al.*, A stochastic model of ion channel cluster formation in the plasma membrane. *J Gen Physiol* **151**, 1116-1134 (2019).
286. M. T. Nelson *et al.*, Relaxation of arterial smooth muscle by calcium sparks. *Science* **270**, 633-637 (1995).
287. S. C. O'Dwyer *et al.*, Kv2.1 channels play opposing roles in regulating membrane potential, Ca(2+) channel function, and myogenic tone in arterial smooth muscle. *Proc Natl Acad Sci U S A* **117**, 3858-3866 (2020).
288. N. C. Vierra, M. Kirmiz, D. van der List, L. F. Santana, J. S. Trimmer, Kv2.1 mediates spatial and functional coupling of L-type calcium channels and ryanodine receptors in mammalian neurons. *Elife* **8**, (2019).
289. N. C. Vierra, S. C. O'Dwyer, C. Matsumoto, L. F. Santana, J. S. Trimmer, Regulation of neuronal excitation-transcription coupling by Kv2.1-induced clustering of somatic L-type Ca(2+) channels at ER-PM junctions. *Proc Natl Acad Sci U S A* **118**, (2021).
290. E. E. Maverick, M. M. Tamkun, High spatial density is associated with non-conducting Kv channels from two families. *Biophys J* **121**, 755-768 (2022).

291. J. Du, J. H. Tao-Cheng, P. Zerfas, C. J. McBain, The K+ channel, Kv2.1, is apposed to astrocytic processes and is associated with inhibitory postsynaptic membranes in hippocampal and cortical principal neurons and inhibitory interneurons. *Neuroscience* **84**, 37-48 (1998).
292. J. S. Trimmer, Immunological identification and characterization of a delayed rectifier K+ channel polypeptide in rat brain. *Proc Natl Acad Sci U S A* **88**, 10764-10768 (1991).
293. K. S. Park, D. P. Mohapatra, H. Misonou, J. S. Trimmer, Graded regulation of the Kv2.1 potassium channel by variable phosphorylation. *Science* **313**, 976-979 (2006).
294. H. Misonou *et al.*, Regulation of ion channel localization and phosphorylation by neuronal activity. *Nat Neurosci* **7**, 711-718 (2004).
295. H. Misonou *et al.*, Bidirectional activity-dependent regulation of neuronal ion channel phosphorylation. *J Neurosci* **26**, 13505-13514 (2006).
296. D. S. Bindels *et al.*, mScarlet: a bright monomeric red fluorescent protein for cellular imaging. *Nat Methods* **14**, 53-56 (2017).
297. M. M. Cobb, D. C. Austin, J. T. Sack, J. S. Trimmer, Cell cycle-dependent changes in localization and phosphorylation of the plasma membrane Kv2.1 K+ channel impact endoplasmic reticulum membrane contact sites in COS-1 cells. *J Biol Chem* **291**, 5527 (2016).
298. J. B. Olmsted, Affinity purification of antibodies from diazotized paper blots of heterogeneous protein samples. *J Biol Chem* **256**, 11955-11957 (1981).
299. G. H. Hernandez *et al.*, A Computational Model Predicts Sex-specific Responses to Calcium Channel Blockers in Mesenteric Vascular Smooth Muscle. *bioRxiv*, 2023.2006.2024.546394 (2023).
300. L. Guarina *et al.*, Biological noise is a key determinant of the reproducibility and adaptability of cardiac pacemaking and EC coupling. *J Gen Physiol* **154**, (2022).
301. M. J. Marquis, J. T. Sack, Mechanism of use-dependent Kv2 channel inhibition by RY785. *J Gen Physiol* **154**, (2022).
302. J. Herrington *et al.*, Identification of novel and selective Kv2 channel inhibitors. *Mol Pharmacol* **80**, 959-964 (2011).
303. D. C. Tilley *et al.*, The tarantula toxin GxTx detains K(+) channel gating charges in their resting conformation. *J Gen Physiol* **151**, 292-315 (2019).
304. S. Fredriksson *et al.*, Protein detection using proximity-dependent DNA ligation assays. *Nat Biotechnol* **20**, 473-477 (2002).
305. B. Koos *et al.*, Analysis of protein interactions in situ by proximity ligation assays. *Curr Top Microbiol Immunol* **377**, 111-126 (2014).
306. M. Kirmiz *et al.*, Remodeling neuronal ER-PM junctions is a conserved nonconducting function of Kv2 plasma membrane ion channels. *Mol Biol Cell* **29**, 2410-2432 (2018).
307. M. F. Navedo *et al.*, Ca(v)1.3 channels produce persistent calcium sparklets, but Ca(v)1.2 channels are responsible for sparklets in mouse arterial smooth muscle. *Am J Physiol Heart Circ Physiol* **293**, H1359-1370 (2007).
308. D. E. Antonucci, S. T. Lim, S. Vassanelli, J. S. Trimmer, Dynamic localization and clustering of dendritic Kv2.1 voltage-dependent potassium channels in developing hippocampal neurons. *Neuroscience* **108**, 69-81 (2001).
309. O. Cerda, J. S. Trimmer, Activity-dependent phosphorylation of neuronal Kv2.1 potassium channels by CDK5. *J Biol Chem* **286**, 28738-28748 (2011).
310. B. Johnson *et al.*, Kv2 potassium channels form endoplasmic reticulum/plasma membrane junctions via interaction with VAPA and VAPB. *Proc Natl Acad Sci U S A* **115**, E7331-e7340 (2018).
311. T. Di Mattia *et al.*, FFAT motif phosphorylation controls formation and lipid transfer function of inter-organelle contacts. *EMBO J* **39**, e104369 (2020).

312. G. Stuart, B. Sakmann, Amplification of EPSPs by axosomatic sodium channels in neocortical pyramidal neurons. *Neuron* **15**, 1065-1076 (1995).
313. N. P. Issa, A. J. Hudspeth, Clustering of Ca2+ channels and Ca(2+)-activated K+ channels at fluorescently labeled presynaptic active zones of hair cells. *Proc Natl Acad Sci U S A* **91**, 7578-7582 (1994).
314. H. Takekura, X. Sun, C. Franzini-Armstrong, Development of the excitation-contraction coupling apparatus in skeletal muscle: peripheral and internal calcium release units are formed sequentially. *J Muscle Res Cell Motil* **15**, 102-118 (1994).
315. R. E. Dixon, J. S. Trimmer, Endoplasmic Reticulum-Plasma Membrane Junctions as Sites of Depolarization-Induced Ca(2+) Signaling in Excitable Cells. *Annu Rev Physiol* **85**, 217-243 (2023).
316. V. A. Nirenberg, O. Yifrach, Bridging the Molecular-Cellular Gap in Understanding Ion Channel Clustering. *Front Pharmacol* **10**, 1644 (2019).
317. R. E. Dixon, M. F. Navedo, M. D. Binder, L. F. Santana, Mechanisms and physiological implications of cooperative gating of clustered ion channels. *Physiol Rev* **102**, 1159-1210 (2022).
318. T.-T. Hong *et al.*, BIN1 is reduced and Cav1. 2 trafficking is impaired in human failing cardiomyocytes. *Heart rhythm* **9**, 812-820 (2012).
319. T.-T. Hong *et al.*, BIN1 Localizes the L-Type Calcium Channel to Cardiac T-Tubules. *PLOS Biology* **8**, e1000312 (2010).
320. E. M. Green, C. F. Barrett, G. Bultynck, S. M. Shamah, R. E. Dolmetsch, The Tumor Suppressor eIF3e Mediates Calcium-Dependent Internalization of the L-Type Calcium Channel CaV1.2. *Neuron* **55**, 615-632 (2007).
321. R. Conrad *et al.*, Rapid Turnover of the Cardiac L-Type Ca(V)1.2 Channel by Endocytic Recycling Regulates Its Cell Surface Availability. *iScience* **7**, 1-15 (2018).
322. D. Ghosh *et al.*, Dynamic L-type CaV1.2 channel trafficking facilitates CaV1.2 clustering and cooperative gating. *Biochimica et Biophysica Acta (BBA) - Molecular Cell Research* **1865**, 1341-1355 (2018).
323. D. W. Ito *et al.*, β-adrenergic-mediated dynamic augmentation of sarcolemmal Ca(V) 1.2 clustering and co-operativity in ventricular myocytes. *J Physiol* **597**, 2139-2162 (2019).
324. S. G. Del Villar *et al.*, β-Adrenergic control of sarcolemmal CaV1. 2 abundance by small GTPase Rab proteins. *Proceedings of the National Academy of Sciences* **118**, e2017937118 (2021).
325. P. F. Pratt, S. Bonnet, L. M. Ludwig, P. Bonnet, N. J. Rusch, Upregulation of L-type Ca2+ channels in mesenteric and skeletal arteries of SHR. *Hypertension* **40**, 214-219 (2002).
326. R. H. Cox, I. M. Lozinskaya, Augmented calcium currents in mesenteric artery branches of the spontaneously hypertensive rat. *Hypertension* **26**, 1060-1064 (1995).
327. Y. Ohya, T. Tsuchihashi, S. Kagiyama, I. Abe, M. Fujishima, Single L-type calcium channels in smooth muscle cells from resistance arteries of spontaneously hypertensive rats. *Hypertension* **31**, 1125-1129 (1998).
328. J. M. Simard, X. Li, K. Tewari, Increase in functional Ca2+ channels in cerebral smooth muscle with renal hypertension. *Circ Res* **82**, 1330-1337 (1998).
329. D. W. Wilde, P. B. Furspan, J. F. Szocik, Calcium current in smooth muscle cells from normotensive and genetically hypertensive rats. *Hypertension* **24**, 739-746 (1994).
330. D. W. Wilde, K. D. Massey, G. K. Walker, A. Vollmer, R. J. Grekin, High-fat diet elevates blood pressure and cerebrovascular muscle Ca(2+) current. *Hypertension* **35**, 832-837 (2000).
331. S. Tajada *et al.*, Down-regulation of CaV1.2 channels during hypertension: how fewer CaV1.2 channels allow more Ca(2+) into hypertensive arterial smooth muscle. *J Physiol* **591**, 6175-6191 (2013).

332. J. P. Bannister *et al.*, Transcriptional upregulation of α2δ-1 elevates arterial smooth muscle cell voltage-dependent Ca2+ channel surface expression and cerebrovascular constriction in genetic hypertension. *Hypertension* **60**, 1006-1015 (2012).
333. S. V. Kharade *et al.*, The β3 Subunit Contributes to Vascular Calcium Channel Upregulation and Hypertension in Angiotensin II–Infused C57BL/6 Mice. *Hypertension* **61**, 137-142 (2013).
334. M. Murakami *et al.*, Modified cardiovascular L-type channels in mice lacking the voltage-dependent Ca2+ channel beta3 subunit. *J Biol Chem* **278**, 43261-43267 (2003).
335. E. Kobrinsky *et al.*, Effect of Cavβ Subunits on Structural Organization of Cav1.2 Calcium Channels. *PLOS ONE* **4**, e5587 (2009).
336. S. Tajada *et al.*, Distance constraints on activation of TRPV4 channels by AKAP150-bound PKCα in arterial myocytes. *Journal of General Physiology* **149**, 639-659 (2017).
337. H. I. Bishop *et al.*, Kv2 Ion Channels Determine the Expression and Localization of the Associated AMIGO-1 Cell Adhesion Molecule in Adult Brain Neurons. *Front Mol Neurosci* **11**, 1 (2018).
338. P. D. Fox *et al.*, Induction of stable ER-plasma-membrane junctions by Kv2.1 potassium channels. *J Cell Sci* **128**, 2096-2105 (2015).
339. B. Johnson *et al.*, Kv2 potassium channels form endoplasmic reticulum/plasma membrane junctions via interaction with VAPA and VAPB. *Proceedings of the National Academy of Sciences* **115**, E7331-E7340 (2018).
340. A. Gallo, C. Vannier, T. Galli, Endoplasmic Reticulum-Plasma Membrane Associations:Structures and Functions. *Annu Rev Cell Dev Biol* **32**, 279-301 (2016).
341. E. D. Moore *et al.*, Organization of Ca2+ release units in excitable smooth muscle of the guinea-pig urinary bladder. *Biophys J* **87**, 1836-1847 (2004).
342. A. P. Somlyo, Excitation-contraction coupling and the ultrastructure of smooth muscle. *Circ Res* **57**, 497-507 (1985).